# A DETAILED STUDY OF THE GAMMA-RAY NOVA V1324 SCO

By

Thomas Michael Broen Finzell

A DISSERTATION

Submitted to
Michigan State University
in partial fulfillment of the requirements
for the degree of

Astrophysics and Astronomy- Doctor of Philosophy

2017

ABSTRACT

A DETAILED STUDY OF THE GAMMA-RAY NOVA V1324 SCO

By

Thomas Michael Broen Finzell

It has recently been discovered that some, if not all, classical novae emit GeV gamma-rays, but the mechanisms involved in the production of the gamma-rays are still not well understood. We present here a comprehensive, multi-wavelength dataset—from radio to X-rays—for the most gamma-ray luminous classical nova to-date, V1324 Sco. Using this dataset, we show that V1324 Sco is a canonical dusty Fe-II type nova, with a reddening of $E(B-V) = 1.16 \pm 0.12$, a distance limit of $r_D > 6.5$ kpc, a bulk ejecta velocity of $1150 \pm 40$ km s$^{-1}$and an ejecta mass of $2.0 \pm 0.4 \times 10^{-5}$ $M_{\odot}$. However, despite its seeming normalcy, there is also evidence for complex shock interactions, including the aforementioned gamma-rays and early time high-brightness temperature radio emission. To explain how a nova can be simultaneously ordinary and have the highest gamma-ray luminosity to date, we present a simplified model of the ejecta in which the strength of gamma-ray emission is set by properties of a fast ejecta component that collides with a slower component to produce shocks. We conclude this detailed study of V1324 Sco by showing how it has helped shape our understanding of the role of shocks in novae.

Along with the study of V1324 Sco, this work also presents detailed methods for determining the reddening, distance, and filling factor of a classical nova from optical spectroscopy (using V1324 Sco as an example). We also provide detailed derivations for fitting nova radio light curves, to determine ejecta mass and velocity.

# ACKNOWLEDGMENTS

I would like to thank my adviser, Laura Chomiuk, who supported me for the last four years and shepherded me towards becoming a scientist. You were patient, kind, and thoughtful with me throughout the whole process. I learned a enormous amount from you. Thank you.

I would also like to thank the other four members of my thesis committee: Ed Brown, Danny Caballero, Megan Donahue, and Chris Wrede. In particular I'd like to thank Megan Donahue, for always pushing me to be better and treating me like an astronomer (rather than a student) from day one, and Danny Caballero, for giving me invaluable advice and guidance during my transition to Physics Education Research.

I would also like to thank Brian O'Shea for helping me negotiate grad school from my very first day. You are a large part of the reason why I was able to survive grad school, especially the two years before Laura arrived.

Thanks to my collaborators in the eNova research group, who gave me invaluable help with my research: Justin Linford, Tommy Nelson, Koji Mukai, Jennifer Weston, Jennifer Sokoloski, Michael Rupen, and Amy Mioduszewski. A special thanks to Brian Metzger: working with you was the first time I felt like an independent researcher.

Thanks also to Vashti Davis Sawtelle, Paul Irving, and the rest of the PERL group for making me feel so welcome every week and helping me in my transition to Physics Education Research.

Thanks to my friends at Michigan State (in no particular order): Bethany, Alanna, Justin, Mike, Chris, Dennis, Matt, Rachel, Jess, Terri, Bill, Drew, Ashley, Corey, Kelsey, Laura, Alex, Greg, Danny, Rachel, Dana, Kristen, Jessica, Kim, and so many others. You made grad school bearable and my time in Michigan enjoyable. Especially Kim.

Thanks to my friends back home who helped keep me sane every Sunday: Cullen, Phil, Eric, Eric, and Aaron. And thanks to my best friend Megan.

Finally, I would not be here if it weren't for my parents, who provided me with every opportunity to succeed in life.

# TABLE OF CONTENTS

# LIST OF TABLES

# LIST OF FIGURES

# 1 Introduction

## 1.1 Observations and Characteristics of Classical Novae

Historically, the name *nova* stems from the Latin for "new" (Duerbeck, 2008) signifying that these were new objects in the sky that appeared to come from out of nothingness into being. Nova events are characterized by a $10^4 - 10^6$ increase in luminosity and eject between $\sim 10^{-3} - 10^{-7} M_\odot$ of material at velocities $\gtrsim 10^3$ km s$^{-1}$ (Gallagher & Starrfield, 1978; Prialnik, 1986; Yaron et al., 2005; Shore, 2012; Starrfield et al., 2016). The study of classical novae as we know it today began at the very end of the 19th century, with the regular sky patrols of the Harvard College Observatory (Bode & Evans, 2008). We now know that classical novae are the result of a thermonuclear runaway taking place on the surface of a white dwarf and are fueled by matter accreted onto the white dwarf from a companion star (Gallagher & Starrfield, 1978). But it wasn't until the late 1960s and early 1970s that this picture was generally accepted ((Kraft, 1964; Paczyński, 1965). Figure 1.1 shows the binary nature of GK Per, one of the old nova systems studied by Kraft (1964).

To gain a complete picture of classical novae, we need to incorporate observations in *all* wavelength regimes, to form a single cohesive story. In this section we describe the four major wavelength regimes, and how each one of them is a different puzzle piece that we must fit together to understand novae.

Before we begin, we must first give an operational definition for what exactly a classical nova is. The definition we use comes from Gallagher & Starrfield (1978), and is based on the optical properties (i.e. in the visible wavelength regime) of classical novae. The definition focuses on the optical properties because that is the regime with the largest amount of data available.

Gallagher & Starrfield (1978) defines a classical nova as having :

1. **The optical brightness increases by a factor greater than $10^4$ in less than ∼few days**
2. **The increase in brightness begins to subside on timescales of $10^3$ days (or less)**
3. **The spectral development can be classified in using the standard nova classification scheme (discussed in Section 1.1.1.2).**
4. **Spectroscopically derived velocities are greater than greater than 100 km s$^{-1}$and less than 5000 km s$^{-1}$.**
5. **No outburst has been previously observed from this star.**

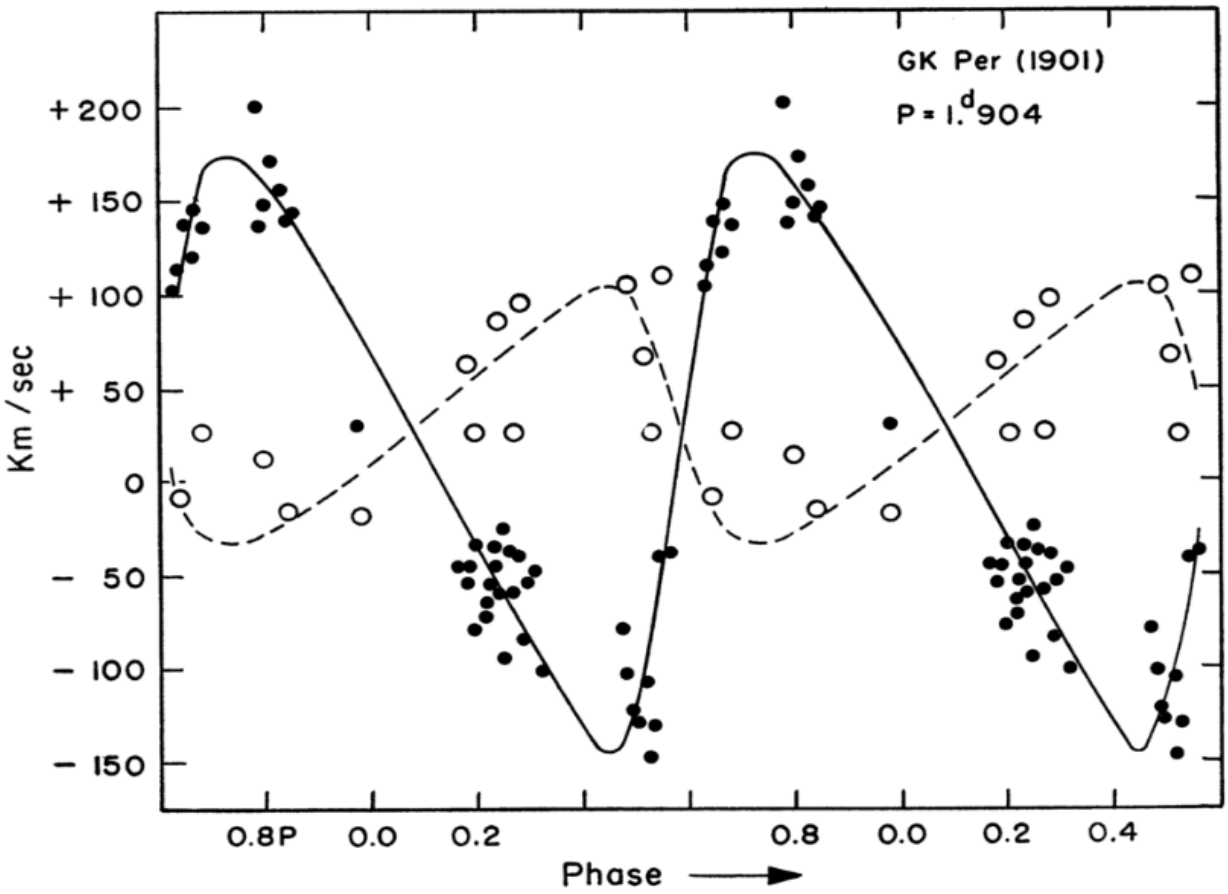


Figure 1.1 Plot showing the radial velocity measurements of the old nova GK Per, made by Kraft (1964). This was the first evidence that most—if not all—of the systems that had undergone a nova outburst were binary systems. Taken from (Kraft, 1964)

Note that the last point excludes recurrent novae (novae that have been observed to go into outburst two or more times). Although it is generally assumed that all novae erupt multiple times (Schaefer, 2010), there is still debate over whether novae with recurrence times $< 100$ years (i.e. novae that could potentially have been labeled recurrent) are indeed unique from classical novae (Pagnotta & Schaefer, 2014).

We devote the rest of this section to describing the different wavelength regimes, and what they each contribute to the picture of classical novae. In Section 1.1.1, we describe ultraviolet, visible, and optical observations; in Section 1.1.2, we detail radio observations of classical novae; in Section 1.1.3, we describe the role played by X-rays in studying classical novae; finally, in Section 1.1.4, we describe (GeV) gamma-ray observations of classical novae.

Later in the chapter we will discuss the nova theory, discussing the details of the energy generation and thermonuclear runaway in Section 1.2.1, the details of how the nova ejects mass in Section 1.2.2, and rounding out the theory with a discussion of the physical differences in nova systems and how they can effect

the observational features in Section 1.2.3.

We conclude this chapter by giving a brief description of V1324 Sco, the primary subject of this work, and laying out the organization of this thesis.

### 1.1.1 UVOIR Observations

The UV/Optical/IR (hereafter referred to as UVOIR) emission from classical novae has the most historical pedigree, dating back to the late 19th century (Bode & Evans, 2008). The large quantity of UVOIR data, however, has mainly served to accentuate the large degree of variation that exists within novae.

Late-time UVOIR observations can also yield resolved imaging of the nova, giving information about the geometry and structure of the ejecta (see, e.g., Slavin et al. 1995; Gill & O'Brien 1998). This will be especially useful in the future, as we try to disentangle the qualitative effects that different geometries and orientation angles can have on the shape of the light curve and spectral lines.

#### 1.1.1.1 UVOIR Photometry

Historical photometric records can stretch as far back as 1890 (Duerbeck, 2008). Qualitative analysis of these photometric measurements has been undertaken several times (Payne-Gaposchkin, 1964; Strope et al., 2010). With the numerous large scale surveys—e.g. OGLE (Udalski, 2003), MOA (Bond et al., 2001), ASSA-SN[1], etc—we are able to probe the temporal evolution of novae to an unprecedented resolution.

The evolution of the light curve is, at early times, dominated by optically thick emission from an expanding (pseudo) photosphere (Shore, 2008). This initial phase is referred to as the *Fireball stage*. In this stage the photosphere is expanding, and the edge of the photosphere is at or very near to the edge of the ejecta. During this expansion phase, the nova is becoming brighter at all wavelengths, due to the increasing size of the emitting region. As the photosphere expands the ejecta become more diffuse, decreasing the opacity. Eventually the decrease in opacity will be greater than the expansion of the ejecta/increase in the size of the emitting region; when this happens the photosphere will begin to shrink, and the brightness will begin to decrease (Bath, 1978). At this time, emission lines begin to dominate the total optical emission. A template of a nova light curve that captures most of the qualitative features can be seen in Figure 1.2.

Note that this same type of evolution occurs at all wavelengths that are dominated by thermal emission. The shorter the frequency of emission, the earlier it will become optically thin. This type of self-similar behavior comes from the fact that the physical process generating the light we see—free-free or bremsstrahlung radiation—is the same emission mechanism across all the wavelength regimes that are redward of the Wien

[1] `http://www.astronomy.ohio-state.edu/~assassin/index.shtml`

tail (i.e. not in the exponential cutoff of the blackbody function). We will discuss this further in Section 1.1.2, which details the evolution of radio emission.

Figure 1.2 also shows some qualitative deviations commonly seen in nova light curves, such as a dust dip and oscillations (seen in the "Transition Phase"). There is good evidence that the physical mechanism causing the dotted-line dip in this schematic light curve is the formation of dust within the ejecta (see, e.g., Gehrz et al. 1980; Gehrz 1988; Derdzinski et al. 2016). However, the physical mechanism governing the oscillatory behavior still remains unknown. It is becoming increasingly clear that novae are not spherically symmetric (Hutchings, 1972; Solf, 1983; Ribeiro et al., 2011; Chomiuk et al., 2014); as a result, it has been postulated that at least part of the variance in the light curve evolution is due to the effects of differing inclination angles (Fred Walter, Private Communication). More detail about the physical conditions that could cause differences in novae can be found in Section 1.2.3.

Given the number of historical observations made of classical novae, it is no surprise that the first means of classifying novae was based on the evolution of the optical light curve. The first classification scheme came from Payne-Gaposchkin (1964), who utilized the speed at with which the nova declined from its maximum magnitude as her primary metric. This is usually given by the values $t_2$ or $t_3$, which denote the number of days it takes for the nova to decrease by 2 and 3 magnitudes from peak, respectively. A more qualitative classification scheme was put forward by Strope et al. (2010), which utilized the overall structure of the light curve for their classification scheme.

#### 1.1.1.2 UVOIR Spectroscopy

Broadly speaking, all nova spectra can be broken into two different phases: Photospheric (or optically thick) and nebular (McLaughlin, 1956). The difference between these two phases is that, during the Photospheric phase, the strongest optical emission lines are permitted, whereas in the nebular phase the strongest (non-Balmer) lines are forbidden transitions, and they also dominate the total optical emission (McLaughlin, 1956). The lines in the nebular phase have a much higher ionization state, due to the lack of absorbing material blocking harder radiation from escaping the surface of the white dwarf.

In virtually all novae the most prominent spectral feature in the optical during the optically thick phase are the hydrogen Balmer lines (Williams et al., 1991). The primary spectral classification scheme— originally put forward by Williams et al. (1991) and later refined in Williams et al. (1994)—classifies novae based on the *second* most prominent feature. Using this classification scheme, virtually all novae fall into one of two categories: novae with prominent iron lines—called Fe-II types—and novae with helium, nitrogen, and other (relatively) high ionization lines—called He/N types. See Figure 1.3 for examples of these two novae.

Qualitative features of these two types of novae are discussed in Williams (1992) and Williams (2012):

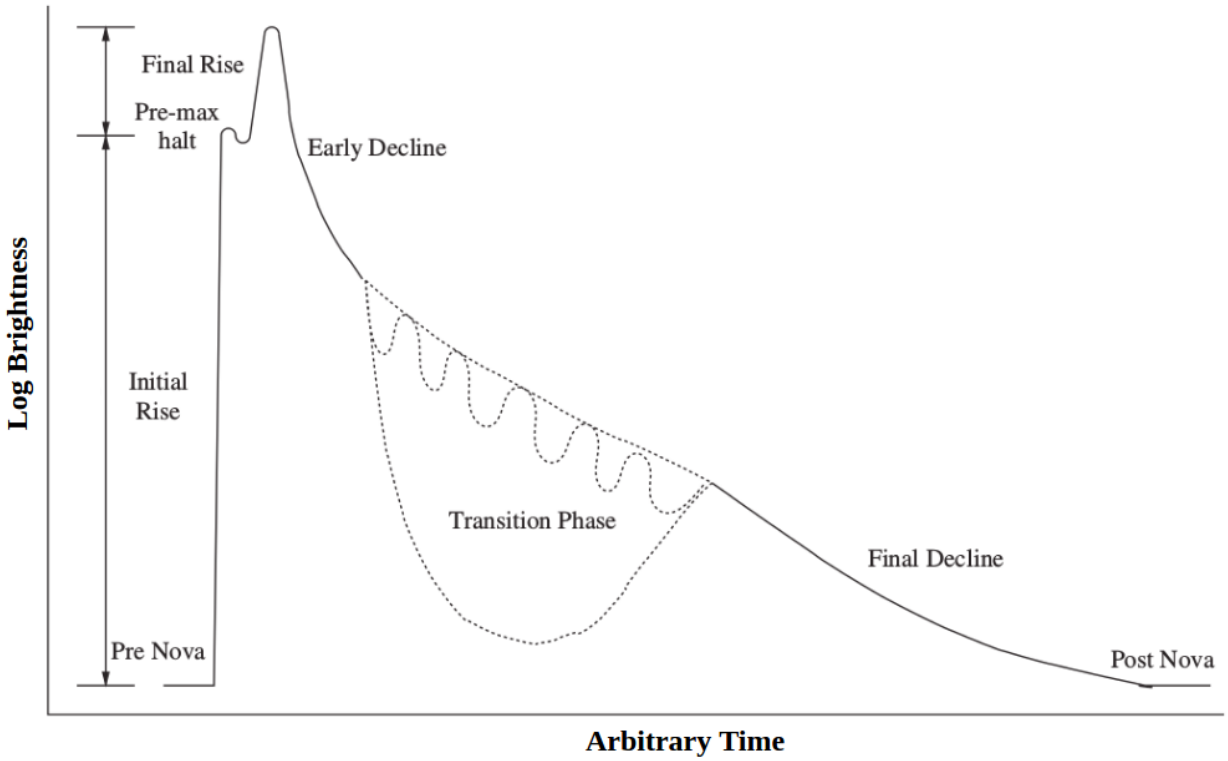


Figure 1.2 A breakdown of the qualitatively different phases of the light curve evolution of a classical nova. This shows the overarching features of a classical nova, including the extremely rapid rise, the slow decline, and the (potential) dust dip and oscillatory behavior that can occur during the decline. With the exception of the dip/oscillations, we expect this same type of evolution for all wavelengths dominated by thermal emission. Adapted from (Warner, 1989)

the He/N spectral type usually have rectangular line profiles and high expansion velocities, while the Fe-II type novae usually have lower expansion speeds, they exhibit P-Cygni profiles (absorption at the blue end of a spectral feature), and the specific lines look similar to ones seen in the envelope of a late-type star. There are also novae that are a hybrid of these two types, initially showing an Fe-II type spectral signature and—at later times—showing an He/N type spectral signature.

The UVOIR has a great deal of information embedded within it, but the analysis can be quite complex. The UVOIR spectroscopy emission is shaped by the abundances and ionization states of hundreds of ion species. If properly leveraged, the UVOIR spectral observations can be used to determine the intensive properties (e.g. temperature, abundances, density, etc) of the ejecta (see, e.g., Schwarz et al. 1997).

To unravel the emission into physically meaningful quantities requires a very detailed radiative transfer calculation, usually outside of the density regime where typical line fitting codes (e.g., CLOUDY Ferland et al. 1998) are valid, at least during the early time evolution. At later times—i.e. during the nebular stage of the novae evolution—it may be possible to fit abundances, temperatures, and density. Efforts to do just

this have shown mixed levels of success (Schwarz et al., 1997, 2007)

Finally, there is also information about the geometry (i.e. the three dimensional shape of the ejected material) encoded in the line structure. Previous efforts to leverage this information can be found in (Hutchings, 1972; Gill & O'Brien, 1999; Ribeiro et al., 2013). In the future, with interferometric measurements—both in the radio and near-IR—we will have the means to check the analysis of spectroscopic line structures against the true geometry (see, e.g., Ribeiro et al. 2009).

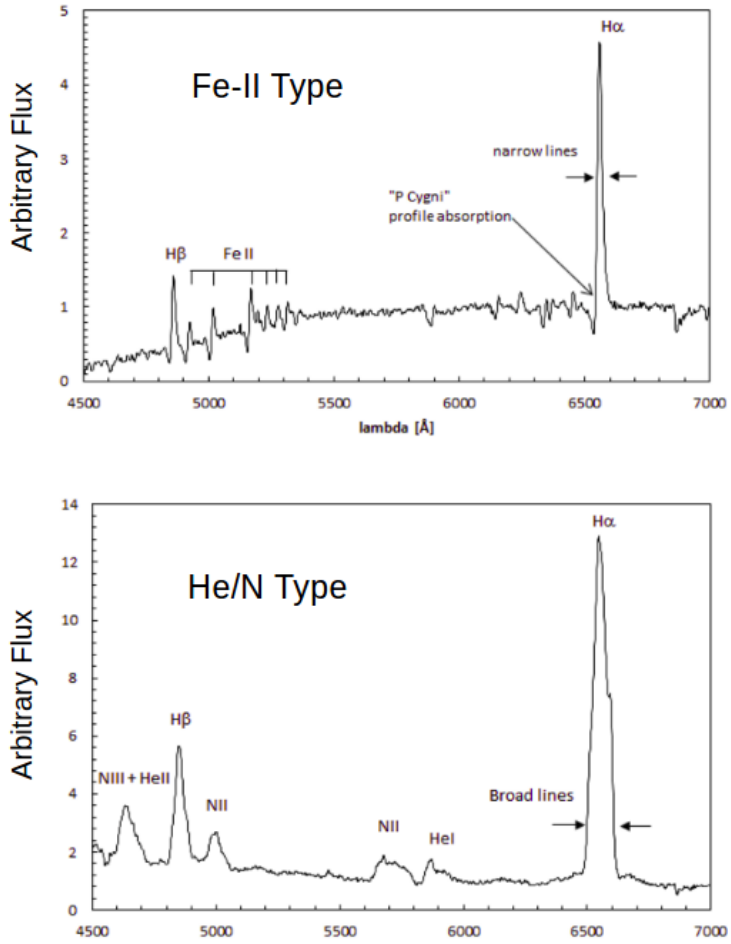


Figure 1.3 Examples of the two different nova spectral classes, with the most prominent features labeled. *Top:* example spectrum from an Fe-II type nova (this specific nova is V496 Sct). Note the relatively narrow spectral features and the characteristic P-Cygni profile. *Bottom:* example spectrum of an He N type nova (this specific nova is KT Eri). Note the much broader spectral features. It is still unclear what exactly is the physical mechanism responsible for the differences in the spectra. Taken from the website of an amateur astronomer, Francois Teyssier (`http://www.astronomie-amateur.fr/feuilles/Spectroscopie/NewStars.html`).

### 1.1.2 Radio Observations of Classical Novae

Historically, it has only been within the last half-century that radio observations of classical novae has been possible (Hjellming & Wade, 1970; Seaquist & Palimaka, 1977; Hjellming et al., 1979). The vast majority of the observations have been made by our group in the last decade, using the (upgraded in 2011) Karl G. Jansky Very Large Array. As our research group specializes in just such nova observations, we will spend a greater amount of time detailing observations in the radio, compared to other wavelength regimes.

#### 1.1.2.1 Thermal Emission

The benefits of radio observations stems from the fact that the primary emission mechanism—bremsstrahlung or free-free radiation—does not require a detailed calculations of the abundance and ionization states of different elements. Free-free radiation just depends on bulk properties of the emitting material; namely, the temperature, electron density, and average level of ionization. Because of this inherent simplicity, deriving density is relatively straightforward.

We model the ejecta as being an expanding shell of thermally emitting plasma; initially, the gas is almost completely optically thick at radio frequencies. However, as the shell expands and becomes more diffuse, the outer portions start to become optically thin—at that time the radio photosphere stops expanding and then begins to shrink (Hjellming & Wade, 1970). This is the same type of evolution that we discussed in Section 1.1.1.1, which dealt with the optical.

The amount of time it takes for the shell to become optically thin, and the speed at which it becomes optically thin, is determined by the density profile of the shell. We can utilize this to determine the density—and, therefore, the mass—of the ejecta (see, e.g., Wright & Barlow 1975; Hjellming et al. 1979).

We model a radio spectrum by fitting it to a power-law, i.e. we stipulate that $S_\nu \propto \nu^\alpha$, where $\nu$ is the frequency, $S_\nu$ is the flux at frequency $\nu$, $\alpha$ is the spectral index. For our model, we assume that the emission is a blackbody; specifically, we are working in the Rayleigh-Jeans tail (i.e. where $kT \gg h\nu$, and the blackbody function is a simple power-law) (Seaquist & Palimaka, 1977; Hjellming et al., 1979). An optically thick blackbody should have a spectral index of $\alpha = 2$, while optically thin free-free emission should have a spectral index of $\alpha \simeq -0.1$ (for $h\nu \ll kT_e$.

Thanks to interferometric observations, radio observations can also be used to determine properties of the ejecta geometry (e.g. angular size and symmetry), as some novae can have resolved radio imaging at late times.

#### 1.1.2.2 Non-Thermal Emission

Radio can also be used to probe shocks in novae, as we would expect to see non-thermal (usually synchrotron) emission at shock fronts. We expect the flux of non-thermal radiation to have a negative spectral index (i.e. $\alpha < 0$). Therefore, we expect the radio flux to be brighter at low-frequencies.

Shocks lead to magnetic field amplification; the magnetic field amplification can then lead to relativistic particle acceleration and the accelerated electrons emit (non-thermal) synchrotron emission (Chevalier, 1982, 1998). As a result, non-thermal emission can be used as another tracer of shock interactions; further, thanks to Very Long Baseline Interferometry (VLBI) radio observation techniques, this non-thermal emission can be imaged.

Non-thermal emission from this type of shock interaction was originally suspected in novae with a giant secondary (e.g. Hjellming et al. 1986; Kantharia et al. 2016). The primary reasoning for this was the exceptionally large brightness temperature (that is, the temperature necessary to explain the total flux from an object given its angular size and assuming the object is an optically thick blackbody emitter). Temperatures in excess of $\sim 10^5$ K strongly suggest that the emission is non-thermal in nature (Seaquist, 1989).

### 1.1.3 X-Ray

We will not go into as much detail on X-ray emission in this thesis, as V1324 Sco was not detected in the X-ray regime. We do give details here, however, about the information that X-ray observations can bring to the study of novae.

X-rays are utilized primarily in two facets in the studies of novae: as a diagnostic of shocks, and to characterize residual burning on the white dwarf once the ejecta becomes optically thin. We describe these two different sources of X-ray emission below. A X-ray light curve—paired with the corresponding optical light curve—can be seen in Figure 1.4.

#### 1.1.3.1 Hard X-Rays

The presence of hard ($\geq$ 1 keV) X-rays is believed to be thermal emission from shock-heated gas (see, e.g., Mukai & Ishida 2001; Bode et al. 2006). The simplest explanation for the presence of these shocks is if the companion in the nova system is a giant; the dense wind coming off of the giant provides an excellent target for the ejecta to slam into (Bode & Kahn, 1985). Indeed, we do detect hard X-ray emission in many novae with giant companions (see, e.g., Sokoloski et al. 2006; Nelson et al. 2012; Linford et al. 2017). O'Brien et al. (1994) argued, however, that the hard X-rays coming from V838 Her must be the result of different

ejecta components interacting with one another—that is, the shocks must be *internal* to the ejecta. The short orbital period of V838 Her ($\sim$ 7 hours) strongly disfavored a giant companion. This model was further confirmed with observations of V382 Vel, which *required* that the shocks be internal to the ejecta in order to explain the amount of absorption (Mukai & Ishida, 2001).

The spectra of these hard X-rays allows us to constrain the shock environment. The shock temperature gives information about the relative velocity and densities of the two shocking media, the amount of absorption tells us about the density of upstream gas, and the emission measure tells us about the density of the emitting gas. Hard X-rays are ubiquitous in novae with fast ejecta; Schwarz et al. (2011) found that *every* nova with FWHM $\geq$3000 km s$^{-1}$and observations within 100 days after visual maximum exhibited hard X-rays (in the sample that they were working with). Reciprocally, very few novae with slow ejecta in the sample of Schwarz et al. (2011) have shown signs of early hard X-ray emission.

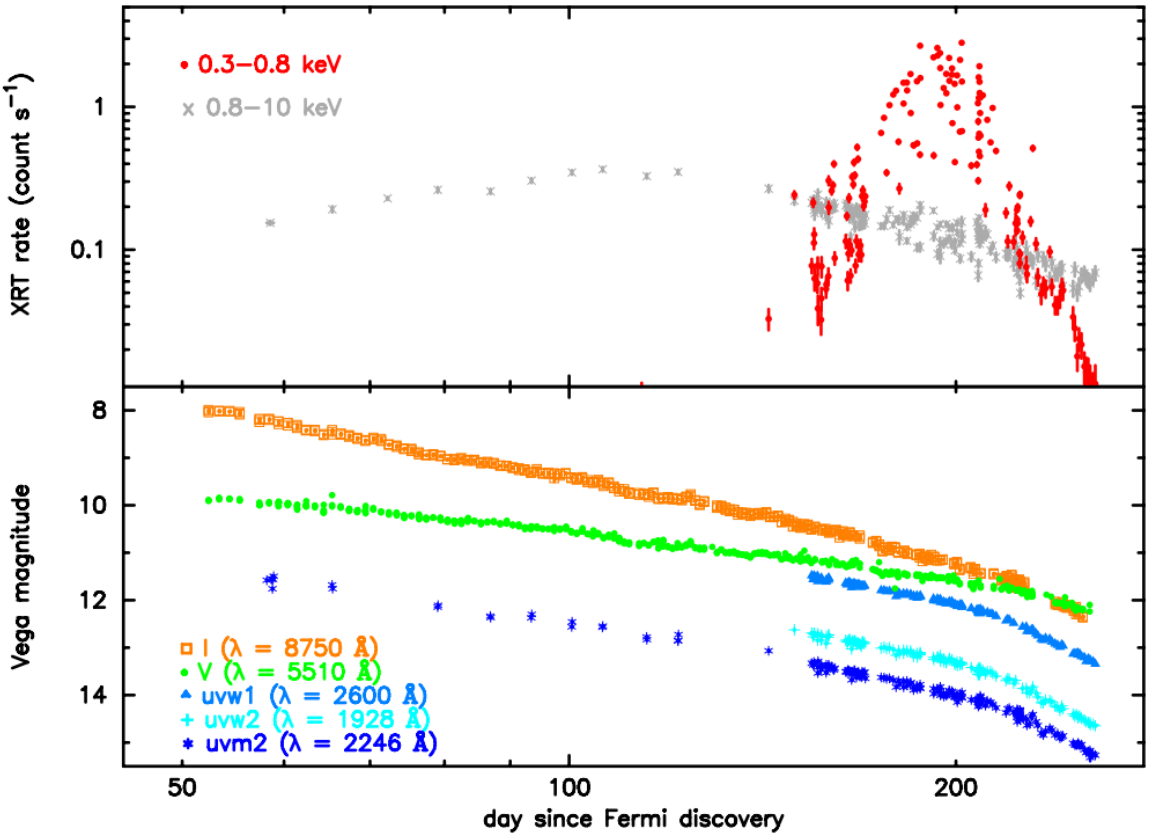


Figure 1.4 X-ray and optical light curves for the gamma-ray detected nova V959 Mon. *Top Panel:* The X-ray flux, given in count s$^{-1}$. The red points are the soft X-rays (<1 keV), while the grey points are the hard X-rays (>1 keV). *Bottom Panel:* Near-IR (orange), optical (green), and different near-UV (blues and teal) photometry. Note the persistent, low level, hard X-rays, as well as the delayed, but much brighter, soft X-rays that turn on around day $\sim$ 150. Taken from Page et al. (2013).

#### 1.1.3.2 Super Soft Source

The large amount of ejected material serves, effectively, as a shield, obscuring the still burning white dwarf surface. Once the ejecta become optically thin, though, the white dwarf surface is revealed. This emission from the white dwarf surface is usually modeled as a blackbody, with a temperature of order 40 eV (Schwarz et al., 2011). This new, much softer, X-ray source is referred to as a Super Soft Source (hereafter SSS).

The amount of time it takes for the SSS to "turn on" (i.e. become visible) is a measure of the total amount of material obscuring the white dwarf along the line of sight. This provides a lower-limit for the total amount of ejected material, as it implicitly assumes that the ejecta are spherically symmetric.

### 1.1.4 Gamma-Ray Novae

Nova outbursts have also been detected in the GeV gamma-ray regime with the *Fermi Gamma Ray Space Telescope* (see e.g. Cheung et al. 2010, 2012b,a; Hays et al. 2013; Cheung et al. 2015). The presence of gamma-rays imply that there are relativistic particles being generated in the nova event.

There are two potential processes for producing gamma-rays from relativistic particles: the leptonic process and the hadronic process. In the leptonic process, electrons are accelerated up to relativistic speeds. There are two potential mechanisms for producing the gamma-rays from the electrons. The first scenario involves photons inverse-Compton scattering off of the non-thermal electrons (Blumenthal & Gould, 1970). The second scenario involves the relativistic electrons emitting gamma-rays via bremsstrahlung radiation (Vurm & Metzger, 2016). In the hadronic process, it is ions that are being accelerated to relativistic speeds. These non-thermal protons then collide with a dense medium to produce $\pi^0$ mesons, which then decay to gamma-rays (Drury et al., 1994). The likely source of the accelerated particles is strong shocks, which can generate relativistic particles via the diffusive shock acceleration mechanism (Blandford & Ostriker, 1978; Metzger et al., 2014). The details of particle acceleration in novae still remains a poorly understood issue, despite the potential for insight into the broader topic of high-energy astrophysics (Metzger et al., 2015).

## 1.2 Classical Nova Theory

It was not until Kraft (1964) observed the binary nature of several old novae (i.e. several decades after outburst) that the current paradigm of classical novae—an accretion induced Thermonuclear Runaway (hereafter referred to as a TNR) on a White Dwarf (hereafter referred to as just WD)—was born (see Figure 1.5 for a representation of this model). In this section, we discuss the theoretical grounding for classical novae; in Section 1.2.1, we discuss the physical mechanism responsible for generating energy in a classical nova; in

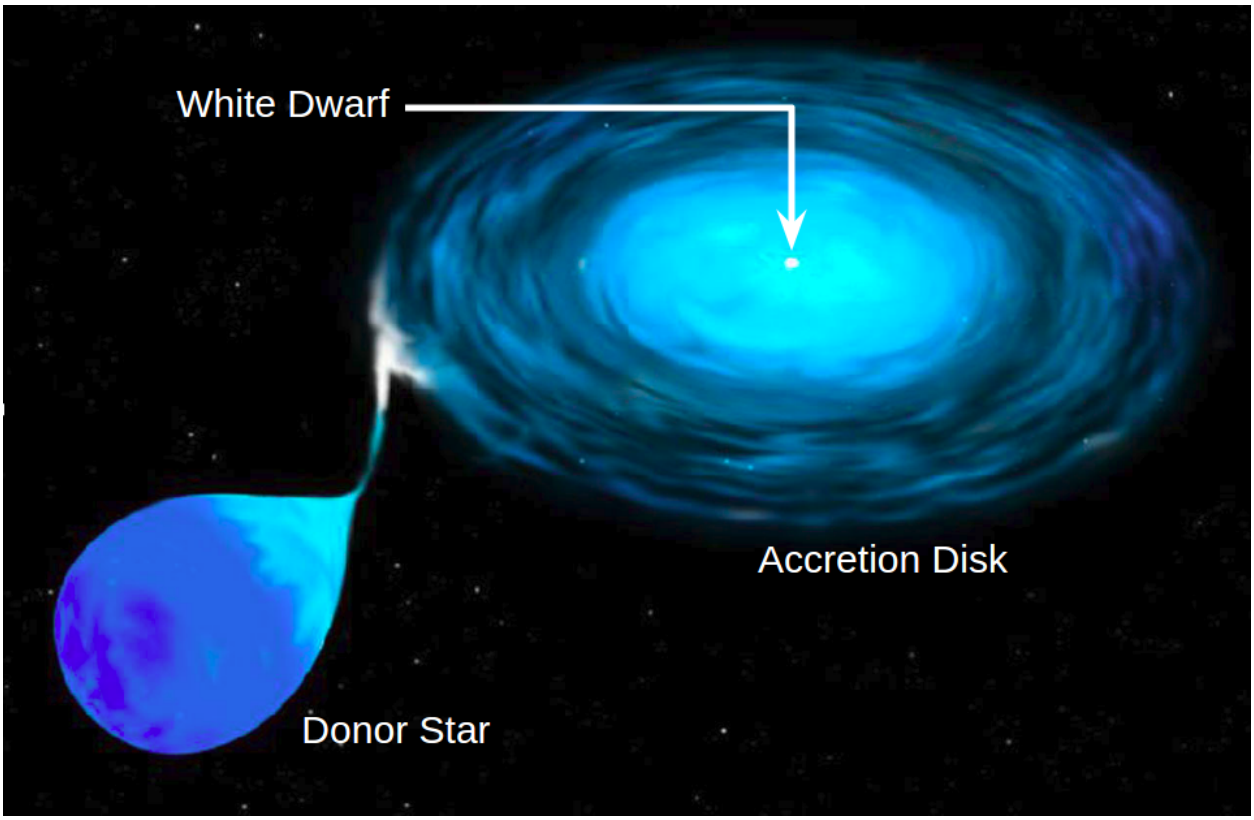


Figure 1.5 Visual representation of the cataclysmic variable model, the progenitors of novae. Mass is accreted from the donor star onto the white dwarf, via the accretion disk. This material piles up on the surface of the white dwarf; enough material is accreted for fusion to ignite; it is this fusion that powers the nova outburst. Image Credit: Space Telescope Institute.

Section 1.2.2 we discuss how the energy generated translates into mass ejected from the system; finally, in Section 1.2.3, we discuss the differences in nova systems that give rise to the variations we see (e.g. ejecta mass, ejecta velocity, etc).

### 1.2.1 Thermonuclear Runaway

The nuclear energy driving a nova is generated via the fusion of $^4$He from four $^1$H atoms. During accretion there may be some some low-level of hydrogen burning going on at the base of the envelope. Due to the relatively low temperature and density, the $p-p$ chain process dominates the energy generation (José & Hernanz, 1998; Starrfield et al., 2016). As the envelope begins to heat up, the cold CNO cycle—which utilizes Carbon, Nitrogen, and Oxygen to catalyze the production of helium—starts to dominate the nuclear energy production. The cold CNO cycle dominates at temperatures between $2 \times 10^7$ to $4 \times 10^8$ K. At the peak of the nuclear burning, though, the *hot* CNO cycle dominates the energy production; this process is similar to the cold CNO cycle, except the high temperatures allow for some elements that would otherwise be waiting

to beta-decay undergo a proton capture instead, opening up new nuclear reaction channels and speeding up the nuclear burning process. This is not to say that the reactions no longer depend on beta-decays, just that the time for the beta-decays to occur will be shorter than in the cold CNO cycle (Wiescher et al., 2010).

During the nuclear burning, there is a need for alpha-capture elements to be enriched beyond solar metallicity in order to catalyze the CNO-cycle or the nuclear energy generation will stall due to too many elements being trapped in $\beta^+$-unstable nuclei (Starrfield et al., 1972). Note that it is this isotope trapping that will, ultimately, stall and shut off the nuclear energy generation (Gallagher & Starrfield, 1978). In order for the nuclear energy generation to not stall too early, the material in the envelope must be CNO enriched. To do this, there must be convection within the envelope during the TNR, to mix CNO-enriched material in with the accreted gas (Starrfield et al., 1974). Simulating novae outbursts, Yaron et al. (2005) were able to initiate a TNR with envelope enrichment values between $Z \sim 0.02$ all the way up to $Z \sim 0.63$ (starting from solar metallicity of $Z \sim 0.01$).Schwarz et al. (2007) did a study of two fast novae—V4160 Sgr and V838 Her—and fit optical spectra their to estimate elemental abundances. They found a large overabundance of nitrogen (factor of $\sim 30$ to 150 above solar), neon (factor of $\sim 50$ above solar), sulfur (factor of $\sim 30$ above solar), and oxygen (factor of $\sim 20$). The other overabundances were more modest, with carbon and silicon being a factor of 5 over solar, and helium, oxygen, magnesium, and iron all being less than a factor of 2 above solar. We can learn a great deal about the nova process from these kinds of enrichment studies. It was the enrichment of sulfur and the relatively depleted carbon suggests that the nuclear burning regions became hot enough ($\geq 5 \times 10^8$ K) for there to be *alpha* capture reactions, something that wasn't predicted by simulations (Schwarz et al., 2007) .

At about $7 \times 10^7$ K, the degeneracy begins to lift and the outer envelope begins to expand and cool (Starrfield et al., 2016). However, by this time, the temperature is increasing too rapidly, and the TNR occurs. It is possible for the TNR to be throttled by one of two effects: (1) a large fraction of the material being locked into isotopes with a long beta decay time—e.g. $^{15}$O, with a decay time of $\sim 2$ minutes—or (2) material being convectively mixed (or diffusing) to cooler regions of the envelope, where the nuclear reactions proceed at a much slower rate—e.g. going from $10^8$ K to $5 \times 10^7$ K decreases the $^{15}\mathrm{N}(p,\alpha)^{12}\mathrm{C}$ reaction rate by nearly four orders of magnitude (based on the best fit parameters for the reaction found in the JINA Reaction Library[2]).

Because of their strong dependency on nuclear reaction rates—such as the one described above—classical novae offer a unique laboratory for putting nuclear astrophysics to the test.

[2] `https://groups.nscl.msu.edu/jina/reaclib/db/n15(p,a)c12/nacr/`

### 1.2.2 Mass Loss

Immediately after the ignition of the TNR, the initial nuclear power generation deposits a great deal of energy in the outer envelope, accelerating material well above the thermal sound speed. This produces a shock wave, which ejects just the outer envelope (Prialnik, 1986). However, this is thought to be only a small fraction of the total mass ejected during the nova event (Prialnik, 1986). How the majority of the mass is ejected is still an open question.

The primary issue with mass loss in novae is that—in order for the mass to be ejected—a great deal of (nominally) thermal energy needs to be converted into kinetic energy before it gets radiated away. The engine that drives novae is the nuclear burning, which generates a great deal of *thermal* energy. The massive increase in thermal energy will make the envelope bloat—similar to a giant—but there needs to be an extra push to actually *eject* the mass. There are three primary theories for the source of this extra push.

- **Radiative Pressure:** The canonical picture of nova posits that the mass loss is primarily driven by radiation pressure (Bath & Shaviv, 1976). After the initial percussive mass ejection there follows a more phase of continuous, radiatively-driven, mass loss. This will slowly, but steadily, push material off of the surface of the WD.
- **Binary Interaction:** Recent evidence suggests that it is possible that the mass loss is being assisted by dynamical friction, between the ejecta and the orbiting stars in the binary, injecting energy into the ejecta. Chomiuk et al. (2014) used radio imaging to show that there were two different ejecta components—perpendicular to one another—in V959 Mon. Such a phenomenon has a solid grounding in theoretical work (see, e.g., Livio et al. 1990; Lloyd et al. 1997). It was predicted to be the result of the binary motion injecting energy and increasing the velocity of material moving parallel to the orbital plane of the binary (the first component), while the (relatively) slower moving material expands perpendicular to the orbital plane (second component).
- **L2 Mass Loss:** It is also possible that, at this time, the mass lost is being funneled out of the L2 Lagrangian point of the system (Pejcha et al., 2016).

There is still a great deal of work that needs to be done in order to determine the specific mechanism for mass-loss in novae.

### 1.2.3 Variations Between Novae

We know that there are variations between the observable features of CNe, such as mass and velocity of the ejecta. It has been found that just three parameters can explain the entirety of this variance: mass accretion

rate, WD mass, and WD surface temperature (Kovetz & Prialnik, 1985; Prialnik, 1986; Yaron et al., 2005). In this section, we describe how each of these variables affects the observable properties of a nova. Note that it has been shown that the mass accretion rate is directly related to the orbital period of the binary system (Rappaport et al., 1983; Patterson, 1984), meaning that at least one of these three properties can be estimated before the nova event, assuming there is pre-outburst data for the system.

The WD mass determines the surface pressure, with a more massive WD having a higher surface pressure; as a result, a larger WD mass will require a smaller amount of accreted material for ignition.

All nova simulations start in an initial state where the base of the envelopes are hot and dense enough for $p - p$ chain reactions to occur; however, the primary source of heating is the compressional heating of newly accreted material (Starrfield et al., 1972; Prialnik, 1986; José & Hernanz, 1998; Yaron et al., 2005). A higher accretion rate will increase the heating and therefore bring about a TNR more rapidly than a lower accretion rate, shortening the time between successive nova events.

For cold WDs, heat conduction into the core saps energy, and therefore delays ignition; an already hot WDs can have a convective envelope that enhances the mixing process, hastening the onset of TNR (Prialnik & Kovetz, 1995).

The initial surface temperature at the onset of accretion also sets the level of degeneracy on the surface of the WD (Yaron et al., 2005). A higher surface temperature means that the gas in the envelope will be less degenerate. At the highest surface temperatures, degeneracy is lifted and there is stable hydrogen burning on the surface of the WD (Townsley & Bildsten, 2004; Shen & Bildsten, 2007). A nova can never occur in such a system, as the accreted material does not have a chance to pile up. Note that Townsley & Bildsten (2004) found that, under ideal conditions, it is possible for the WD core to reach a steady-state temperature. This, in turn, would set the initial surface temperature of a post-nova WD when accretion resumes.

All novae are expected to be recurrent—that is, have multiple CNe events—but they have a wide spread in the amount of time between successive classical nova events (hereafter referred to as the recurrence time). The recurrence time is set by the rapidity with which the system can be set up for another nova event; that is, how fast can the WD be set up for another TNR. As a result, the recurrence time is set by the same three variables discussed in Section 1.2.3: WD mass, WD surface temperature, and accretion rate. In this case, the accretion rate also plays a vital role in setting the time-scale for mass accumulation, not just surface heating.

To summarize, we can draw a broad strokes picture of how different variables affect novae. Specifically, we see that a higher surface temperature, a larger mass, and a higher accretion rate, all shorten the recurrence time, decrease the amount of mass ejected, and decrease the ejecta velocity. So increasing any one of these variables (temperature, mass, accretion rate) will make the nova event less violent.

## 1.3 Introduction to V1324 Sco and This Work

### 1.3.1 A New Paradigm

The work presented in this thesis is focused (primarily) on a very in-depth study of a specific gamma-ray detected nova—V1324 Sco. Gamma-ray detected novae are a relatively new class of transient, with the first—V407 Cyg—being discovered in 2010 (Abdo et al., 2010). V407 Cyg is a rather special system, though, having a Mira giant companion (a Mira giant is a red pulsating star on the asymptotic giant branch). As a result, there was a relatively simple explanation for the gamma-rays: the nova ejecta slammed against the dense wind coming from the Mira companion (see Figure 1.6), the shock led to non-thermal particle acceleration, and these non-thermal particles were the seeds for the gamma-ray production (Abdo et al., 2010).

This model, however, could not explain subsequent novae detected by *Fermi*: V1324 Sco, V959 Mon, V339 Del (Ackermann et al., 2014), V1369 Cen and V5668 Sgr (Cheung et al., 2016), almost all of which do not have a detectable red-giant companion (see, e.g., Finzell et al. 2015; Munari et al. 2013; Munari & Henden 2013; Hornoch 2013; the progenitor of V5668 Sgr has yet to be determined). Without the presence of a giant companion, there is no obvious external material for the ejecta to shock against.

It is in fact much more likely that the shocks are being produced within the ejecta, due to different components of the ejecta colliding with one another (internal shocks). There has already been long standing evidence for internal shocks in classical novae from X-ray observations (Mukai & Ishida, 2001; Drake et al., 2016). However, some asymmetry in the mass ejection mechanism is necessary in order to generate internal shocks (see Figure 1.7). One idea put forward by Chomiuk et al. (2014) is that there is a common envelope phase during the mass ejection, resulting in a density enhancement in the binary orbital plane. A separate, slow, and diffuse wind propagates in the polar direction (i.e. perpendicular to the orbital plane). When these two outflows—dense equatorial and diffuse polar—collide with one another, they produce shocks.

Progress has been made on the theoretical front, by constraining the conditions necessary for both the thermal emission (Metzger et al., 2014) and non-thermal emission (Vlasov et al., 2016; Metzger et al., 2016) observed in gamma-ray detected novae. Work done in Metzger et al. (2015) found that a significant fraction ($> 10\%$) of the bolometric light should be coming from shock emission. However, there has been little in the way of in-depth, multi-wavelength, analysis of these gamma-ray novae on the observational side, to constrain the properties of the shock.

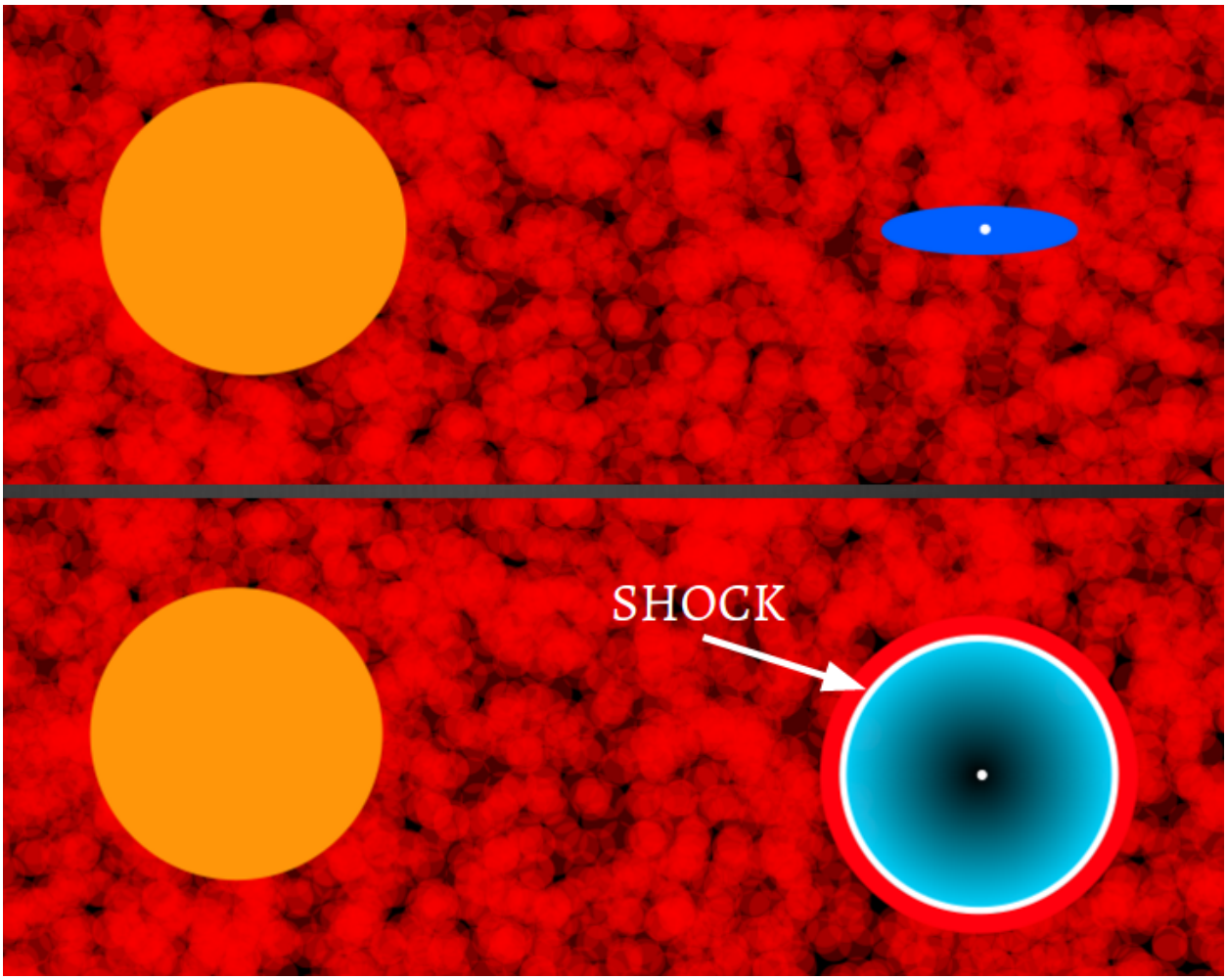


Figure 1.6 A visual representation of external shocks. In this model, the companion/donor star has evolved off the main-sequence into the giant branch. The wind from the companion causes there to be a dense medium surrounding the white dwarf. When the white dwarf goes into outburst, the nova ejecta immediately slams into this dense medium, generating a shock. This type of model can explain gamma-ray novae like V407 Cyg.

### 1.3.2 V1324 Sco: A Brief Primer

V1324 Sco was (arguably) the first of this new class of gamma-ray detected novae. It was first detected in April of 2012. It was initially classified as a candidate microlensing event. Once it was discovered to be a classical nova, it was brought to the attention of the transient community through an Astronomers Telegram (ATEL) (Wagner et al., 2012). Approximately one month after the first announcement of V1324, another ATEL was published concerning a transient discovered by *Fermi* in the galactic bulge, and its possible association with the nova referred to as Nova Sco 2012. V1324 Sco was the first gamma-ray detected nova with a main-sequence companion—beating V959 Mon by just a few days. Upon the publication of Ackermann

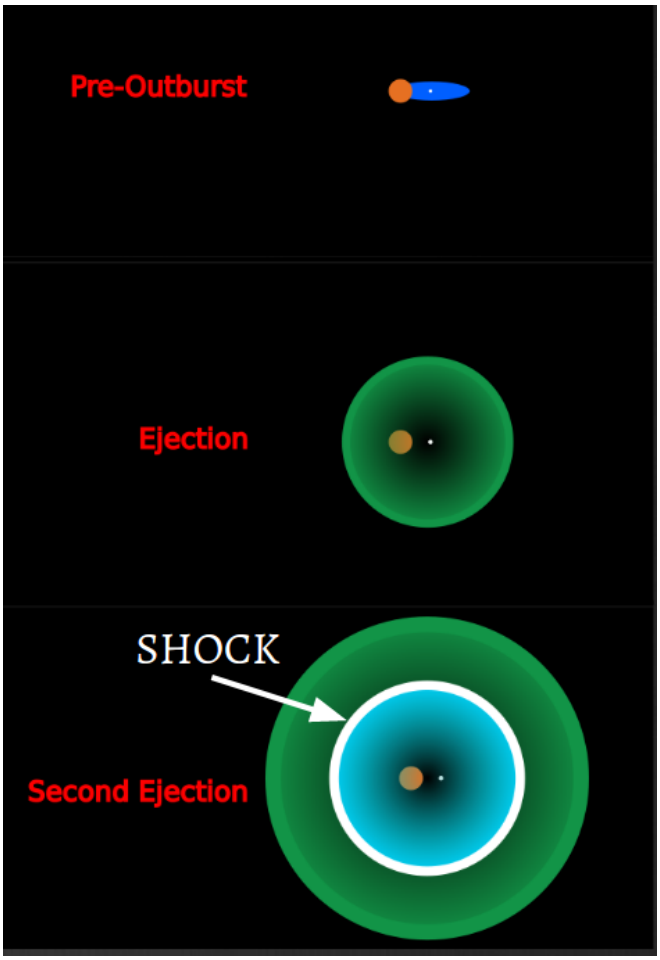


Figure 1.7 Visual representation of a potential internal shock model. In this scenario, the white dwarf goes into outburst and ejects material; this is followed by a *secondary* ejection of material, which is moving faster than the first ejection. The faster moving secondary ejection catches up to the first ejection and slams into it, causing a shock. Note that this is one potential model for how to generate internal shocks, and that other models have been proposed (see, e.g., Chomiuk et al. 2014).

et al. (2014), it was found that V1324 Sco was the most gamma-ray luminous classical nova. Being the extreme case, V1324 Sco became *the* test bed for studies of the gamma-ray emission process in classical novae.

### 1.3.3 This Work

In the forthcoming chapters we present all of the research carried about by the author as part of their doctoral program. Chapters 2, 3, and 4 draw heavily from Finzell et al. (2015) and Finzell et al. (2017); further, Section 3.6 draws from work contributed to Metzger et al. (2015). This work is primarily focused on V1324 Sco; we present a very large, multi-wavelength, dataset in Chapter 2; in Chapter 3, we analyze said dataset, and derive (or put limits on) the physical parameters of this system; in Chapter 4, we posit a

potential difference between V1324 Sco and other classical novae that could explain the exceptional gamma-ray luminosity; finally, in Chapter 5, we conclude by giving a brief overview of all of the physical parameters found for V1324 Sco and the implications for the future study of classical novae.

# 2 Data

## 2.1 UV/Optical/Near-IR Photometry

### 2.1.1 Observations and Reduction

V1324 Sco—located at RA:267.72458 and DEC: −32.62236(J2000)—falls within one of the fields that the Microlensing Observations in Astrophysics (MOA) Collaboration continually observe with the MOAII 1.8 meter telescope at Mt. Johns Observatory in New Zealand. V1324 Sco was initially detected in 2012 April by their high-cadence $I$-band photometry (Wagner et al., 2012). The initial detection showed a slow monotonic rise in brightness between April 13 - May 31 (see Figure 2.1), followed by a very large increase in brightness starting June 1 (Wagner et al., 2012). We will take 2012 June 1 to be day 0. We also adopt the convention throughout this paper that all dates with − or + denote days before or after 2012 June 1, respectively.

All initial high-cadence observations, taken as part of the regular MOA program, were taken in the $I$-broad band (corresponds to a sum of the standard Cousins $R$ and $I$-bands; Sumi et al. 2016), and were reduced using standard procedures (see Bond et al. 2001 for details). The MOA survey emphasizes rapid imaging of the Galactic bulge fields. On a clear night an individual field will be reimaged every $\sim$ 40 minutes. The result of this high time cadence photometry can be seen in Figure 2.1. It should be noted that the primary purpose of the high-cadence observations is difference imaging. As a result, the individual apparent magnitude values should only be used to measure changes, not as an absolute measurement (Bond et al., 2001).

After the steep optical rise, a follow up campaign was triggered by the MicroFUN group[1] who believed that the transient could be a potential microlensing event. Apart from the standard $I$-broad band filter, the MicroFUN follow up observations also used $V$ and $I$ Bessel filters. Other observations were made in $B$, $V$, and $I$ filters using the Small & Moderate Aperture Research Telescope System (SMARTS) 1.3 Meter telescope (Cerro Tololo Inter-American Observatory) and Auckland Observatories.

Along with the MOA and MicroFUN data we also present multi-color photometry from Fred Walter's ongoing Stony Brook/SMARTS Atlas of (mostly) Southern Novae (see Walter et al. 2012 for further information on this dataset), as well as data from American Association of Variable Star Observers (AAVSO)[2]. The SMARTS data uses the ANDICAM instrument on the 1.3 meter telescope, and provide both optical ($B$, $V$, $R$, $I$) and near-IR ($J$, $H$, $K$) filters going from day +35 to day +124, while the AAVSO data use

[1] http://www.astronomy.ohio-state.edu/~microfun/
[2] https://www.aavso.org/data-download

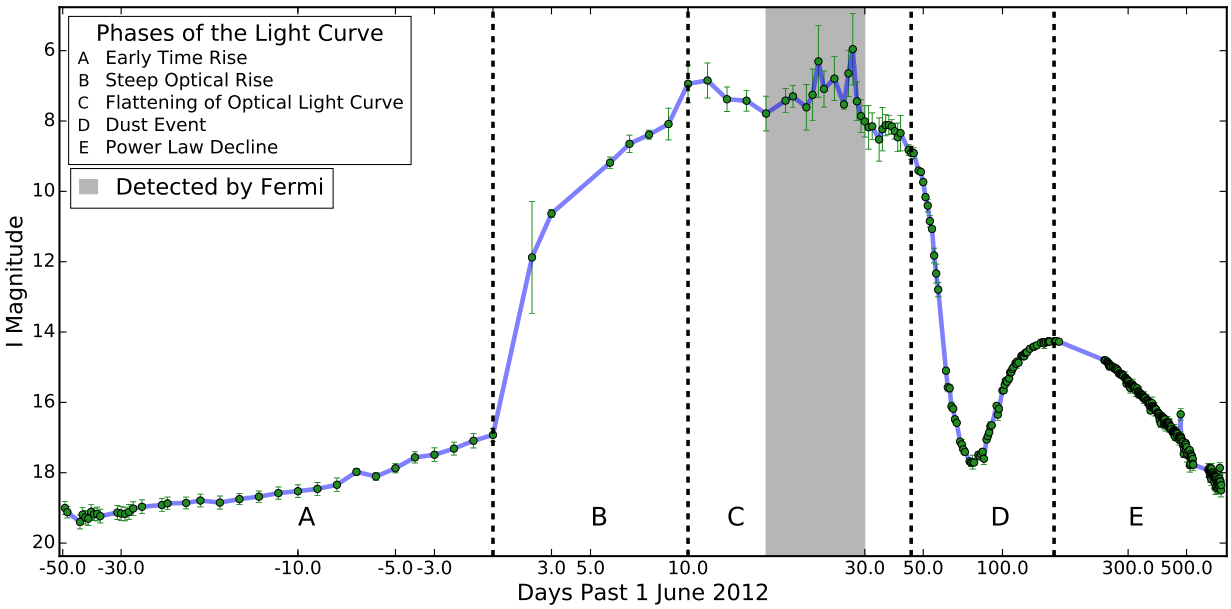


Figure 2.1 $I$ band light curve for V1324 Sco, generated using the MOA data set. The plot starts 49 days before primary optical rise, at the first date where a *single* observation (as opposed to a stacked observation) yields a $5\sigma$ detection. The dashed lines delineate the different phases of the light curve evolution, as described in Section 2.1. The gray shaded region denotes the time period where V1324 Sco was detected in gamma-rays. Thanks to the extremely well-sampled MOA data set we can see all of the different evolutionary phases of the optical light curve, as discussed in section 2.1.2. Note, that the X-axis takes the date of the primary optical rise (2012 June 1) to be day 0, so the plot starts on a negative value.

optical ($V$, $B$, $R$) filters, and go from day +7 to day +445.

Finally, we incorporate the UV data taken contemporaneously with the X-ray observations. The UV data comes from the Ultraviolet/Optical Telescope (UVOT; see Roming et al. 2005 for further details) on board *Swift*. Each observation was taken using the UVM2 filter, which is centered on 2246 Å and has a FWHM of 498 Å (Poole et al., 2008). These observations were taken at the same time as the X-ray observations (see Section 2.3), stretching from day +22 to day 520; however, we only include observations where V1324 Sco was detected.

A portion of the UV/optical/near-IR photometric data set is presented in Table 2.1; the entire data set can be found in the online publication[3]. Note that no attempt has been made to standardize the photometry from different observatories.

### 2.1.2 Timeline of the Optical Light curve

We present an overview of the different phases in the evolution of the optical light curve to help orient the reader to the different qualitative variations. These different phases come from the classification scheme laid

[3] `https://opennova.space/`

Table 2.1. Table of Photometric Data

| Observation Date | JD | $t - t_0$[a] (Days) | Filter | Mag | Mag Error | Observer/Group | Telescope/Specific Filter[b] |
|---|---|---|---|---|---|---|---|
| 2012 Apr 13 | 2456030.07502 | -48.92499 | I | 18.700 | 0.150 | MOA | MJUO-Ibroad |
| 2012 Apr 13 | 2456030.95591 | -48.04410 | I | 18.770 | 0.090 | MOA | MJUO-Ibroad |
| 2012 Apr 13 | 2456030.95714 | -48.04287 | I | 18.590 | 0.090 | MOA | MJUO-Ibroad |
| 2012 Apr 13 | 2456030.99663 | -48.00338 | I | 18.800 | 0.110 | MOA | MJUO-Ibroad |
| 2012 Apr 14 | 2456031.05194 | -47.94807 | I | 18.760 | 0.090 | MOA | MJUO-Ibroad |
| 2012 Apr 14 | 2456031.06304 | -47.93697 | I | 18.900 | 0.110 | MOA | MJUO-Ibroad |
| 2012 Apr 14 | 2456031.07414 | -47.92587 | I | 18.850 | 0.090 | MOA | MJUO-Ibroad |
| 2012 Apr 14 | 2456031.08652 | -47.91348 | I | 18.860 | 0.110 | MOA | MJUO-Ibroad |
| 2012 Apr 14 | 2456031.09762 | -47.90238 | I | 19.030 | 0.110 | MOA | MJUO-Ibroad |
| 2012 Apr 14 | 2456031.10976 | -47.89024 | I | 18.660 | 0.070 | MOA | MJUO-Ibroad |
| 2012 Apr 14 | 2456031.12211 | -47.87789 | I | 18.930 | 0.120 | MOA | MJUO-Ibroad |
| 2012 Apr 14 | 2456031.13321 | -47.86679 | I | 18.890 | 0.100 | MOA | MJUO-Ibroad |
| 2012 Apr 14 | 2456031.14435 | -47.85566 | I | 18.830 | 0.100 | MOA | MJUO-Ibroad |
| 2012 Apr 14 | 2456031.15670 | -47.84331 | I | 18.860 | 0.090 | MOA | MJUO-Ibroad |
| 2012 Apr 14 | 2456031.16781 | -47.83220 | I | 18.950 | 0.110 | MOA | MJUO-Ibroad |
| 2012 Apr 14 | 2456031.17893 | -47.82108 | I | 18.890 | 0.090 | MOA | MJUO-Ibroad |
| 2012 Apr 14 | 2456031.19127 | -47.80874 | I | 18.910 | 0.090 | MOA | MJUO-Ibroad |
| 2012 Apr 14 | 2456031.20237 | -47.79764 | I | 18.880 | 0.120 | MOA | MJUO-Ibroad |
| 2012 Apr 14 | 2456031.21348 | -47.78653 | I | 18.850 | 0.090 | MOA | MJUO-Ibroad |
| 2012 Apr 14 | 2456031.22585 | -47.77416 | I | 18.880 | 0.100 | MOA | MJUO-Ibroad |
| 2012 Apr 14 | 2456031.23825 | -47.76176 | I | 18.750 | 0.090 | MOA | MJUO-Ibroad |
| 2012 Apr 14 | 2456031.25182 | -47.74818 | I | 18.870 | 0.090 | MOA | MJUO-Ibroad |
| 2012 Apr 14 | 2456031.96000 | -47.04001 | I | 18.610 | 0.080 | MOA | MJUO-Ibroad |
| 2012 Apr 14 | 2456031.96123 | -47.03877 | I | 18.700 | 0.080 | MOA | MJUO-Ibroad |
| 2012 Apr 14 | 2456031.99908 | -47.00093 | I | 18.880 | 0.120 | MOA | MJUO-Ibroad |
| 2012 Apr 15 | 2456032.05184 | -46.94817 | I | 18.740 | 0.100 | MOA | MJUO-Ibroad |
| 2012 Apr 15 | 2456032.07405 | -46.92596 | I | 18.840 | 0.130 | MOA | MJUO-Ibroad |
| 2012 Apr 15 | 2456032.08742 | -46.91258 | I | 18.920 | 0.100 | MOA | MJUO-Ibroad |
| 2012 Apr 15 | 2456032.09855 | -46.90146 | I | 18.810 | 0.100 | MOA | MJUO-Ibroad |
| 2012 Apr 15 | 2456032.10966 | -46.89035 | I | 18.770 | 0.090 | MOA | MJUO-Ibroad |
| 2012 Apr 15 | 2456032.12200 | -46.87801 | I | 18.880 | 0.150 | MOA | MJUO-Ibroad |
| 2012 Apr 15 | 2456032.13311 | -46.86690 | I | 18.740 | 0.100 | MOA | MJUO-Ibroad |
| 2012 Apr 15 | 2456032.14421 | -46.85580 | I | 18.850 | 0.100 | MOA | MJUO-Ibroad |
| 2012 Apr 15 | 2456032.15655 | -46.84346 | I | 18.740 | 0.090 | MOA | MJUO-Ibroad |
| 2012 Apr 15 | 2456032.16869 | -46.83132 | I | 18.780 | 0.090 | MOA | MJUO-Ibroad |
| ... | ... | ... | ... | ... | ... | ... | ... |

Note. — All of this data, as well data from both AAVSO and Walter et al. (2012), can be found online at `https://openmova.space/`

[a]Taking $t_0$ to be 1.0 June 2012

[b]This is a key for the different facilities used by the MOA and MicroFUN groups. **MJUO**: Mt. John University Observatory; **AUCK**: Auckland Observatory; **CTIO**: SMARTS 1.3 Meter Telescope.

Table 2.2. Optical Spectroscopic Observations

| UT Date | $t - t_0$ (Days) | Observer | Telescope | Instrument | Dispersion (Å) | Wavelength Range (Å) |
|---|---|---|---|---|---|---|
| 2012 Jun 04.0 | +3.0 | Bensby | VLT | UVES | 0.02 | 3700 – 9500 |
| 2012 Jun 08.5 | +7.5 | Bohlsen | Vixen VC200L | LISA | 0.5 | 3800 – 8000 |
| 2012 Jun 14.5 | +13.5 | Bohlsen | Vixen VC200L | LISA | 0.5 | 3800 – 8000 |
| 2012 Jun 18.5 | +17.5 | Bohlsen | Vixen VC200L | LISA | 0.5 | 3800 – 8000 |
| 2012 Jun 20.9 | +19.9 | Buil | 0.28m Celestron | LISA | $\sim 0.6$ | 3700 – 7250 |
| 2012 Jun 21.2 | +20.2 | Walter | SMARTS 1.5m | RC | $\sim 5.5$ | 3240 – 9500 |
| 2012 Jun 23.1 | +22.1 | Walter | SMARTS 1.5m | RC | $\sim 1.0$ | 5620 – 6940 |
| 2012 Jun 24.9 | +24.9 | Buil | 0.28m Celestron | LISA | 6.2 | 3700 – 7250 |
| 2012 Jun 25.1 | +24.1 | Walter | SMARTS 1.5m | RC | $\sim 1.5$ | 3650 – 5420 |
| 2012 Jul 03.0 | +32.0 | Walter | SMARTS 1.5m | RC | $\sim 1.5$ | 3650 – 5420 |
| 2012 Jul 07.1 | +36.1 | Walter | SMARTS 1.5m | RC | $\sim 1.0$ | 5620 – 6940 |
| 2012 Jul 11.1 | +40.1 | Walter | SMARTS 1.5m | RC | $\sim 5.5$ | 3240 – 9500 |
| 2012 Jul 15.0 | +44.0 | Walter | SMARTS 1.5m | RC | $\sim 1.0$ | 5620 – 6940 |
| 2012 Jul 16.1 | +45.1 | Chomiuk | Clay Magellan | MIKE | 0.035 | 3700 – 9200 |
| 2012 Jul 19.0 | +48.0 | Walter | SMARTS 1.5m | RC | $\sim 5.5$ | 3240 – 9500 |
| 2013 May 20.0 | +353.0 | Wagner | LBT | MODS1 | $\sim 3.5$ | 3420 – 10000 |
| 2013 Aug 04.0 | +450.0 | Chomiuk | SOAR | Goodman | $\sim 1.0$ | 3000 – 7000 |

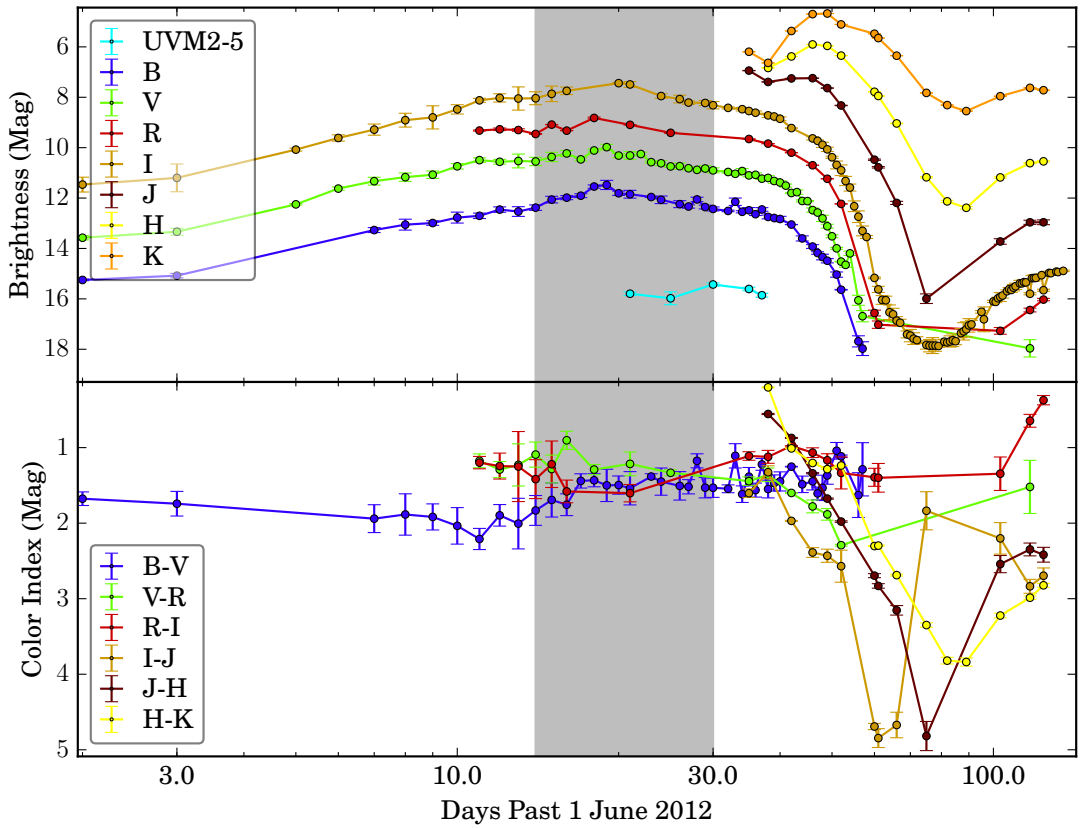


Figure 2.2 Top panel: Light curves of V1324 Sco in the optical/near-IR bands. Bottom panel: Evolution of optical and near-IR colors. The gray shaded region denotes the time period when V1324 Sco was detected in gamma-rays. Note that this plot has significantly worse time resolution than in Figure 2.1. Using this figure we can see how the dust event hits the bluer bands first and then moves to redder wavelengths as time progresses. We can also see that the dust event caused a drop in brightness all the way out to the near-IR ($JHK$) wavelength regime.

out in Strope et al. (2010)—with the exception of the early time rise. Throughout this overview we will reference Figure 2.1, which shows the light curve generated from the MOA data set. We will also reference Figure 2.2—which shows the light curve for multiple photometric bands as well as the color evolution—whenever there is multi-band photometry for a given evolutionary phase.

### 2.1.3 Early Time Rise (Days −49 to 0)

The first MOA $5\sigma$ detection of V1324 Sco occurred on 2012 April 13. Following this, there was a monotonic increase in brightness that lasted until 31 May 2012. The total increase in brightness during this period was $\Delta I \approx 2.5$ mags (about $\sim 0.05$ mags per day). This can be seen as phase A of Figure 2.1.

This type of early time rise has been observed only once before—in V533 Her (Robinson, 1975)—but

no theory was put forward to explain it. This lack of early time rise data is quite likely a selection effect; most early time information for novae comes from the Solar Mass Ejection Imager (SMEI) (Hounsell et al., 2010), which has a limiting magnitude of $m_{\rm SMEI} \sim 8$, preventing it from seeing such faint early time rises. It is only with the type of dedicated, deep, high cadence observations like those of MOA that we can observe such a rise—although it may be possible in the future with nightly cadence surveys like LSST (LSST Science Collaboration et al., 2009).

Catching such an early time rise is quite unique in studying novae, and deserves a thorough analysis that go beyond the scope of this work. We therefore defer the discussion of this early time rise to Wagner et al. (in prep).

#### 2.1.3.1 Onset of the Steep Optical Rise (Days 0 to +10)

The slow monotonic rise is followed by an extremely rapid increase in brightness; between day 0 and day +2 the brightness increased by $\sim 2.2$ mags day$^{-1}$. However, this is just an average, as no measurements were taken on day +1—as a result, there is an uncertainty of $\pm 2$ days on the start of the steep optical rise. Between days +2.8 and +3.3 the rate of increase dropped to $\approx 1.1$ mags day$^{-1}$, and then between days +5.6 and +6.8 the rate dropped to $\approx 0.3$ mags day$^{-1}$. This rate of increase persisted for the next two observation epochs (days +7.6 to +7.9 and +8.7 to +9.2), before becoming flat (i.e. $\sim 0$ mags day$^{-1}$) starting at the next observation epoch (days +12.9 to +13.2). From day 0 to day +12.9 the $I$ band flux increased by a total of $\approx 9.1$ magnitudes, with most of that rise occurring during the first $\approx 3$ days. This can be seen as phase B of Figure 2.1. Note that the large uncertainty in measurement on day 2 is the result of binning the measurements during the steep optical rise.

#### 2.1.3.2 Flattening of the Optical Light Curve (Days +10 to +45)

The enormous increase in the optical was followed by a period with a much smaller change in brightness, with $I$ changing by $\leq 1.5$ mags over the course of the next $\sim 30$ days. This flattening in the light curve is not unique to V1324 Sco; Strope et al. (2010) shows 15 examples of nova light curves with a similar flattening around peak, 10 of which also show a dust event. This can be seen as phase C of Figure 2.1.

It is during the flattening of the optical light curve that we see both the gamma-ray emission as well as the beginning of the initial radio bump (see section 4.2 for further details). It should be noted that, of the gamma-ray detected novae, at least two—V1369 Cen and V5668 Sgr—had similar flattening of the optical light curve near maximum (Cheung et al., 2016), though both exhibited large ($\Delta V > 1$ Mag) oscillations during their period of flattening.

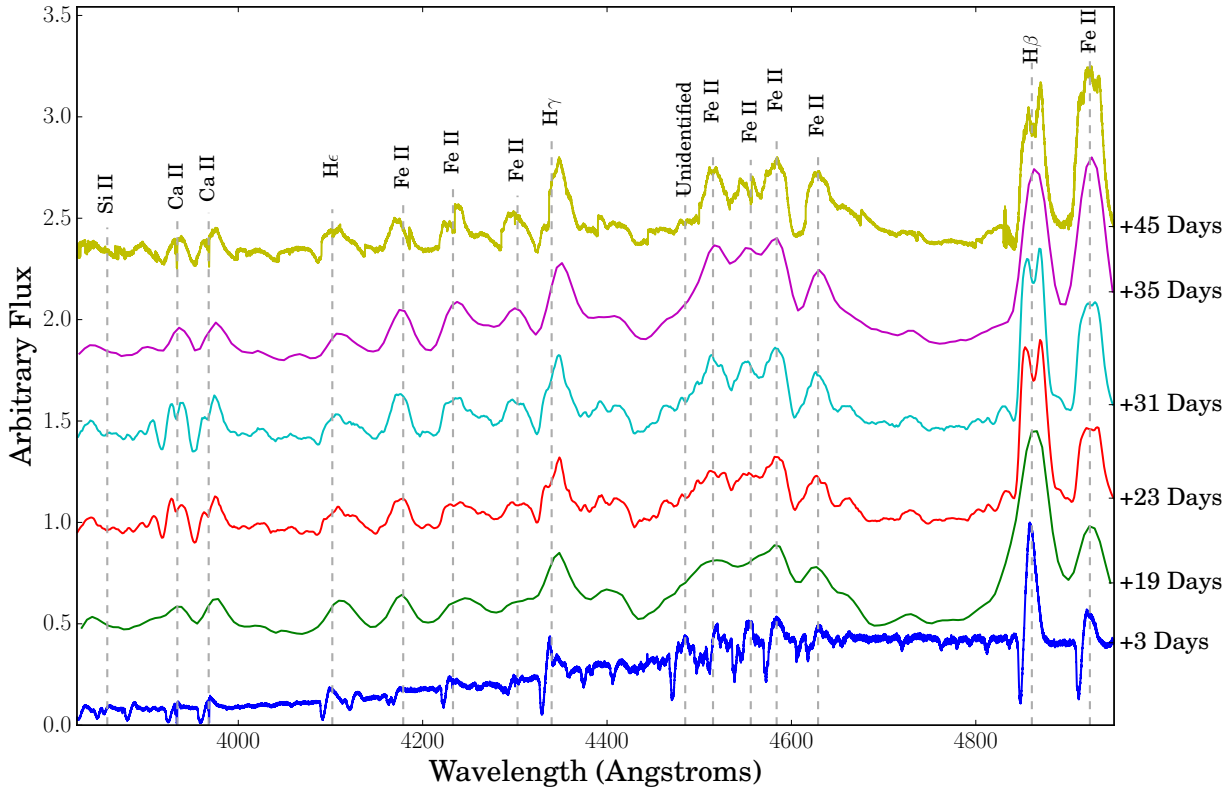


Figure 2.3 Evolution of the blue ($3900 - 4950$ Å) spectral region. All wavelengths have been corrected to be in the heliocentric frame. None of these spectra have been corrected for Telluric features.

#### 2.1.3.3 Dust Event (Days +45 to +157)

The flattening of the optical light curve was followed by another rapid change in brightness, this time downwards. There was a very clear, very large, decline in optical and near-IR flux that took place from day +46 to day +78, and a subsequent recovery from day +79 to day +157. Only the MOA $I$ band data had the cadence necessary to capture the minimum of the decrease. The $I$-band flux dropped by $\sim 8.5$ magnitudes in the span of $\sim 30$ days (Phase D in Figure 2.1). The observations in $BVR$ did not have the sensitivity to detect V1324 Sco at the bottom of the decline. Figure 2.2 shows that this decline in flux occurred all the way out to the near-IR (although the decrease was much less in the near-IR bands, i.e. only $\sim 3.9$ mags in $K$ band). This decline in flux that preferentially affects the shorter wavelength (bluer) light is the signature of a dust event.

A dust event occurs in a nova when the ejecta achieve conditions that are conducive to the condensation of dust—e.g. colder and shielded from ionizing radiation (Gallagher, 1977). The newly formed dust has a large optical depth; as a result a new, cooler, photosphere is created at the site of dust condensation. Dust events in novae are not a new phenomenon; McLaughlin (1936) first proposed dust condensation to explain

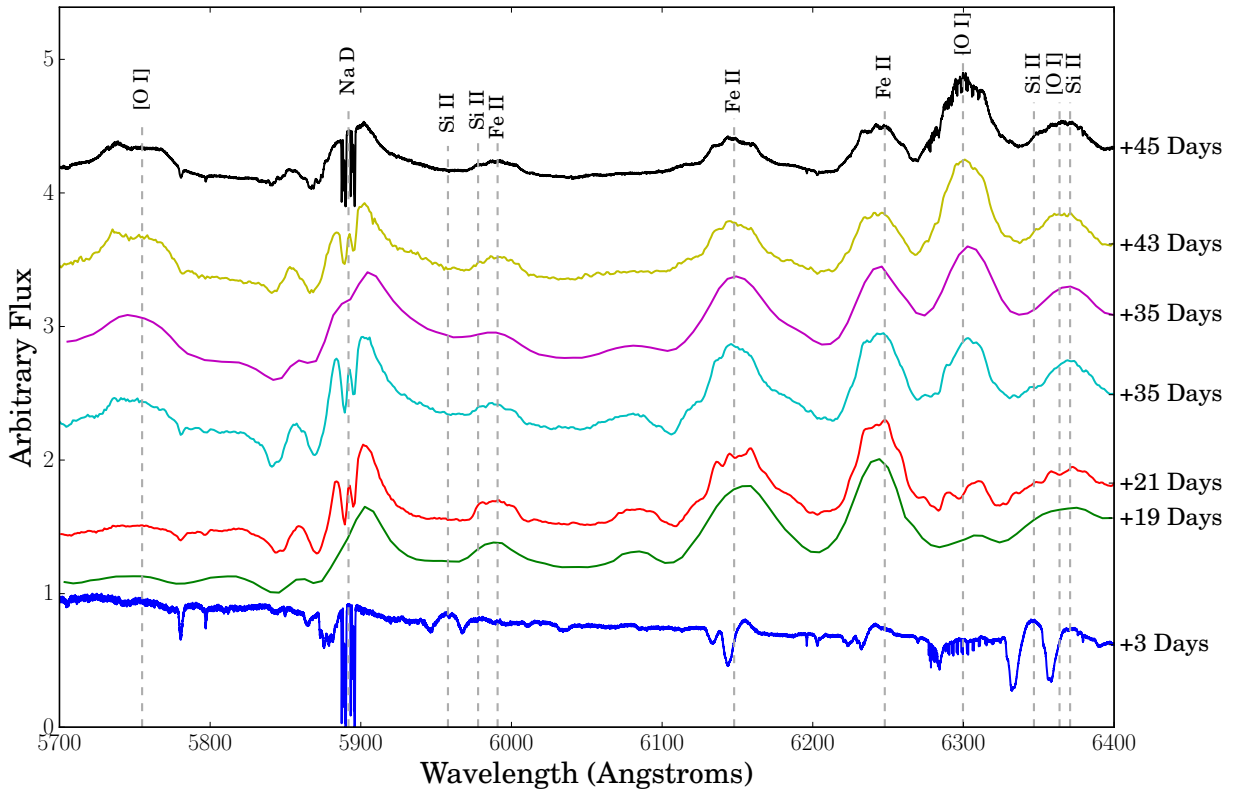


Figure 2.4 Evolution of the red ($5700 - 6400$ Å) spectral region. All wavelengths have been corrected to be in the heliocentric frame. None of these spectra have been corrected for Telluric features. The UVES spectrum taken on day +3 has contamination from Telluric absorption lines between 6280 Å and 6320 Å .

the significant decline in optical light seen in DQ Her.

The standard model of novae posits that the total luminosity of the ejecta remains constant, being powered by the luminosity of the still hot white dwarf at the center of the ejecta (Gallagher & Code, 1974; Bath & Shaviv, 1976), such that the fraction of the luminosity that is lost in the blue is compensated by increased luminosity in the red. This is only feasible if the cool dusty photosphere is significantly larger than the pre-dust photosphere (Gehrz et al., 1992). However, the details of this larger dust photosphere remain poorly understood. For a blackbody of constant luminosity $L \propto T_{\rm eff}^4 R^2 \rightarrow R \propto T_{\rm eff}^{-2}$, so even a modest decrease in temperature requires a significant increase in photosphere size to maintain constant luminosity.

In the case of V1324 Sco, the drop in flux all the way out to the near-IR suggests that the dust photosphere was very cold, and the change in temperature was significant. A rough calculation using the near-IR colors at the epoch closest to the $I$ band minimum suggest that the dust photosphere was $< 1000$ K. While these types of dust episodes are not unheard of— Strope et al. (2010) gives 16 examples of other such novae—there are only a few novae with dust dips showing comparably cool photospheres (e.g. QV Vul and V1280 Sco; Gehrz et al. 1992; Sakon et al. 2016).

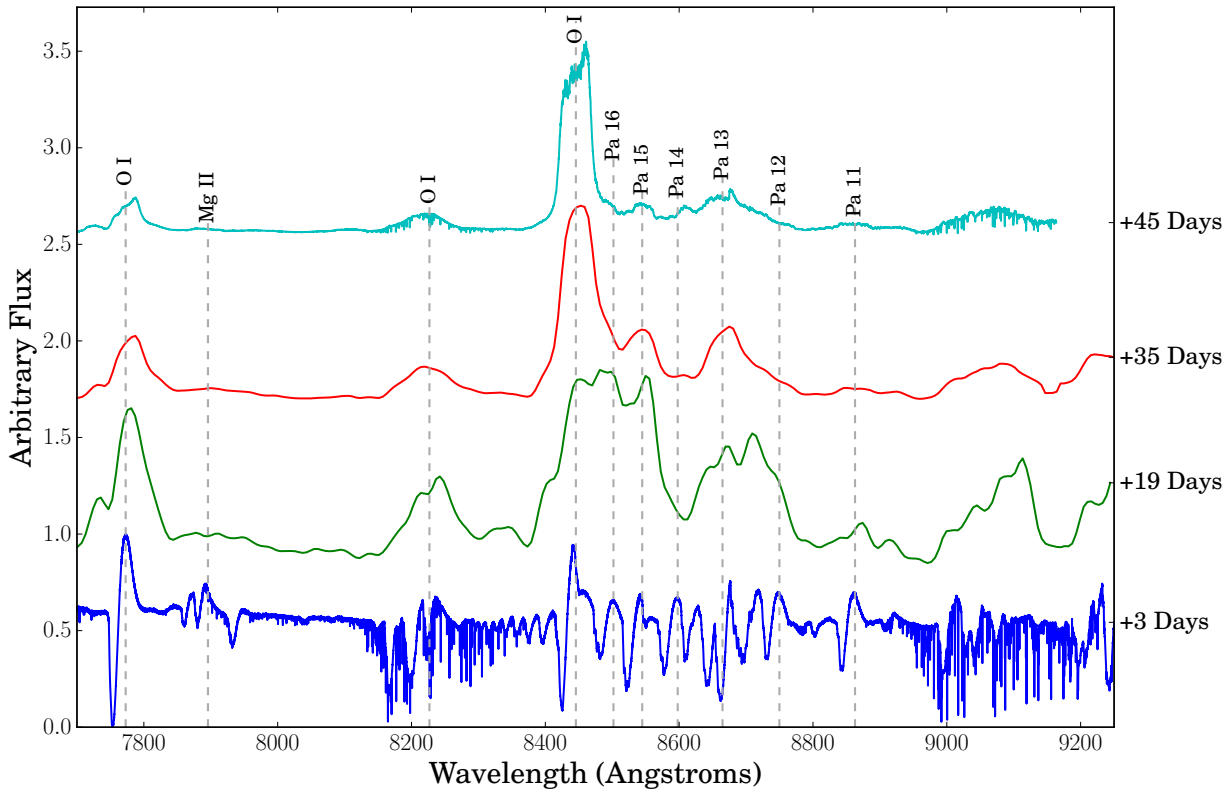


Figure 2.5 Evolution of the near-infrared (7700 − 9000 Å) spectral region. All wavelengths have been corrected to be in the heliocentric frame. None of these spectra have been corrected for Telluric features. The UVES spectrum taken on day +3 has prominent contamination from Telluric absorption lines between 8200 Å − 8300 Å and between 8900 Å − 9200 Å.

For further details we defer to the more thorough analysis of the dust event in V1324 Sco detailed Derdzinski et al. (2016).

#### 2.1.3.4 Power Law Decline (Days +157 to End of Monitoring)

Following the post-dust event rebound the evolution followed a power law decline, with $I \propto (t-t_0)^{0.2}$ (where $t_0$ is 2012 June 1). The index of the power law is positive because luminosity *decreases* when magnitudes *increase*. This decline continues until the final observation from April 2014, when it fell below the MOA detection threshold. In Figure 2.1, the power-law decline is phase E, between day +228 and +730.

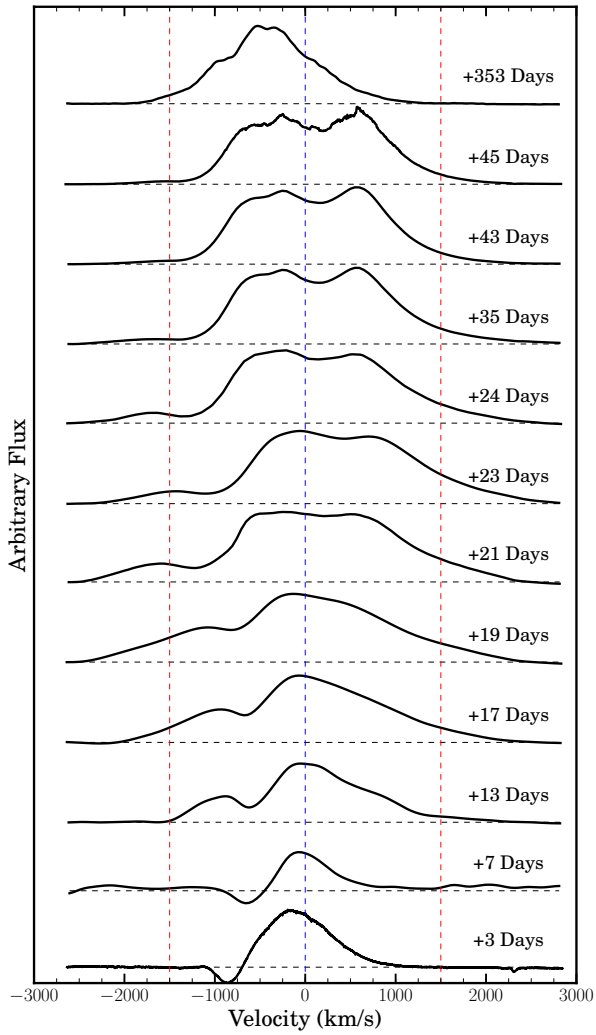


Figure 2.6 Evolution of the H$\alpha$ line as a function of time. We take day 0 to be June 1 2012. All velocities have had heliocentric corrections. The blue dashed line indicates $v = 0$ km s$^{-1}$, while the red dashed lines—used to help guide the eye—give $v = \pm 1500$ km s$^{-1}$. The $y-$axis is arbitrary flux; these relative flux values are not to scale. Note the expansion of the velocity profile starting sometime between day +7 and +13, and continuing until day $\sim +35$.

## 2.2 Optical Spectra

### 2.2.1 Observations and Reduction

We present the spectral observations in a manner similar to the work of Surina et al. (2014)—who carried out a multi-wavelength analysis of the 2011 outburst of T Pyx—by breaking up the analysis into sections based on the phases of the light curve. However, unlike Surina et al. (2014)—where the time frame is relative to the date of $V$ band maximum—all dates presented in this work are relative to the onset of the steep optical rise (taken to be 2012 June 1). All spectroscopic observations—including date, telescope, and observer—are

listed in Table 2.2. Note that all plots have been corrected to put them into the heliocentric frame.

Spectra were taken on 2012 June 4.1 UT (+3.1 days after main outburst) by Wagner et al. 2012 using the Ultraviolet and Visible Echelle Spectrograph (UVES) instrument on the VLT (Dekker et al., 2000). The spectra were taken as part of the follow-up conducted by the MOA group. Copies of the data were made publicly available on the ESO archive and were obtained by the authors.

Observations were made in dichroic mode, with the blue arm centered at 4370 Å (spanning $3600 - 4800$ Å) and the red arm centered at 7600 Å (covering $5600 - 9300$ Å), taken using two CCDs that have a chip gap between $7550 - 7650$Å. The slit width was $1.00''$ with an average seeing of $0.8''$, giving a resolution of $R \approx 40,000$ for the blue arm and $40,000 - 50,000$ for the red arm. Four 1800 second integrations were taken with $1 \times 1$ binning, with each integration having an average signal-to-noise of $S/N \approx 30$ per pixel for the blue arm and $S/N \approx 110 - 175$ per pixel for the red.

The reduction was undertaken using the standard ESO Reflex data reduction pipeline, which includes flatfield correction, bias subtraction, cosmic-ray removal, spectral extraction, and wavelength calibration using comparison spectra of a ThAr lamp (see Sacco et al. 2014 for details on the data reduction procedure). The four individual spectrum frames were combined using the IRAF routine *ndcombine*, giving a final $S/N$ per pixel of $\approx 60$ in the blue and $S/N$ per pixel of $\approx 220 - 350$ in the red.

Further observations were made on 2012 July 16.1 UT (+45.1 days after main outburst) using the MIKE instrument (Bernstein et al., 2003) on the 6.5 meter Magellan Clay telescope.

The MIKE instrument also has two arms, blue ($3350 - 5000$ Å) and red ($4900 - 9500$ Å). Two 300 second integrations were taken (total exposure of 600 seconds) with a $0.7''$ slit, giving a final resolution of $R \approx 40,000$ in the blue and $R \approx 30,000$ in the red. CCD binning was $2 \times 2$ for all integrations, giving an average $S/N$ per pixel of $\approx 30$ in the blue and $S/N$ per pixel of $\approx 170$ in the red.

The reduction for the MIKE spectra was done using the Carnegie Python tools (CarPy)[4], which provides a simple pipeline data reduction procedure. Milky flats, Quartz flats, Twilight flats, ThAr comparison lamps and bias frames were all taken during the observation run and utilized in the data reduction pipeline.

We note that the MIKE spectrum, having $\sim 0.5$ the S/N as the UVES spectrum in the red, was not used in any of our quantitative analysis. The MIKE spectrum was used instead as a qualitative check, to make sure that the spectral features seen in the UVES spectrum were not varying in time.

An optical spectrum was obtained on 2013 May 20.4 UT (day 353) using the 8.4 m Large Binocular Telescope (LBT) and Multi–Object Double Spectrograph (MODS1). Observing conditions were photometric but the seeing as measured from two independent sources ranged from $1.8-1.9''$ at the start of the observation. MODS1 utilized a $0.8''$ entrance slit (so there was some loss of light at the entrance slit) and G400L (blue

[4] `http://code.obs.carnegiescience.edu/mike`

channel; 3200–5800 Å) and G670L (red channel; 5800–10000 Å) gratings giving a final dispersion of 0.5″ per pixel. The combined spectrum covers the range 3420–10000 Å at a spectral resolution of 3.5 Å. The spectra of quartz–halogen and HgNeArXe lamps enabled the removal of pixel–to–pixel and other flatfield variations in response and provided wavelength calibration respectively. Spectra of the spectrophotometric standard star BD+33 2642 were obtained to measure the instrumental response function and provide flux calibration of the V1324 Sco spectra. The spectra were reduced with a set of custom routines to remove the bias from the detectors and provide flatfield correction and with IRAF (Version # 2.11) for spectral extraction and wavelength and flux calibration.

The SOAR Goodman data were taken using a 400 l/mm grating centered at 5000 Å, and were reduced using the standard procedure in IRAF with optimal extraction and wavelength calibration using FeAr arcs. In the case of the spectra taken by C. Buil and T. Bohlsen, both observers used a LISA spectrograph attached to commercially available telescopes of different sizes (0.28 meter Celestron for Buil; 0.22 meter Vixen VC200L for Bohlsen). More information about their observations can be found on their websites[5,6].

The details of the data reduction for the SMARTS RC Spectrograph data can be found in Walter et al. (2012).

### 2.2.2 Spectroscopic Evolution

#### 2.2.2.1 Onset of Steep Optical Rise (Days 0 to +10)

As discussed in Wagner et al. (2012), V1324 Sco appeared initially as a standard Fe II type nova Williams et al. (1991). As seen in Figure 2.6 there were strong P-Cygni absorption profiles starting at least as early as day +3. The H$\alpha$ emission component peaked at $\sim -180$ km s$^{-1}$ on day +3, and had a Gaussian FWHM of $\sim 800$ km s$^{-1}$. The H$\alpha$ P-Cygni absorption component had a FWHM of $\sim 200$ km s$^{-1}$. The entirety of H$\alpha$, including both the primary emission feature as well as the P-Cygni absorption, extended out to $\sim -1100$ km s$^{-1}$ in the blue, or $\sim 900$ km s$^{-1}$ away from line peak. We take the P-Cygni absorption profile to be coming from the fastest material, meaning that—at this early time—the expansion velocity was $\sim 900$ km s$^{-1}$.

As discussed in Schwarz et al. (2001), one would normally expect the bulk of the ejecta to be optically thick at these early times and, as a result, one would expect the spectral features to be absorption dominated. The presence of emission in the spectral features—which necessitates an optically thin region in the ejecta—suggests that the nova atmosphere is highly extended, even at this early stage.

The second most prominent features—aside from the Balmer lines—are the Fe II lines, all of which

[5] http://users.northnet.com.au/~bohlsen/Nova/
[6] http://www.astrosurf.com/buil/index.htm

showed P-Cygni profiles. This is evident in Figures 2.3 and 2.4, which show the time evolution of the blue ($3900-4950$ Å) and red ($5700-6400$ Å) spectral regions, respectively. In the UVES spectrum taken on day +3 there were Fe II lines at 4297 Å, 4556 Å, 4584 Å, 4629 Å, 4921 Å, and 6456 Å. There are further lines in the region between 4450 - 4540 Å. However, their morphology and velocity structure make them difficult to identify. There is also a feature that could not be identified using the table provided in Williams (2012) that shows a P-Cygni profile and peaks around 4485 Å. It is possible that this is a blend of an Mg II feature at 4481 Å and Fe II feature at 4491 Å.

During this early time we see transitory Si II absorption features at 3858 Å, 5958/78 Å and 6347/71 Å. While present on day +3 all evidence of them disappears by day +22, when the next medium-resolution spectrum was taken. These are the highest excitation lines we see at this early time—having an ionization potential of 16.3 eV—so we attribute the appearance of these absorption features as being evidence of a slightly harder ionizing radiation field at early times, as compared to late times (Hillman et al., 2014).

#### 2.2.2.2 Flattening of the Optical Light Curve (Days +10 to +45)

This period is demarcated by two qualitative changes: an increase in the H$\alpha$ linewidth (see Figure 2.6), as well as the onset of the optical decline (i.e. post-maximum stage). This type of increase in the linewidths has been seen before (for some more recent examples see, e.g. Schwarz et al. 2001; Surina et al. 2014). In previous works, this increase in linewidth was attributed to a gradually accelerating radiatively driven wind. We discuss this further in Section 4.2.1.

#### 2.2.2.3 Nebular Phase

Within just a few days of the Magellan MIKE spectrum—taken on day +45—V1324 Sco underwent a massive dust dip, dropping by $> 8$ mags in $I$ band in $\sim 30$ days, ultimately bottoming out at $I \simeq 17.7$ (see Section 2.1.3.3 for further details). It was at $I > 16.0$ magnitude for the next $\sim 50$ days. Although it did eventually rebound out of the dust dip, there was only a brief window of $\sim< 25$ days before it went into solar conjunction. As a result our spectroscopic coverage did not pick back up until 20 May 2013—355 days after eruption—well into the nebular phase. All of our analysis and line identification is done using the LBT spectrum taken on day +355, as it had better resolution and significantly better S/N.

As seen in Figure 2.7 the strongest lines in the nebular phase are the [O III] lines at 5007 and 4959 Å, followed by H$\alpha$ and [Fe VII] at 6084 Å. A list of all of the observed nebular lines is given in Table 2.3. Most of the lines were matched using the table provided in the appendix of Williams (2012)

There are several lines that seem to have a match but, assuming they are matched correctly, have a peak velocity that is significantly different than the other lines. Such lines include He II at 8237 Å, which would

have a peak velocity of $\sim 0$ km s$^{-1}$, C I at 8335 Å, which would have a peak velocity of +100 km s$^{-1}$, and [S III] at 9531 Å, which would also have a peak velocity of +100 km s$^{-1}$ . This is in contrast to most of the other lines, which have peak velocities between $-200$ to $-350$ km s$^{-1}$.

Note that a full fitting procedure to the nebular data using a photoionization code such as CLOUDY (Ferland et al., 1998) was not attempted due to the lack of UV spectral data, as the diagnostic power is severely diminished without UV data, which contains a large fraction of the emission lines commonly studied in novae.

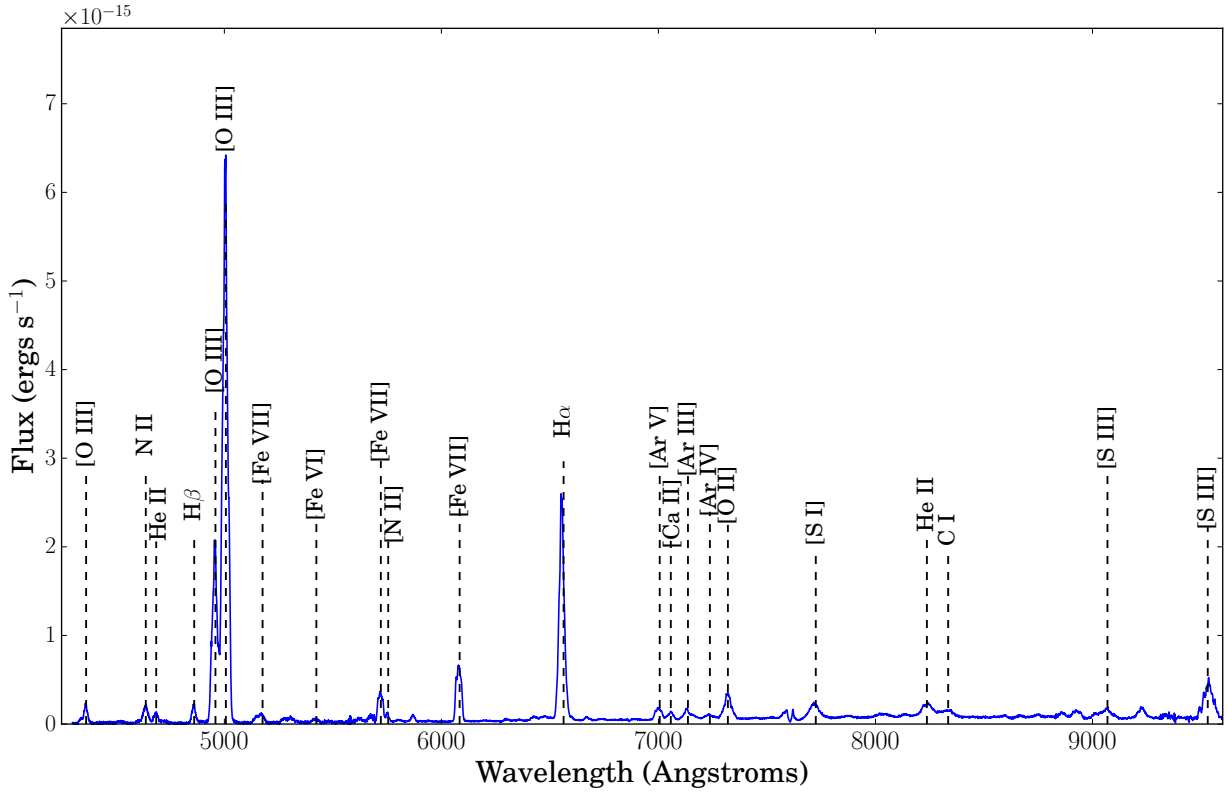


Figure 2.7 Spectrum for V1324 Sco during the nebular phase taken on day +353.

## 2.3 X-ray

Multiple X-ray observations were made using the *Swift* X-Ray Telescope (XRT), all of them yielding non-detections. That is, we did not detect thermal X-rays from the shocked plasma, and we did not detect non-thermal (hard) X-rays from the population of accelerated particles. This is especially noteworthy given that the extremely high gamma-ray luminosity should imply a relatively strong shock, which would generate a significant amount of hard X-rays (Mukai & Ishida, 2001). As discussed in Vurm & Metzger (2016),

Table 2.3. Nebular Phase Spectral Lines

| Feature | Wavelength (Å) |
|---|---|
| [O III] | 4363 |
| N II | 4638 |
| He II | 4686 |
| H$\beta$ | 4861 |
| [O III] | 4959 |
| [O III] | 5007 |
| [Fe VII] | 5176 |
| [Fe VI] | 5424 (low S/N) |
| [Fe VII] | 5721 |
| [N II] | 5755 |
| [Fe VII] | 6084 |
| [Ar V] | 7006 |
| H$\alpha$ | 6563 |
| [Ar V] | 7006 |
| [Ca II] | 7057 |
| [Ar III] | 7136 |
| [Ar IV] | 7237 |
| [O II] | 7320/7330 (Lines blended) |
| [S I] | 7725 |
| He II | 8237 |
| C I | 8335 |
| [S III] | 9069 |
| [S III] | 9531 |

this apparent contradiction can be explained by either the presence of high densities behind the radiative shock—due to Coulomb collisions sapping energy from what would otherwise be X-ray emitting particles—or by bound-free (photoelectric) absorption or inelastic Compton downscattering if there is a large column of material ($\gtrsim 10^{25}$ cm$^{-2}$) ahead of the shock. In Section 3.5, we use oxygen line ratios to show such high column densities are plausible.

Note that, along with the peculiar lack of hard X-rays from non-thermal particle acceleration, there was also a lack of soft X-rays, which are usually seen at later times (see, e.g., Schwarz et al. 2011). However, V1324 Sco was both distant ($\geq 6.5$ kpc Finzell et al. 2015) and had a large absorbing column density. The only other nova given in Schwarz et al. (2011) with both of these characteristics is V1663 Aql, a nova that was also never detected as a super soft source.

We present the X-ray limits obtained from the *Swift* observations in Table 2.4. The quoted limits are the $3\sigma$ upper limits, derived using the Bayesian upper limit method outlined in Kraft et al. (1991). The count rates were converted into luminosities assuming emission from a thermal plasma with characteristic temperature 1 keV and a distance of 6.5 kpc, which is the lower limit derived in Finzell et al. (2015). These limits are for X-ray luminosities in the range $0.3 - 10$ keV, assuming a distance of 6.5 kpc, and modeling the X-ray emission as a thermal plasma with a temperature of 1 keV and solar metallicity. The luminosity limits only correct for absorption by the ISM, assuming a column density of $8 \times 10^{21}$ cm$^{-2}$. The column density was derived using the reddening values of Finzell et al. (2015) and the relationship of Güver & Özel (2009). These limits were used in the analysis of Metzger et al. (2014) and we provide the numbers here for

Table 2.4. X-ray Upper Limits from *Swift* XRT

| Date (UT) | $t - t_0$ (Days) | Count Rate[a] ($s^{-1}$) | Luminosity[ab] (ergs $s^{-1}$ ) |
|---|---|---|---|
| 2012 Jun 22 | +21 | 0.0031 | 1.67E+33 |
| 2012 Jun 27 | +26 | 0.0054 | 2.91E+33 |
| 2012 Jun 28 | +27 | 0.0151 | 8.11E+33 |
| 2012 Jul 4 | +33 | 0.0038 | 2.04E+33 |
| 2012 Jul 10 | +39 | 0.0120 | 6.44E+33 |
| 2012 Jul 13 | +42 | 0.0055 | 2.96E+33 |
| 2012 Aug 14 | +74 | 0.0031 | 1.66E+33 |
| 2012 Oct 16 | +137 | 0.0023 | 1.23E+33 |
| 2013 May 22 | +355 | 0.0030 | 1.61E+33 |
| 2013 Nov 3 | +520 | 0.0037 | 1.99E+33 |

[a] $3\sigma$ Upper limits

[b] Note that this is based on a distance lower bound of 6.5 kpc, modeling the X-ray emission as a thermal plasma with a temperature of 1 keV, with solar metallicity. The luminosity is for an energy range of $0.3 - 10$ keV.

completeness.

## 2.4 Radio Data

Radio emission from novae is a crucial tool in our analysis, as the opacity at radio frequencies is directly proportional to the emission measure—defined for some line of sight $z$ as $EM_z = \int n_e^2 dz$—of the emitting material. We can map out the density profile of the ejecta by watching the evolution of the radio emission (Bode & Evans, 2008). The early time radio can also show unexpected behavior that can be used to constrain other parameters of the nova event.

### 2.4.1 Observations and Reduction

We obtained sensitive radio observations of V1324 Sco between 2012 June 26 and 2014 December 19 with the Karl G. Jansky Very Large Array (VLA) through programs S4322, 12A-483, 12B-375, 13A-461, 13B-057, and S61420. Over the course of the nova, the VLA was operated in all configurations, and data were obtained in the C (4–8 GHz), Ku (12–18 GHz), and Ka (26.5–40 GHz) bands, resulting in coverage from 4–37 GHz. Observations were acquired with 2 GHz of bandwidth and 8-bit samplers, split between two independently tunable 1-GHz-wide basebands. The details of our observations are given in Table 2.5.

At the lower frequencies (C band), the source J1751-2524 was used as the complex gain calibrator, while J1744-3116 was used for gain calibration at the higher frequencies (Ku and Ka bands). The absolute flux density scale and bandpass were calibrated during each run with either 3C48 or 3C286. Referenced pointing scans were used at Ku and Ka bands to ensure accurate pointing; pointing solutions were obtained on both

the flux calibrator and gain calibrator, and the pointing solution from the gain calibrator was subsequently applied to our observations of V1324 Sco. Fast switching was used for high-frequency calibration, with a cycle time of ∼2 minutes. Data reduction was carried out using standard routines in AIPS and CASA. Each receiver band was edited and calibrated independently. The calibrated data were split into their two basebands and imaged, thereby providing two frequency points.

An observation in A configuration (the most extended VLA configuration) from 2012 Dec 16 suffered severe phase decorrelation at higher frequencies. Despite efforts to self calibrate, we could not reliably recover the source and we therefore do not include these measurements here.

In each image, the flux density of V1324 Sco was measured by fitting a Gaussian to the imaged source with the tasks `JMFIT` in AIPS and `gaussfit` in CASA. We record the integrated flux density of the Gaussian; in most cases, there was sufficient signal on V1324 Sco to allow the width of the Gaussian to vary slightly, but in cases of low signal-to-noise ratio, the width of the Gaussian was kept fixed at the dimensions of the synthesized beam. Errors were estimated by the Gaussian fitter, and added in quadrature with estimated calibration errors of 5% at lower frequencies (<10 GHz) and 10% at higher frequencies (>10 GHz). All resulting flux densities and uncertainties are presented in Table 2.5. V1324 Sco was unresolved in all observations.

### 2.4.2 Timeline of Radio Light Curve

Here we discuss the different phases of the radio light curve evolution. The radio emission is shown in Figure 2.8 (radio light curve) and Figure 2.9 (radio spectra).

#### 2.4.2.1 Initial Radio Bump (Days +25 to +136)

V1324 Sco was detected during the first radio observation (day +25), coincident with the end of the gamma-ray emission and one day before the second X-ray observation. In subsequent radio observations the light curve showed an initial bump, peaking on day +72. The emission after the initial bump—which we refer to as the second bump—was seen 30 to 50 days later (days +102 and +152, respectively; see Figure 2.8).

The radio spectrum during the initial bump started out flat, with $\alpha = -0.3 \pm 0.7$ on day +25 (where $\alpha$ is defined such that $S_\nu \propto \nu^\alpha$). It then transitioned to $\alpha = 2.0 \pm 0.3$ on day +65, which is consistent with optically thick thermal emission. The spectrum then flattened out again ($\alpha = 0.6 \pm 0.1$ on day +72). Note that the first two epochs were only based on two frequencies (4.5 GHz and 7.8 GHz) while the epoch on day +72 included higher frequency observations (27.5 GHz and 36.5 GHz). As a result, the early time fits should be interpreted with some caution.

A full discussion of the implications for this initial radio bump is given in Section 4.2.2.

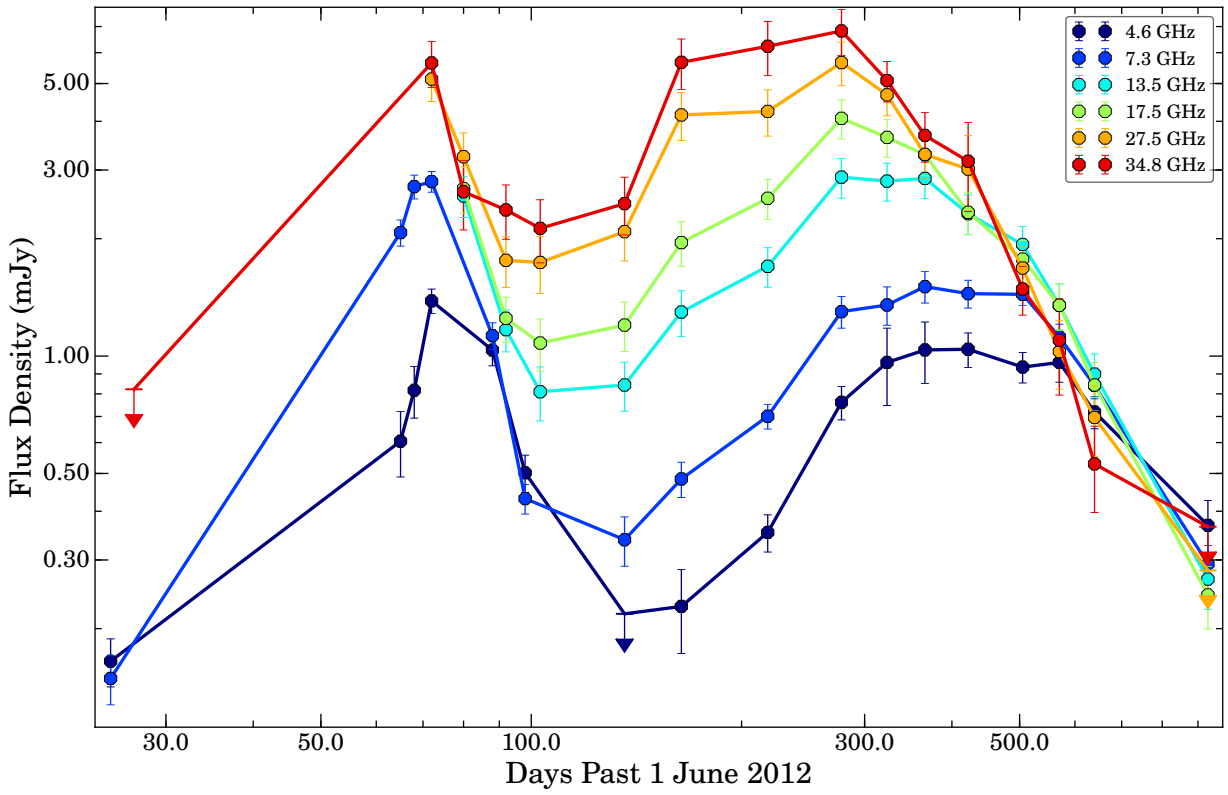


Figure 2.8 Radio light curve for V1324 Sco, spanning day +22 to day +930 (using June 1 2012 as day 0). Note the initial radio bump seen between day +25 to day +136.

#### 2.4.2.2 Second Radio Bump (Days +137 to +900)

After this initial radio bump, a secondary radio bump occurred, starting sometime between September 15 2012 and October 15 2012 (+106 and +136 days after 2012 June 1), starting with high frequencies and progressing to lower frequencies. During this secondary radio bump, V1324 Sco peaked at $\sim$ 6.23 mJy at high frequencies (36 GHz) between days +218 and +323, and peaked at $\sim$ 1.0 mJy for low frequencies (4.5 GHz) between days +366 and +505. In terms of the evolution of the second radio bump, V1324 Sco was relatively normal compared to the other novae that have been studied in the radio (e.g. Seaquist & Palimaka 1977; Hjellming et al. 1979; Chomiuk et al. 2012; Nelson et al. 2014; Weston et al. 2016a). Further analysis of the second radio bump is presented in Section 3.4.

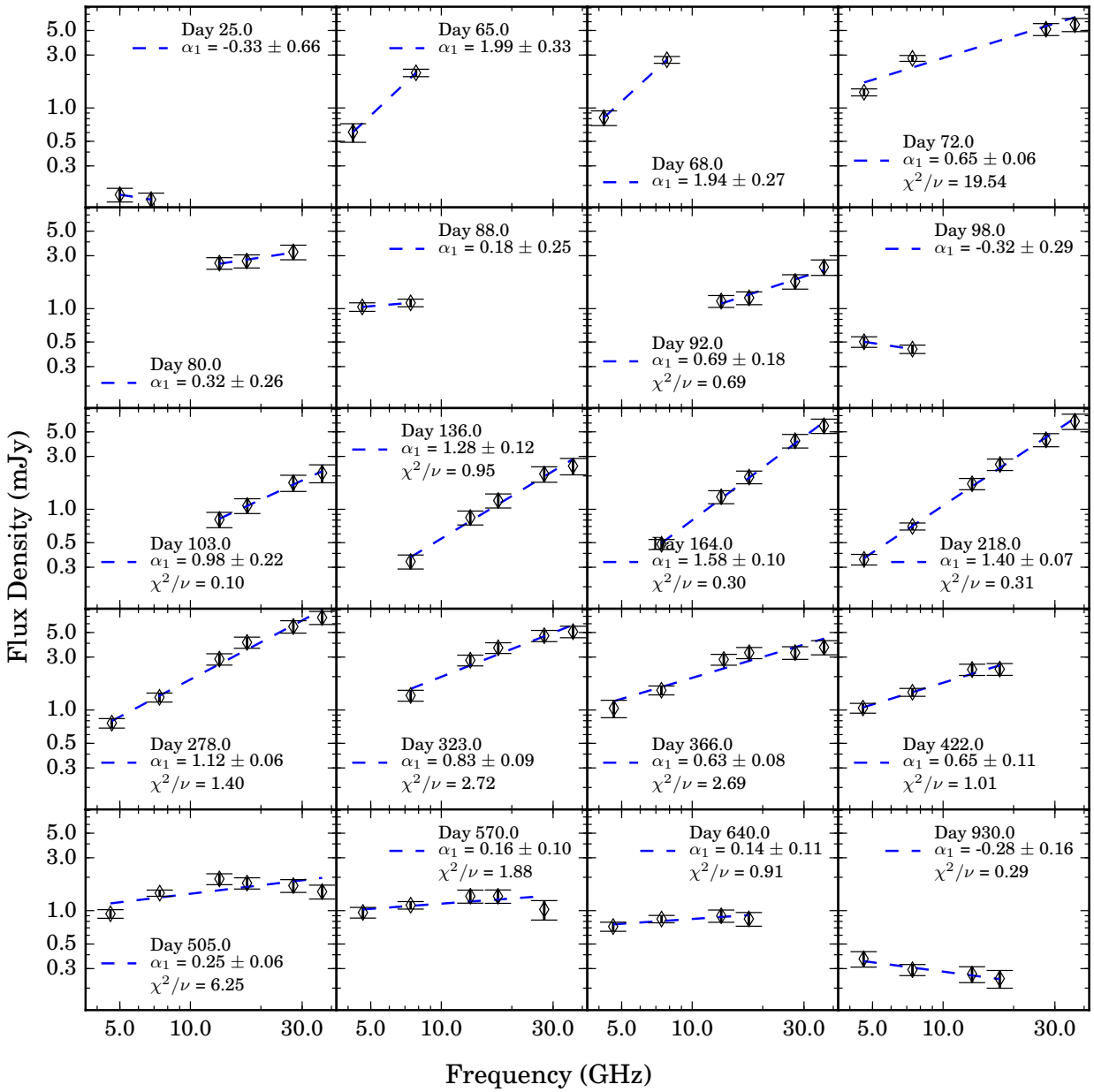


Figure 2.9 Radio spectra for V1324 Sco. At every epoch with measurements at 3 or more frequencies we fit either a power-law or double power-law to the flux values. The best fit solution was determined by the reduced chi-squared value closest to 1.

Table 2.5. VLA Observations of V1324 Sco

| Julian (245000+) | Date (UT) | $t - t_0$ | Config. | 4.5 GHz Flux [a,b] (mJy) | 7.8 GHz Flux (mJy) | 13.3 GHz Flux (mJy) | 17.4 GHz Flux (mJy) | 27.5 GHz Flux (mJy) | 36.5 GHz Flux (mJy) |
|---|---|---|---|---|---|---|---|---|---|
| 6104.3 | 6/26/2012 | 25.0 | B | 0.165 ± 0.023 | 0.149 ± 0.021 | – | – | – | – |
| 6106.1 | 6/28/2012 | 27.0 | B | – | – | – | – | – | <0.822 |
| 6144.1 | 8/5/2012 | 65.0 | B | 0.605 ± 0.115 | 2.074 ± 0.160 | – | – | – | – |
| 6147.1 | 8/8/2012 | 68.0 | B | 0.817 ± 0.124 | 2.720 ± 0.191 | – | – | – | – |
| 6151.2 | 8/12/2012 | 72.0 | B | 1.385 ± 0.100 | 2.803 ± 0.171 | – | – | 5.133 ± 0.636 | 5.647 ± 0.766 |
| 6159.2 | 8/20/2012 | 80.0 | B | – | – | 2.574 ± 0.307 | 2.690 ± 0.364 | 3.246 ± 0.489 | 2.639 ± 0.533 |
| 6167.0 | 8/28/2012 | 88.0 | B | 1.036 ± 0.092 | 1.128 ± 0.089 | – | – | – | – |
| 6171.1 | 9/1/2012 | 92.0 | B | – | – | 1.169 ± 0.144 | 1.250 ± 0.165 | 1.760 ± 0.261 | 2.370 ± 0.377 |
| 6177.9 | 9/7/2012 | 98.0 | BnA | 0.502 ± 0.055 | 0.431 ± 0.038 | – | – | – | – |
| 6182.1 | 9/12/2012 | 103.0 | BnA | – | – | 0.810 ± 0.128 | 1.080 ± 0.165 | 1.738 ± 0.290 | 2.126 ± 0.392 |
| 6215.0 | 10/15/2012 | 136.0 | A | <0.218 | 0.338 ± 0.049 | 0.843 ± 0.121 | 1.201 ± 0.174 | 2.085 ± 0.332 | 2.460 ± 0.415 |
| 6243.8 | 11/12/2012 | 164.0 | A | 0.228 ± 0.055 | 0.484 ± 0.050 | 1.297 ± 0.174 | 1.955 ± 0.256 | 4.153 ± 0.582 | 5.667 ± 0.838 |
| 6297.6 | 1/5/2013 | 218.0 | A | 0.353 ± 0.039 | 0.701 ± 0.051 | 1.699 ± 0.198 | 2.539 ± 0.301 | 4.240 ± 0.574 | 6.230 ± 0.983 |
| 6357.5 | 3/6/2013 | 278.0 | D | 0.761 ± 0.075 | 1.300 ± 0.121 | 2.877 ± 0.337 | 4.071 ± 0.469 | 5.660 ± 0.725 | 6.821 ± 0.917 |
| 6402.3 | 4/20/2013 | 323.0 | D | 0.963 ± 0.216 | 1.352 ± 0.153 | 2.810 ± 0.313 | 3.637 ± 0.403 | 4.677 ± 0.543 | 5.089 ± 0.605 |
| 6445.4 | 6/2/2013 | 366.0 | DnC | 1.037 ± 0.186 | 1.507 ± 0.139 | 2.855 ± 0.322 | 3.283 ± 0.379 | 3.290 ± 0.429 | 3.680 ± 0.538 |
| 6501.3 | 7/28/2013 | 422.0 | C | 1.041 ± 0.105 | 1.446 ± 0.118 | 2.318 ± 0.270 | 2.337 ± 0.286 | 3.017 ± 0.659 | 3.160 ± 0.811 |
| 6584.0 | 10/19/2013 | 505.0 | B | 0.937 ± 0.084 | 1.440 ± 0.093 | 1.933 ± 0.218 | 1.773 ± 0.206 | 1.682 ± 0.222 | 1.486 ± 0.213 |
| 6649.7 | 12/23/2013 | 570.0 | B | 0.963 ± 0.106 | 1.120 ± 0.087 | 1.350 ± 0.182 | 1.350 ± 0.186 | 1.027 ± 0.205 | 1.098 ± 0.304 |
| 6719.5 | 3/3/2014 | 640.0 | A | 0.719 ± 0.068 | 0.841 ± 0.064 | 0.899 ± 0.114 | 0.843 ± 0.119 | 0.696 ± 0.143 | 0.529 ± 0.132 |
| 7009.8 | 12/18/2014 | 930.0 | C | 0.368 ± 0.058 | 0.293 ± 0.034 | 0.268 ± 0.044 | 0.244 ± 0.044 | <0.282 | <0.365 |

Note. — Taking $t_0$ to be 2012 June 1

[a]Detections are defined as flux $> 5\sigma$. Non-detections are given as the $5\sigma$ upper limits.

[b]If no observations were taken for a given frequency it is denoted by –.

# 3 Analysis

## 3.1 A Brief Interlude on the Importance of Determining Physical Properties of Novae

In this chapter we use different techniques to determine physical properties of the classical nova V1324 Sco. Translating observables to physical quantities is an extremely important task, as it allows us to model novae.

Before we begin dissecting the data to determine physical parameters, we must first determine the reddening. As the light passes through the interstellar medium on its way to the observer some amount of the light will be blocked by the material it is passing through. Further, blue light will be preferentially blocked compared to red light. This is called interstellar reddening, and the reddening value is a measure of how much more blue light has been blocked compared to the red light. Correcting for interstellar reddening allows us to determine the true—i.e. if it were observed in a vacuum—amount of flux emitted by the object in question. We also use the reddening value as a means to set a lower-limit on the distance to V1324 Sco. Once flux is corrected for reddening we can determine other physical properties, such as the ejecta mass.

## 3.2 Determining Distance

### 3.2.1 Reddening

#### 3.2.1.1 Reddening Measurement from DIBs

We use the Equivalent Width (EW) of Diffuse Interstellar Bands (DIBs) to measure the reddening, a method that has already been used in the context of novae (see e.g., Shore et al. 2011; Munari et al. 2012). Friedman et al. (2011) found an empirical relationship between the EW of eight strong optical DIBs and the reddening along a given sight line. In V1324 Sco, one of these eight DIB features (5487.7 Å) had very low S/N (in

Table 3.1. Best Fit Reddening Values For DIBs

| DIB $\lambda$ (Å) | EW (mÅ) | E($B-V$) |
|---|---|---|
| 5705.1 | 99 ± 9 | $1.01 \pm 0.11$ |
| 5780.5 | 581 ± 40 | $1.14 \pm 0.08$ |
| 5797.1 | 155 ± 16 | $0.86 \pm 0.09$ |
| 6196.0 | 68 ± 2 | $1.39 \pm 0.04$ |
| 6613.6 | 200 ± 8 | $0.94 \pm 0.04$ |

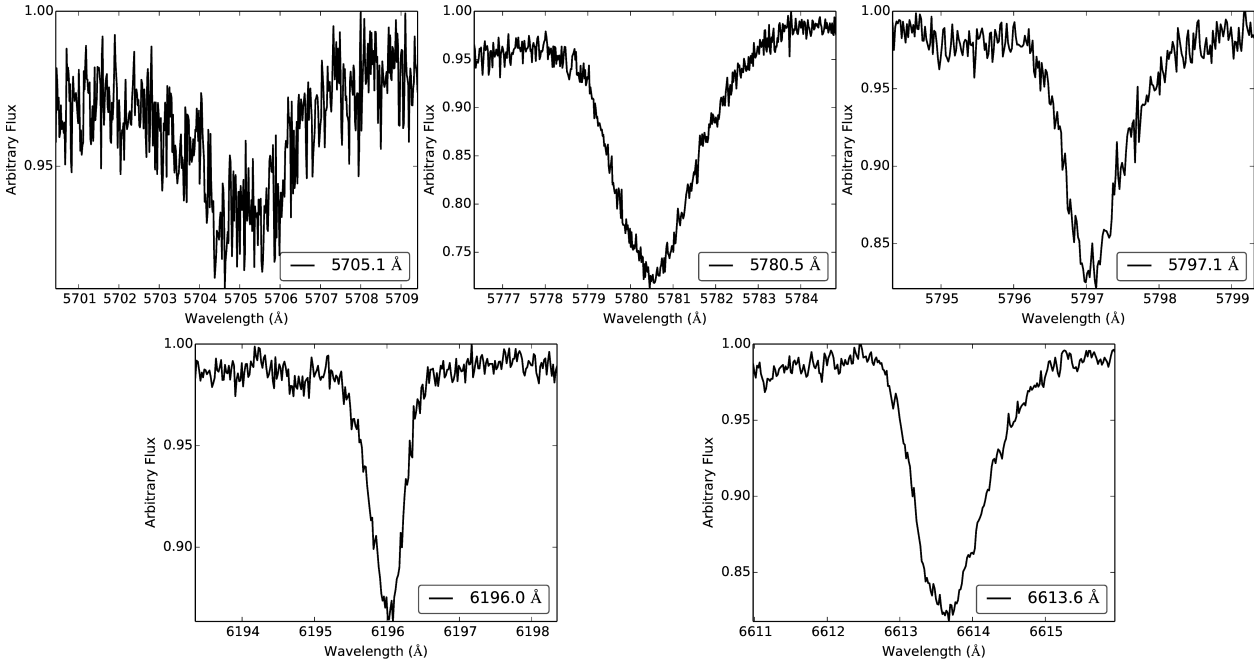


Figure 3.1 Five DIBs that were used to determine reddening. The largest contributor of uncertainty in the EW of the DIB features was determination of the continuum flux. This is why, in spite of the poor $S/N$, the 5705.1 Å feature has a comparable uncertainty to the other features.

both VLT and MIKE spectra) and was not used, and two features (6204.5 Å and 6283.8 Å) were discarded due to overlapping telluric features (spectral features coming from Earth's atmosphere, not the astrophysical object). The remaining five DIBs were used to find a value for $E(B-V)$ (a logarithmic ratio of the extincted red light over extincted blue light, hereafter referred to as the reddening). All of the EW values were measured using the VLT spectrum (see Figure 3.1) as it had a much higher $S/N$ in the red compared to the MIKE spectrum. The specific DIB EW values are given in Table 3.1, and the derived $E(B-V)$ as a function of wavelength is plotted in Figure 3.2. The IRAF tool *splot* to measure EW values through direct integration. By iteratively varying both the bounds of integrations and the continuum flux level we determined a spread of potential EW values for each line; from this spread we determined the uncertainty in the EW values. The primary uncertainty in determining the EW values was setting the continuum flux level. From our derived values for the reddening we took an error weighted average and found $E(B-V) = 1.07$ with a $1\sigma$ uncertainty on the error weighted average of $\pm 0.20$. The uncertainty for the individual $E(B-V)$ values derived for each DIB included both the uncertainty in the fit parameters from Friedman et al. (2011) as well as the standard deviation in measured EW values. The final uncertainty in the error weighted average was dominated by the spread in derived $E(B-V)$ values for different DIB features.

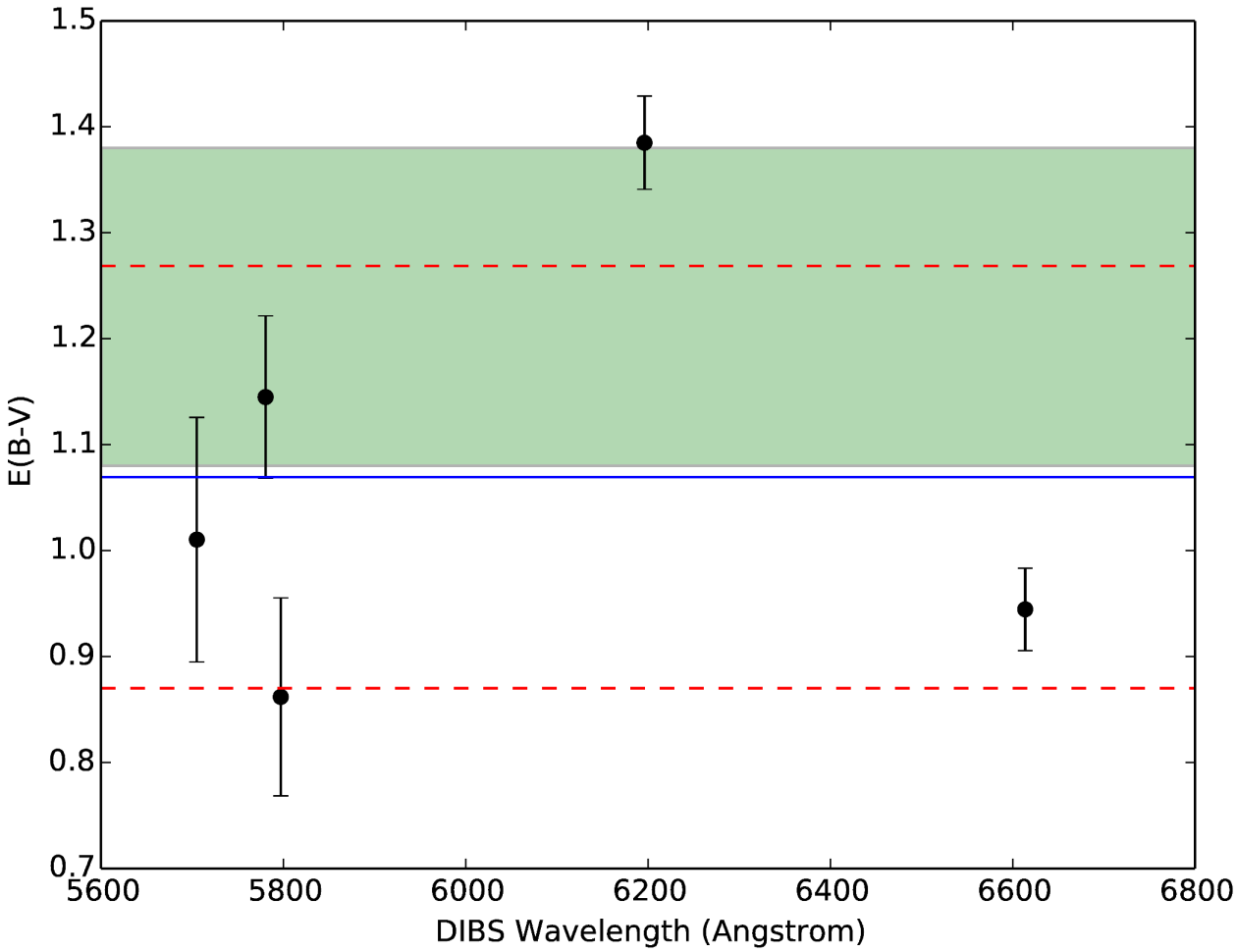


Figure 3.2 The best fit $E(B-V)$ values for all five DIBs that were analyzed (see Table 3.1 for the specific values). The reddening value for each DIB was determined using the best-fit values of Friedman et al. (2011). The average reddening value is $E(B-V) = 1.07$ (the solid horizontal blue line) with an uncertainty of $\pm 0.20$ (the dashed horizontal red lines). The green band corresponds to the reddening value, $E(B-V) = 1.23 \pm 0.15$, derived using the EW of Na and K absorption features. The width of the band corresponds to the uncertainty in the derived value.

#### 3.2.1.2 Reddening Measurement from Na and K Absorption Features

We used a second, independent, method to determine the reddening. This method utilized the empirical relationship found by Munari & Zwitter (1997), which relates reddening to the total equivalent width of the Na I D absorption lines (at 5889.9 Å and 5895.9Å) and K I absorption line (at 7698.9 Å). The material along the line of sight to an object will have some characteristic features due to interstellar absorption, and Munari & Zwitter (1997) calibrated two of these features to determine the amount of reddening each feature contributes. The sum of reddening from individual absorbing features gives the total reddening.

Munari & Zwitter (1997) found that the Na I D features are ideal for tracing reddening at low column densities, but saturates at high column densities. In these instances the K I feature, which does not saturate

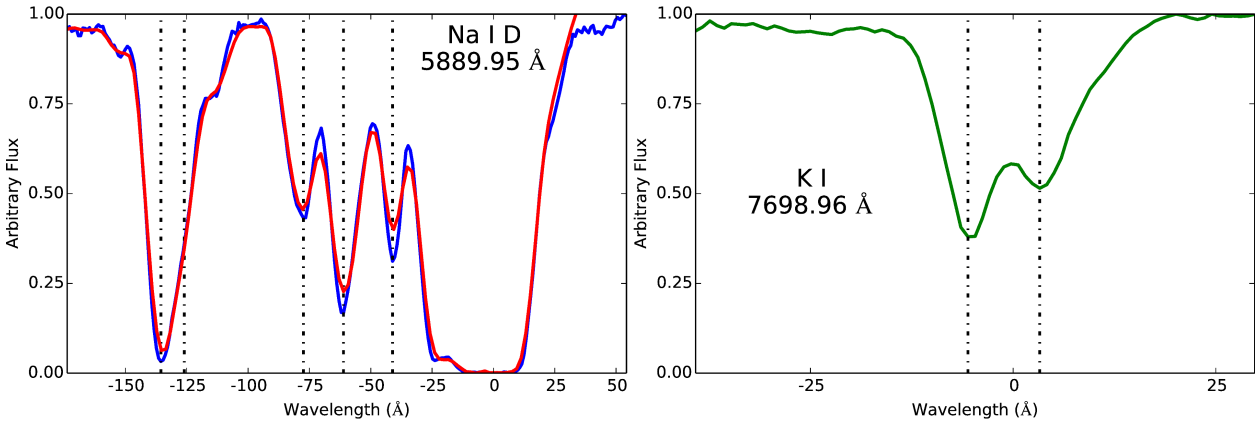


Figure 3.3 Sodium D (5889.95 Å) and potassium (7698.96 Å) interstellar absorption features that were used to derive a value for the reddening. The specific absorption components from Table 3.2 are marked as black dashed lines. We plot both the UVES and MIKE spectra for the sodium to show that these features are unchanging in time, meaning they are interstellar and not associated with the nova. Note that we only use the potassium absorption feature to calculate reddening when the sodium feature is saturated, which is why we are only showing the potassium in the region where the sodium is saturated.

as easily, can be used to determine the reddening. In our case, we only needed to utilize the K I for the two Na I D features that were saturated (at $-7$ and $+3$ km/s).

To ensure that the absorption features were the result of interstellar clouds, and not the nova itself, we compared the UVES and MIKE spectra. If the features were from the nova, we would expect them to change over time. As can be seen in the Na I D plot in Figure 3.3, which shows both the UVES and MIKE spectra, the features remained constant. We did not plot the MIKE spectra for the K I features, as the S/N was very low.

Just as in the case of the DIBs features, only the UVES spectrum was used to measure the EW values as it had a higher S/N as compared to the MIKE spectrum. To avoid potential contamination of the lines with telluric features we used an archived telluric divider to remove telluric features from the UVES spectrum. Values for the EW were derived by fitting one or more Gaussian profiles to the individual spectral features. The EW, derived reddening, and velocity of the absorption features that we used to find the total reddening are given in Table 3.2 and Figure 3.3. Although the uncertainty resulting from sum of the measured quantities is $\pm 0.09$, the intrinsic scatter that Munari & Zwitter (1997) found in their calibration was 0.15 for large reddening values ($E(B-V) \geq 0.4$). As a result, we take 0.15 to be the uncertainty.

The reddening value found using this technique, $E(B-V) = 1.23 \pm 0.15$, is consistent (within margin of uncertainty) with the reddening derived using the DIB features.

We combine these two independent reddening measurements by taking an error weighted average of the two, which yields our final reddening value of $E(B-V) = 1.16 \pm 0.12$.

Table 3.2. Reddening Values from Na I D & K I Absorption Lines

| Absorption Wavelength (Å) | EW (mÅ) | E($B-V$) | LSR Radial Velocity (km s$^{-1}$) |
|---|---|---|---|
| 5886.94 | 246 ± 12 | 0.08 ± 0.01 | −136 |
| 5887.15 | 127 ± 6 | 0.04 ± 0.01 | −126 |
| 5888.06 | 148 ± 7 | 0.05 ± 0.01 | −79 |
| 5888.42 | 234 ± 12 | 0.08 ± 0.01 | −61 |
| 5888.82 | 171± 9 | 0.05 ± 0.01 | −41 |
| 7698.37 | 103 ± 5 | 0.39 ± 0.02 | −7 |
| 7698.62 | 140 ± 7 | 0.54 ± 0.02 | 3 |
| Total | | 1.23 ± 0.09 | |

### 3.2.2 Distance

In order to derive distance, we used the reddening value found in Section 3.2.1 in conjunction with a 3D Galactic center reddening map from Schultheis et al. (2014), found using data from the *Vista Variables in the Via Lactae* (*VVV*) survey. The *VVV* survey is a ESO large program using the 4-meter VISTA telescope to take near-IR photometry ($0.9-2.5\mu$m) of 520 square degrees towards the Milky Way Bulge to characterize variable sources. The reddening map was one of the byproducts of the exquisite *VVV* photometric dataset. The 3D map gives $E(J-K)$ reddening values as a function of: Galactic longitude (in intervals of 0.1°), Galactic latitude (in intervals of 0.1°), and radial distance (in intervals of 0.5 kpc, extending out to 10 kpc).

To make use of the map, we needed to transform our $E(B-V)$ value into an $E(J-K)$ value given in the reddening map. To do this we found a coefficient, $\gamma$, such that $E(J-K) = \gamma E(B-V)$. The value of $\gamma$ was determined using the *VVV* survey color transforms from Table 1 in Saito et al. (2012). These color transforms give the relative extinction for the *VVV* filter system in terms of $E(B-V)$, assuming a standard extinction law of Cardelli et al. (1989). From these correction values we found a $\gamma$ value of 0.502, which gives $E(J-K) = 0.58 \pm 0.06$ for our reddening value of $E(B-V) = 1.16 \pm 0.12$.

We used the average of the four points in the reddening map closest to the coordinates of V1324 Sco (RA = 17:50:53.90, Dec = −32:37:20.5) for our analysis. Figure 3.4 shows $E(J-K)$ versus radial distance $r_D$ for the reddening map values, as well as our derived value for V1324 Sco's $E(J-K)$ reddening.

The dashed blue line in Figure 3.4 shows the $1\sigma$ maximum for our derived $E(J-K)$ reddening (0.62); it is clear that this value is consistent with any distance $> 6.5$ kpc. Because of this degeneracy in $E(J-K)$ reddening we can only place a lower limit of 6.5 kpc on the distance to V1324 Sco.

## 3.3 The Progenitor System

If V1324 Sco had a giant companion like V407 Cyg then the wind from the companion could explain its exceptionally high gamma-ray luminosity. To determine if this is a feasible explanation, we need to determine

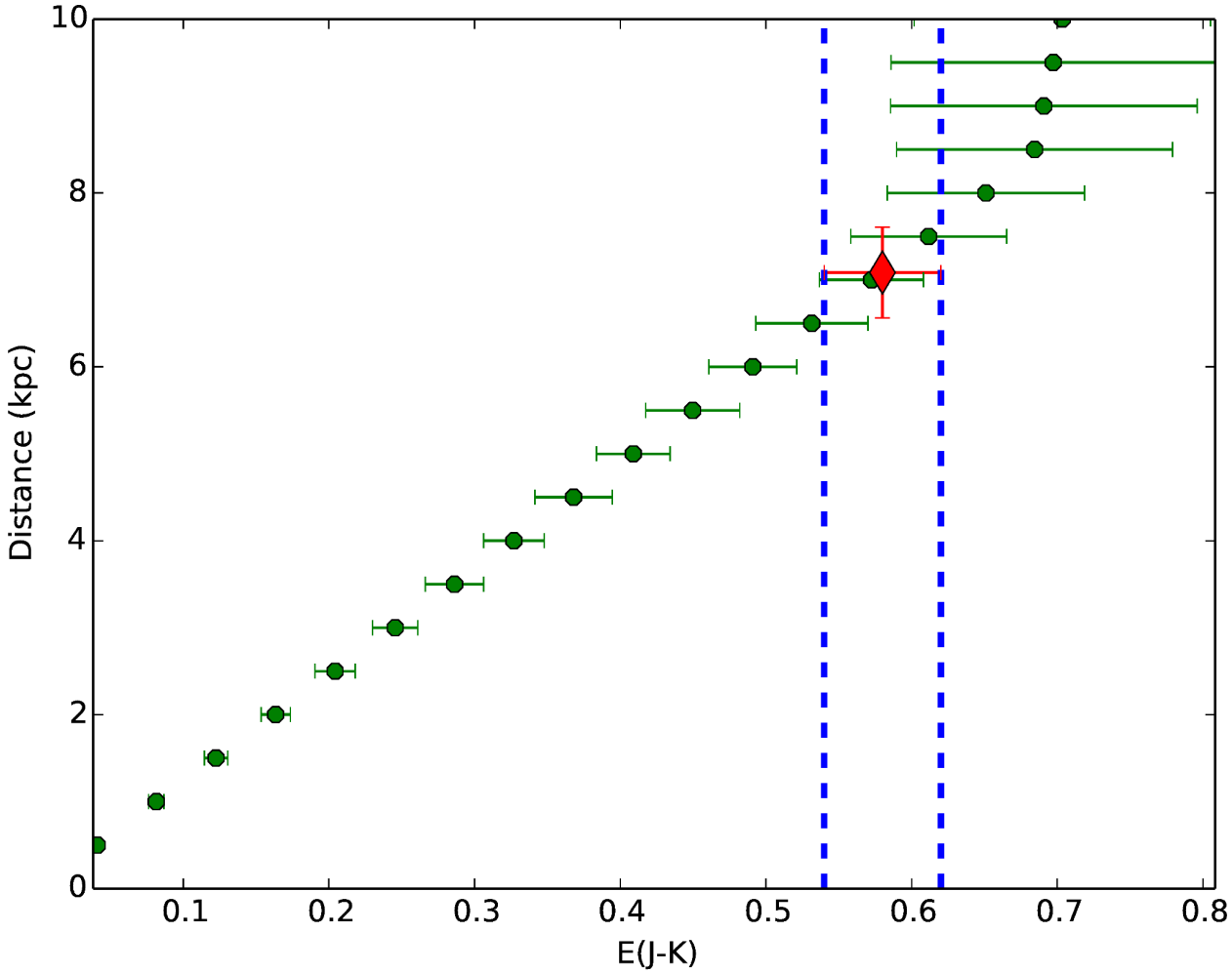


Figure 3.4 The green data points give the (average) $E(J-K)$ reddening values as a function of distance at the position of V1324 Sco, taken from the 3D reddening map of Schultheis et al. (2014). The red diamond indicates the derived reddening. The blue dashed lines show the $1\sigma$ extent of the derived reddening; it is clear that this value is consistent with all reddening values past 6.5 kpc.

if the progenitor system to V1324 Sco has a giant secondary star. The strongest photometric constraints on the secondary star comes from the *VVV* Survey (Minniti et al., 2010), which obtained several epochs of near-IR photometry on the target field between July 2010 and September 2011. We searched the catalog for all stars with non-zero $K$-band magnitude in a 15'×15' cutout centered on the coordinates of V1324 Sco ($N \approx 25,000$). To qualify as a star, an object had to have a *pStar*[1] value $> 0.9$. From this sample we found that 99% of the sources had $m_K < 16.626$; given that V1324 Sco was not detected by the *VVV* survey, we use this value as a limiting magnitude.

Table 1 in Saito et al. (2012) gives the filter specific extinction for the *VVV* $K$ band as $A_K/E(B-V) = 0.364$, and we can use our derived reddening value to obtain a $K$-band extinction of $\sim$ 0.42 mags. Without a proper upper bound on the distance to V1324 Sco, we cannot place an upper limit on the distance modulus. However we can say that if V1324 Sco were at a distance of $\gtrsim 9.5$ kpc, then the distance modulus would be $\approx 15.3$, meaning that the absolute $K$-band limit would be bright enough for the companion to be a very faint giant ($M_K \geq 1.3$, corresponding to a spectral type G5 giant (Covey et al., 2007)). However, if V1324 Sco is at the galactic center ($\sim 8.5$ kpc) then it must have a dwarf companion.

While this limit is not stringent enough to rule out a giant companion, by analyzing the period of V1324 Sco we show that a main sequence companion is strongly favored.

### 3.3.1 Constraints from the Orbital Period

Darnley et al. (2012) created a classification system for novae according to their orbital period which is a proxy for luminosity class of the secondary star. We utilize this classification scheme to help constrain the companion to V1324 Sco.

Measurements of the binary orbital period were found in the original photometry from the MOA group, who detected periodic modulations in the brightness of V1324 Sco (Wagner et al., 2012). These modulations were on the order of $\sim 0.1$ mag, with a period of $\sim 1.6$ hours. However, it is possible that there ellipsodial variations in the photometric light curve, which would give a secondary minimum and maximum. As a result, we consider both 1.6 and 3.2 hours for the period in our analysis.

Interestingly, if the period is 1.6 hours, V1324 Sco would be below the period gap, meaning that the angular momentum loss is driven by gravitational radiation (Knigge, 2011). Only a handful of novae fall below the period gap (Wagner et al., 2012), and it has been postulated that these systems may have a different type of mass transfer mechanism that takes place in this period range (Uthas et al., 2010).

Using the value for the period within the framework of Darnley et al. 2012 (Figure 3.5) we see that

[1] *pStar* is determined by taking the flux for different aperture sizes (e.g. $r/2$, $r$... $32r$, where $r$ is fixed based on the seeing) to determine the "sharpness" of the object profile. This, combined with the ellipticity of the object, is used to generate a statistical measure of the probability that the object is a star (Irwin et al., 2004).

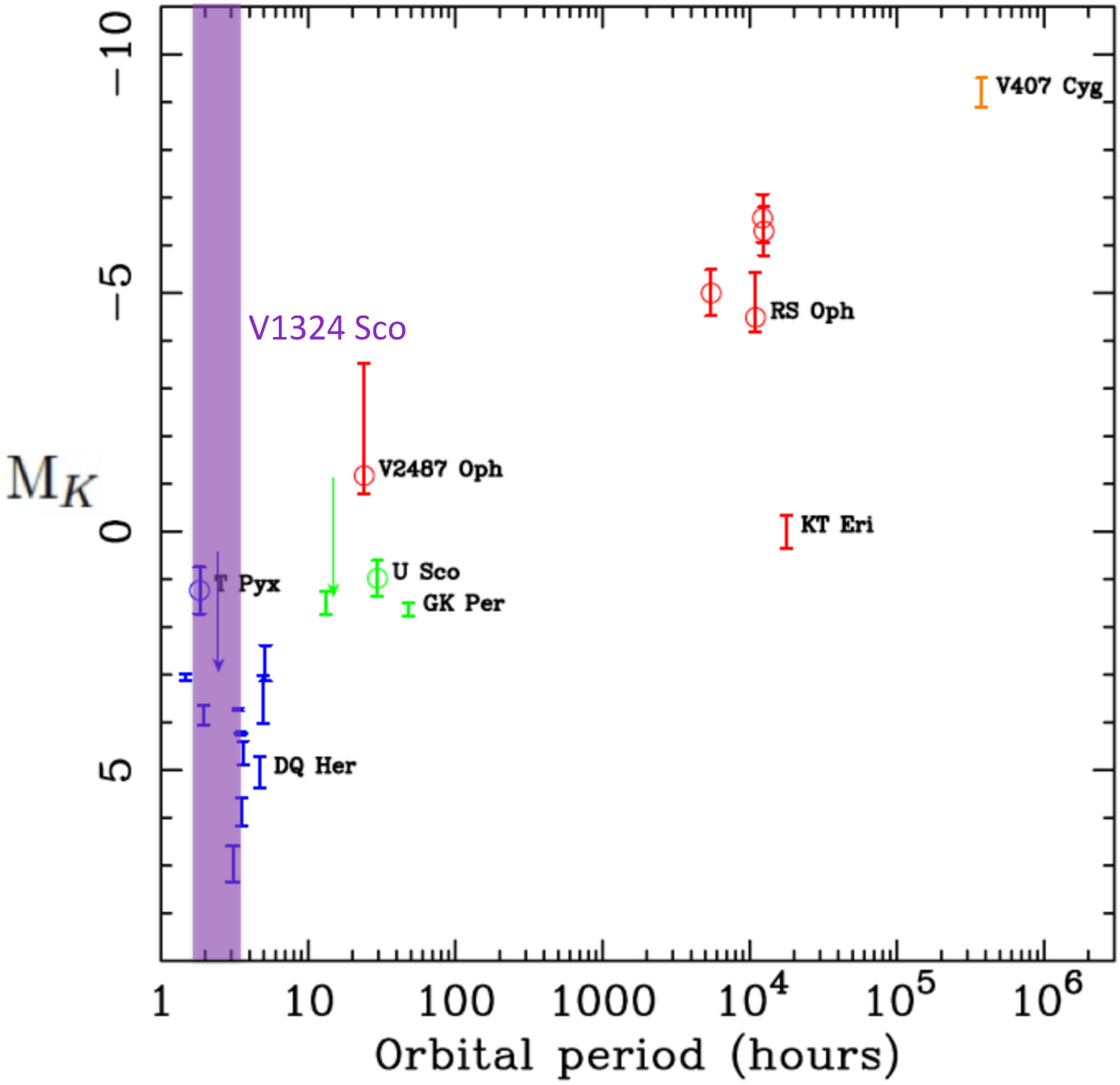


Figure 3.5 Plot showing the distribution of novae as a function of absolute $K$-band magnitude and binary orbital period, taken from Darnley et al. (2012). V1324 Sco is marked as the purple transparent line, indicating that we know the period $\sim$ 1.6 hours, but we cannot place a limit on the absolute $K$-band magnitude. The width of the purple line corresponds to the fact that the period could either be 1.6 or 3.2 hours. The colors on the plot correspond to the luminosity class of the secondary: blue is main sequence, green is sub-giant, and red is giant.

V1324 Sco (the purple dashed line) most likely falls into the region of blue points, indicting that it has a main sequence companion.

## 3.4 Determining Ejecta Mass as Measured from the Radio Light Curve

We modeled the secondary radio bump, which we interpret to be thermal emission from the expanding ejecta. We fit the radio data observed after day +106 (see Figure 2.8) using the standard model of Hjellming et al. (1979). Specifically, we utilize a homologously expanding Hubble flow model, with an inner and outer radius that is given as a ratio that we refer to as $\tilde{r}$, and an $r^{-2}$ density profile (for more details on this model see Seaquist & Palimaka 1977). The other physical quantities that go into the Hubble flow model (ejecta mass, ejecta velocity, temperature, and distance) are degenerate, and cannot be solved for individually. To circumvent this issue, we defined two composite variables that can be determined uniquely. These two variables are defined as

$$\Psi \equiv \frac{2k_b T_e v_{max}^2}{c^2 D^2}; \tag{3.1}$$

$$\Xi \equiv 0.018 \text{ sec}^5\text{Hz}^2 \left[ T_e^{-3/2} v_{max}^{-5} \left( \frac{M_{\rm ej} Z}{\bar{\mu}} \right)^2 \right]_{\rm cgs} g_{ff} f_V^{-1}, \tag{3.2}$$

where $T_e$ is the temperature of the emitting region, $v_{\rm max}$ is the maximum velocity of the ejecta, $D$ is the distance, $M_{\rm ej}$ is the mass of the ejecta, $Z$ is the average charge of the emitting particles, $f_V$ is the volume filling factor of the ejecta (discussed further in Appendix A), and $\bar{\mu}$ is the average particle mass. In simple terms we can think of $\Psi$ as setting the flux scale—as it contains the terms for the blackbody function and the angular size, which combine to give the total flux—and $\Xi$ as setting the time scale for the ejecta to become optically thin—as $\Xi$ is just all of the opacity terms collected into a single variable. Rewriting our expression for total flux and optical depth, we find

$$S_\nu = \Psi t^2 \nu^2 \left[ \int_0^{\tilde{r}_{min}} \tilde{a}(1 - e^{-\tau_1(\tilde{a})}) d\tilde{a} + \int_{\tilde{r}_{min}}^1 \tilde{a}(1 - e^{-\tau_2(\tilde{a})}) d\tilde{a} \right], \tag{3.3}$$

where $S_\nu$ is the observed flux and

$$\begin{aligned} \tau_1(\tilde{a}) &= \frac{\Xi\ \nu^{-2} t^{-5}}{4\pi[1 - \tilde{r}_{min}]} \int_{\sqrt{\tilde{r}_{min} - \tilde{a}^2}}^{\sqrt{1-\tilde{a}^2}} \frac{d\tilde{s}}{(\tilde{a}^2 + \tilde{s}^2)^2}; \\ \tau_2(\tilde{a}) &= \frac{\Xi\ \nu^{-2} t^{-5}}{4\pi[1 - \tilde{r}_{min}]} \int_0^{\sqrt{1-\tilde{a}^2}} \frac{d\tilde{s}}{(\tilde{a}^2 + \tilde{s}^2)^2}, \end{aligned} \tag{3.4}$$

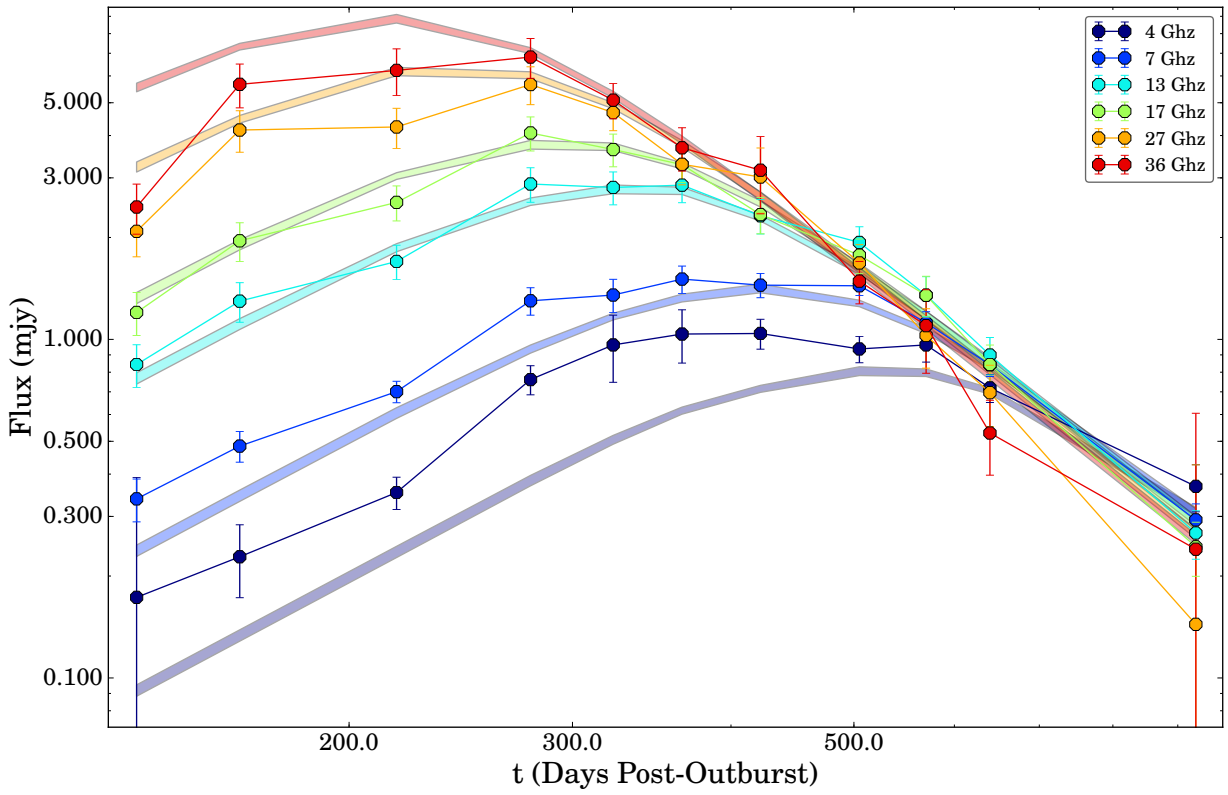


Figure 3.6 Best fit model to *just* the second bump portion of the radio light curve (see Figure 2.8 for the entirety of the radio light curve). The best fit parameter values and the resultant physical values can be found in Section 3.4. The reduced chi-squared value fit for this model is $\chi^2_{red} = 3.36$. The fitting scheme was error weighted, which (partially) explains the relatively poor fits to the highest and lowest frequencies. There is the further issue of the fact that none of the data have the canonical optically thick spectral index of $\alpha = 2.0$, which the model expects (see Figure 2.9).

where $\tau$ is the optical depth (a measure of how easy it is for light to escape before being absorbed or scattered). We also fit the previously mentioned variable $\tilde{r}_{min}$—the ratio of the inner and outer radius of the ejecta shell—giving us a total of three variables to fit in our model. A more detailed derivation of these relations is provided in Appendix Section A.

The actual fitting procedure was done using the Markov Chain Monte Carlo program *pymc* (Patil et al., 2010). This procedure was selected as it does not enforce a Gaussian distribution of best fit parameters, allowing us to more accurately characterize the full variance of our results.

Due to the exceptionally large parameter space occupied by our composite variables (many orders of magnitude), our sampling for the MCMC scheme was done in $\log(\Xi)$ and $\log(\Psi)$ space, and our results are given as such. Our best set of parameters are $\log(\Psi) = -24.487^{+0.033}_{-0.031}$, $\log(\Xi) = 59.763^{+0.03}_{-0.06}$, and $\tilde{r}_{min} = 0.447^{+0.10}_{-0.079}$.

Figure 3.6 shows the fit to the second bump using these parameters. The fitting scheme was error

weighted, which partially explains why the highest/lowest frequencies are not fit as well. The reduced chi-squared value fit for this model is $\chi^2/\nu = 3.36$. Further, by construction the model has a spectral index of $\alpha = 2.0$ during the rise, as this is the spectral index of optically thick thermal emission in the Rayleigh-Jeans tail. As can be seen in Figure 2.9 we never observe a spectral index this high.

We can derive physical parameters for the ejecta—e.g. velocity ($v_{\rm max}$) and ejected mass ($M_{\rm ej}$)—from $\Xi$ and $\Psi$ by using the canonical nova temperature of $10^4$ K (Osterbrock, 1989; Cunningham et al., 2015), the lower bound distance of Finzell et al. (2015) (6.5 kpc), and the filling factor value derived in Appendix B (also using $T_e = 10^4$ K). We also approximate the uncertainties as being a Gaussian distribution. The physical quantities derived from this are

- $v_{\rm max}$ =$1150 \pm 40$ km s$^{-1}$
- $M_{\rm ej}$ =$2.0 \pm 0.4 \times 10^{-5}$ $M_\odot$,
- $E_{\rm ej}$ =$2.6 \pm 0.6 \times 10^{44}$ ergs,

where the uncertainty quoted is the $1\sigma$ value. The majority of the uncertainty comes from the reddening value and a fiducial flux calibration uncertainty.

We have also assumed a fixed temperature and distance in our calculations. Calculating the dependence of $M_{\rm ej}$ on these two variables, we find that

$$\begin{aligned}
v_{max} &\propto D\Psi^{1/2}T_e^{-1/2};\\
M_{\rm ej} &\propto \Xi^{1/2}T_e^{3/4}v_{max}^{5/2}f_V^{1/2}\bar{\mu}Z^{-1};\\
f_V &\propto v_{max}^{-3}T_e^{-1}D^2;\\
\rightarrow M_{\rm ej} &\propto \Xi^{1/2}T_e^{3/4}v_{max}^{5/2}\left[v_{max}^{-3}T_e^{-1}D^2\right]^{1/2}\bar{\mu}Z^{-1}\\
&= \Xi^{1/2}T_e^{1/4}v_{max}D\bar{\mu}Z^{-1}\\
&= \Xi^{1/2}T_e^{1/4}\left[D\Psi^{1/2}T_e^{-1/2}\right]D\bar{\mu}Z^{-1}\\
&= \Xi^{1/2}T_e^{-1/4}\Psi^{1/2}D^2\bar{\mu}Z^{-1}.
\end{aligned}$$

Note that only the power-law contribution to $f_V$ was included, neglecting the *exponential* term. The true dependence on temperature is $M_{\rm ej} \propto T_e^{-1/4}\left[A\exp\left(B/T_e\right)-1\right]^{-1}$, where $A$ and $B$ are constants. As a result, $M_{\rm ej}$ is a very sensitive function of temperature. Given that $M_{\rm ej}$ scales positively with distance (i.e. an increase in distance leads to an increase in $M_{\rm ej}$), and that the distance used was a lower limit, we can think of the $M_{\rm ej}$ derived above as a lower limit.

It should be noted that, during the dust event, we expect some fraction of the nova ejecta to cool, recombine, and become neutral. Since neutral particles will not emit free-free emission—or, at least for atoms with significant dipole moments, they will emit significantly less free-free emission than ionized particles—we do not expect this mass to show up in the radio emission. However, we know from previous studies (see, e.g., Derdzinski et al. 2016 and references within) that the dust mass usually makes up no more than 0.1% of the total ejecta mass, so this discrepancy is negligible.

From the physical properties of the nova event derived above we find that V1324 Sco is very typical (see, e.g. Yaron et al. 2005).

## 3.5 OI Density Limits

The strong O I emission at 7774 Å and 8446 Å from the MIKE spectrum—seen in Figure 2.5—suggests a high density for the emitting material, as the relative strength of the line at 7774 Å compared to 8446 Å is a measure of the rate of collisional deexcitation (Williams, 2012). As 8446 Å is a fluorescent line, it should be substantially more dominant than all other O I lines; the only way for 7774 Å to even approach the strength of 8446 Å is if there are very high electron densities, such as at a radiative shock front. The forbidden [O I] line at 6300 Å can also be used as a density diagnostic, and we use it here in conjunction with the permitted O I lines.

We can use the oxygen line ratios of $j_{\lambda 7774}/j_{\lambda 6300}$ and $j_{\lambda 8446}/j_{\lambda 6300}$ to place constraints on the temperature, density, and ionizing radiation field (Kastner & Bhatia, 1995). This technique works best with high spectral resolution measurements, so we use the MIKE spectra taken on day +45. The other high resolution spectra—taken on day +3—had strong, confounding P-Cygni absorption features. Because the MIKE spectrum was not flux calibrated, we are tacitly assuming that the change in throughput of the spectrograph, as a function of wavelength, is small. After making the necessary reddening corrections (see Appendix B for more details) we found an average value of $\log(j_{\lambda 7774}/j_{\lambda 6300}) = 0.39 \pm 0.16$ and an average value of $\log(j_{\lambda 8446}/j_{\lambda 6300}) = 1.08 \pm 0.13$.

We can compare this to the work of Kastner & Bhatia (1995) and Bhatia & Kastner (1995), who use a simple model that assumes that the rate of excitation can be simply parameterized in terms of the electron number density ($N_e$), temperature ($T_e$), and rate of photoexcitation ($R_p$). Looking at the tables in Kastner & Bhatia (1995), if we assume a temperature of $T_e = 10,000$ K, these ratios are consistent with density $\log(N_e/[\mathrm{cm}^{-3}]) > 10$. Assuming that the density scales like $t^{-3}$, we would expect the density to be a factor of $\sim 10$ times greater during the first X-ray observation than it was on day +45. Combined with the fact that we expect the ejecta to have expanded to $\sim$ a few $\times 10^{14}$ cm, we derive a column density $\geq 10^{25}$ cm$^{-3}$.

As discussed in Section 2.3, such a high column density can explain the lack of hard X-ray emission.

We can also calculate the total mass that this density implies. Using a toy model where we assume a typical nova velocity of $\sim 1,000$ km s$^{-1}$, a mean molecular weight of $2.0 \times 10^{-24}$ grams/particle (i.e. solar metalicity), and a uniform density, this would correspond to a total ejecta mass of $\approx 2 \times 10^{-3} M_{\odot}$. Such a high ejecta mass is at odds with the mass derived from the radio light curve (discussed in Section 3.4). A plausible resolution to this discrepancy is if the line emitting region is the cooling region behind a radiative shock where we would expect the density to be substantially higher (Metzger et al., 2014).

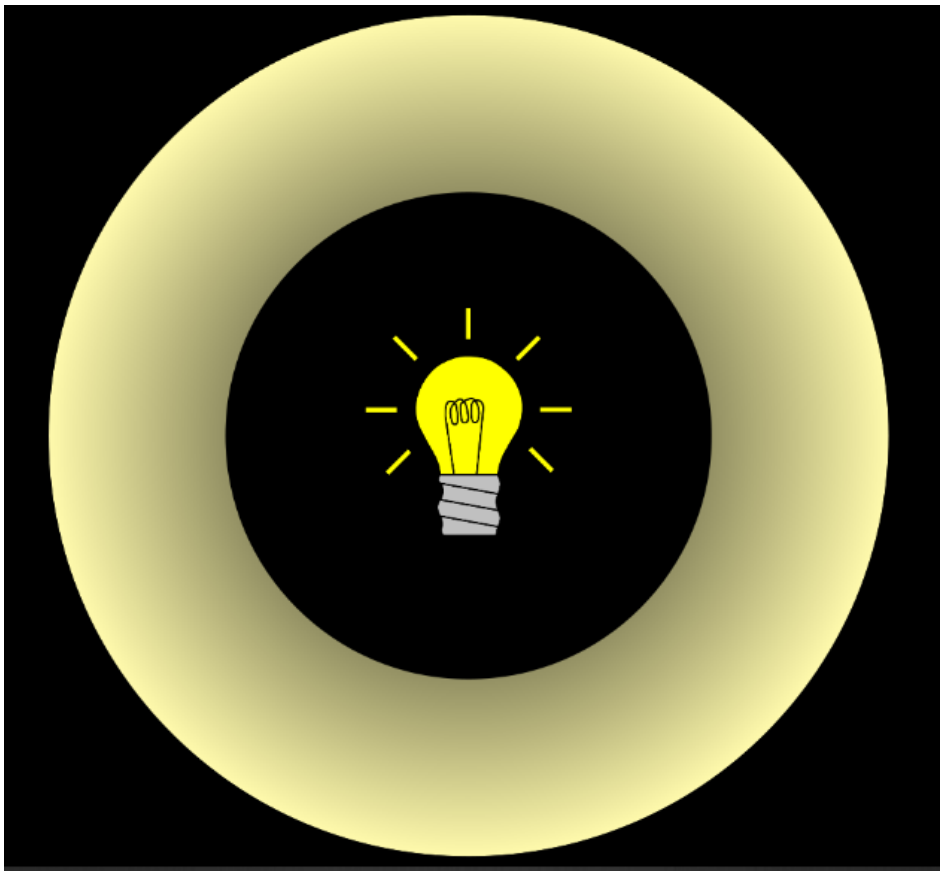

Figure 3.7 The standard model explanation for why novae get bright. In this representation we see the ejecta (pale yellow annulus) surrounding a light source (here a cartoon light bulb, but in actuality a still hot white dwarf). The standard model says that the light from a classical nova comes from the diffusion of energy from the "light bulb" at the center of the ejecta. This model, however, does not take into account light coming from shock interactions.

## 3.6 Determining Gamma-Ray/Optical Flux Ratio

In the model of Metzger et al. (2015), it was predicted that a shock that could be responsible for the gamma-rays could be radiative, producing a significant amount of X-ray emission as well. Given that no such X-rays

were observed—coincident with the gamma-ray emission—it was postulated by Metzger et al. (2015) that the X-rays were being absorbed by unshocked material upstream from the shock, and being reradiated at lower frequencies—most notably, in the optical.

This idea challenges the long held belief that the optical emission from classical novae comes from the energy of the burning white dwarf (see Figure 3.7), not a shock interaction. To test this model, we measured the ratio of the gamma-ray to optical flux, and compared this value to several models of shock interaction and gamma-ray production.

### 3.6.1 Determining Total Optical Emission

We estimated the total optical flux from V1324 Sco by assuming that the total emission could be modeled as a blackbody at some fixed temperature.

We utilized several epochs of both optical and near-IR photometric measurements for our analysis. We only used a subset of the photometric dataset, to insure that all of the measurements came from the same telescope with a known filter system (Walter et al., 2012). All photometric data points were corrected for both differential and total extinction, as well as a conversion from Vega to AB magnitudes.

To determine the best fit blackbody temperature, we convolved the filter response with the expected flux from a blackbody source. The expected flux values were compared with the flux measurements for our photometric data points. We iterated over multiple temperature values until we found the best fit value. Along with the best fit temperature, we also fit a scaling term that encapsulated the angular size of the source, which allowed us to compare with the flux received.

To make sure that we were adequately dealing with the error of our both our measurements and reddening corrections we adopted a Monte-Carlo approach, drawing random data points from a sample and assuming that the errors were normally distributed.

Taking all of these values together—i.e. the best fit temperature and scaling term—we were able to estimate the total optical flux emitted.

### 3.6.2 Determining Total Gamma-Ray Flux

Given the low photon count, Ackermann et al. (2014) gave several different parameters for determining the total gamma-ray flux, assuming different generating functions—either power-law or power-law with exponential cutoff.

We incorporated all of these potential best fit parameters by using a Monte-Carlo approach similar to the previous section. We drew best fit parameters from a normally distributed set, defined by the mean and

uncertainty given in Ackermann et al. (2014).

### 3.6.3 Results

Having two sets of measurements—one for the total optical flux and one for the total gamma-ray flux—we combined the two to determine the range of potential values for the optical to gamma-ray flux ratio.

Due to the large amount of uncertainty inherent in this task, our results had a large dynamic range. Specifically, it was large enough that a good deal of information was lost by taking the arithmetic mean and standard deviation. To better capture this information, we converted all values to be in log space, and the quoted mean and standard deviation were also given in terms of log values. See Figure 3.8 for the quantitative results.

This work can be seen as laying the ground work for Li (2017), setting out the framework for analysis and as a proof of concept. Li (2017) showed, definitively, that the optical light curve for the nova ASASSN-16ma was powered entirely by shock interactions, confirming the ideas put forward in Metzger et al. (2015), and ultimately favoring a Hadronic origin for the gamma-rays.

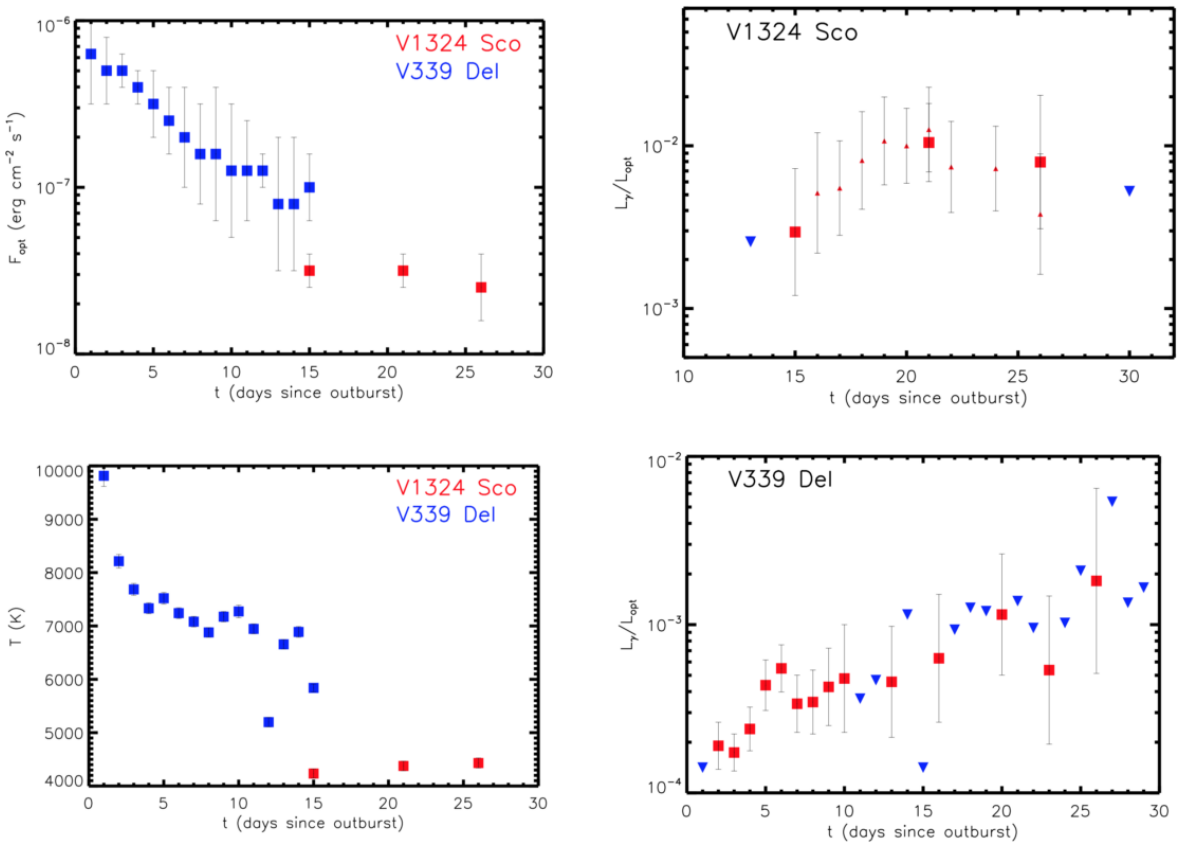


Figure 3.8 This plot, taken from (Metzger et al., 2015), shows the optical and gamma-ray properties for V1324 Sco (as well as V339 Del) as a function of time. *Upper Left:* Total optical flux as a function of time. The optical flux is calculated by fitting a blackbody function to the photometry. *Upper Right:* Gamma-ray to optical luminosity ratio, as a function of time, for V1324 Sco. Note that, for this panel and the one below it, the large red squares corresponds to fits with near-IR and $VBR$ photometry, while the little red squares are nights with just $V$-band photometry, and it was assumed to have the same bolometric correction as day 15. The blue triangles are for gamma-ray non-detections. *Lower Left:* Best fit temperature, derived from the optical photometry. *Lower Right:* Gamma-ray to optical luminosity ratio, as a function of time, for V339 Del. Note that the gamma-ray to optical luminosity ratio is significantly higher in V1324 Sco than in V339 Del.

# 4 Discussion

## 4.1 V1324 Sco: A Normal Nova

In this section we argue that all of the non-gamma-ray observational signatures of V1324 Sco are normal, in the sense that all of observational features have been seen in previous novae—although never all together in the same novae.

### 4.1.1 Optical Regime

In the optical regime, V1324 Sco is photometrically a *D* (Dusty) class nova (Strope et al., 2010), based on the not so ordinary dust event that took place between days +46 to +157. Other *D* class novae include: FH Ser, NQ Vul, and QV Vul. The speed of photometric decline is also quite normal. The $t_2$ value—that is, the time is takes for a nova to decline by 2 magnitudes in *V* band—of V1324 Sco is consistent with other *D* class novae, all of which are of order tens of days (e.g. FH Ser $t_2 = 49$ days, NQ Vul $t_2 = 21$ days, QV Vul $t_2 = 37$ days; see Strope et al. 2010 and references within), with V1324 Sco having a $t_2 \approx 24$ days.

Spectroscopically, V1324 Sco is a Fe II type nova (Williams et al., 1991), due to the prominence of the Fe II spectral features—the second strongest, behind the Balmer features—during optical maximum. The Fe II type classification is common among *D* type novae: FH Ser, NQ Vul, and QV Vul are also Fe II type (see Strope et al. 2010 and references within).

Note that we can also use the spectroscopic observations to determine properties of the ejecta density. Specifically, we use the late-time (nebular) spectroscopy to measure density inhomogeneities (i.e. clumpiness), which we parameterize in terms of the so called filling factor (see Appendix B for the detailed calculations). Such inhomogeneities must be taken into account in order to get a proper mass estimate, and we will incorporate the filling factor in our mass derivation in the next section.

We also use the permitted O I lines at 7774 Å and 8446 Å, and the forbidden [O I] line at 6300 Å, to constrain the column density (for at least one portion) of the ejecta to be $\geq 10^{25}$ cm$^{-2}$ (see Section 3.5 for the detailed calculations). As discussed in Section 2.3, such a high column density can explain the lack of hard X-ray emission.

Such large densities are quite common, as clumpiness is considered to be ubiquitous in novae (see, e.g., Slavin et al. 1995). Taking all of the properties discussed above into account, it is clear that—within the context of the optical regime—V1324 Sco is a normal nova.

### 4.1.2 X-ray Regime

In the X-ray regime, again, V1324 Sco is normal for a *D* class nova. Although the three novae we were previously using as examples all went into outburst before there was consistent X-ray monitoring of novae, we know from more recent *D* class novae that it is the norm—rather than the exception—for dusty novae to go undetected in X-rays. As discussed in Schwarz et al. (2011), only one *D* class nova has been detected in hard X-rays: V1280 Sco, although this detection was $\sim 800$ days after the beginning of the nova event. Note: Although not considered a *D* class nova, Schwarz et al. (2011) makes the case that V2362 Cyg is another dusty nova that has been X-ray detected.

A further two marginally dusty novae were detected as super-soft-sources (V2467 Cyg and V574 Pup, see Schwarz et al. 2011 and references within). Note that these two sources showed little to no change in their optical light; the presence of dust was only determined due to a modest increase in IR flux. On the other hand, six other dusty novae—including V1324 Sco—were observed but not detected in X-rays (V1324 Sco, V2676 Oph, V2361 Cyg, V1065 Cen, V2615 Oph, and V5579 Sgr; again, see Schwarz et al. 2011).

This lack of X-ray emission in dusty novae could be explained by the cool dense dust forming material absorbing the majority of the X-rays before they can escape. We find that, based on the X-ray observations, V1324 Sco is still a normal nova.

### 4.1.3 A Luminous Red Nova?

A Luminous Red Nova (LRN), observationally, appear brighter and with redder colors than a classical nova (see, e.g., Tylenda et al. 2011). The physical interpretation of these observational characteristics is that a LRN is the result of a merger of a close binary. V1309 Sco is one of the canonical LRNs, and its optical emission is very similar to V1324 Sco. Both have an initial, slow, monotonic rise, both have a flattening of the optical light curve near peak, and both have a significant dust event.

We find, however, that a luminous red nova does not fit with the observations of V1324 Sco. Specifically,

• The most generous estimate of the ejecta mass is still two orders of magnitude smaller than what is expected for LRN events, (Ivanova et al., 2013).

• There is still a detectable period during the power law decline phase of the light curve. This was determined using the MOA data set, which had the best sampling, as well as the highest cadence. The period was measured using the Lomb-Scargle algorithm in the Python scientific library *SciPy*. We limited the data set to $> 5\sigma$ detections.

Some facets of the LRN model, however, could explain features seen in V1324 Sco. For instance, in V1309 Sco, the physical explanation for the light-curve flattening near maximum is that the photosphere does not

grow–or grows very slowly–in Eulerian coordinates (and is shrinking in Lagrangian coordinates), due to the fact that the ejecta envelope is cooling, recombining, and becoming optically thin very rapidly. This could also explain the flattening of the optical light curve in V1324 Sco.

Another connection is that the early-slow rise phase of V1309 Sco (see Tylenda et al. 2011) is somewhat similar to that in the rise seen in V1324 Sco. In V1309 Sco the rise was interpreted by Pejcha et al. (2013) as being due to mass loss from L2. Likewise, Chomiuk et al. (2014) interprets the "initial" ejecta phase as being due to a "common-envelope" like ejection, which very well could manifest in its early stage also as L2 mass loss.

## 4.2 V1324 Sco: The Most Gamma-Ray Luminous Nova to Date

Having established in the previous section that V1324 Sco is—in all non gamma-ray observations—a normal nova, we now discuss what about this nova could cause it to have such an extremely high gamma-ray luminosity. There is strong observational evidence for a shock interaction, both from the gamma-rays and from the radio. We discuss here the observational evidence tied to the shock, as well as the physical properties of the nova event—e.g. velocity, density, etc.—that could give rise to differences the in gamma-ray luminosity.

### 4.2.1 Velocity Variations

Looking at Figure 2.6, it is clear that the Balmer line velocities change as a function of time. The spectroscopic velocities for H$\alpha$ and H$\beta$ are plotted in Figure 4.1, along with the photometric light curve for comparison purposes. All velocities quoted are half-width at half-maximum (HWHM) measured for each line. A number of the spectra taken by Walter were either blue (3650Å − 5420Å) or red (5620Å − 6940Å). Given that H$\alpha$ and H$\beta$ were were consistently strong in all the spectra we analyzed, we chose to use these two features for our measurements in order to maximize the number of velocity measurements. The HWHM was measured by fitting a Gaussian profile to the emission lines using the IRAF routine *splot*. The uncertainties were found by adding in quadrature both the uncertainty in the line measurement—found by measuring the line multiple times in *splot*—and the (average) dispersion of the spectrum. Note that the velocity rises approximately concurrent with the gamma-ray emission (day +14 to +30, marked as a grey shaded region in Figure 4.1).

We see a similar increase in the H$\alpha$ profile of another gamma-ray nova, V339 Del. Figure 4 of Skopal et al. (2014) show that the wings of the H$\alpha$ profile—especially in the red—began to increase on 2013 August 18 (date of the first gamma-ray detection). Figure 8 of Skopal et al. (2014) shows a dramatic increase in the H$\alpha$ line widths in the blue starting no later than 2013 August 20. It is unclear what the magnitude of

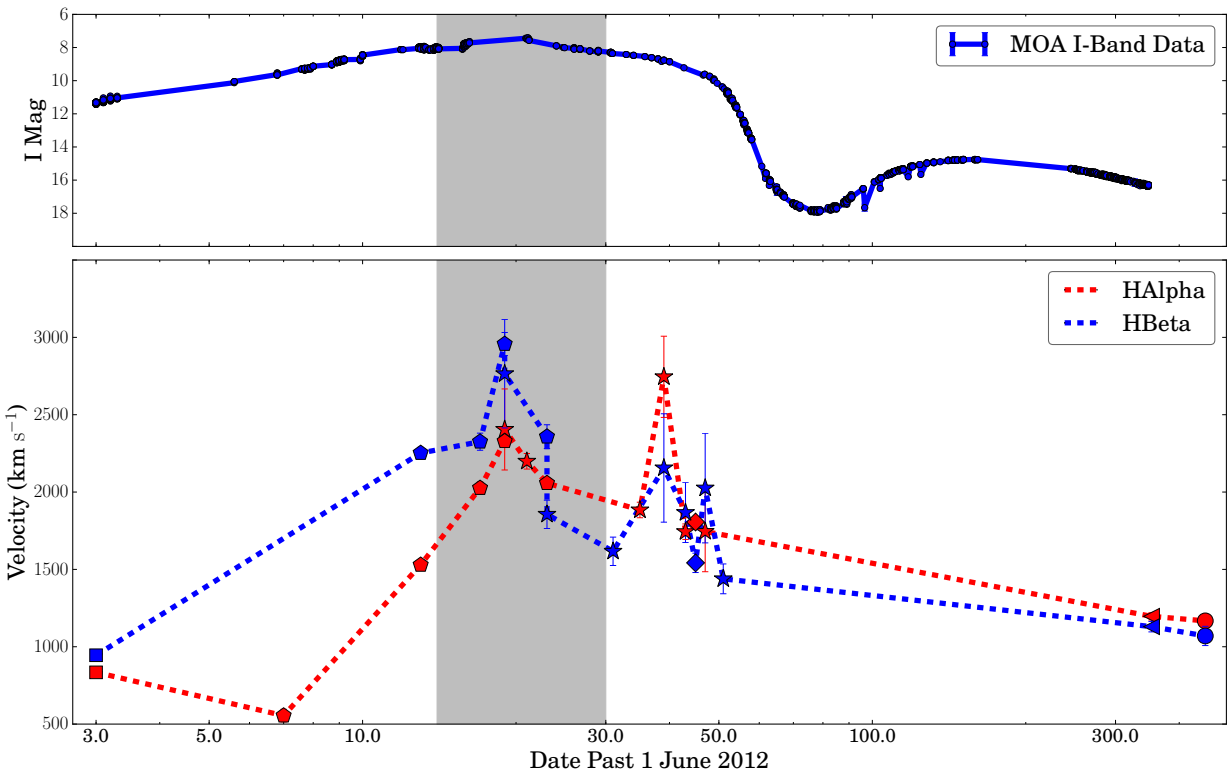


Figure 4.1 Top Panel: A subset of the $I$ band light curve in Figure 2.1, given here for reference. Bottom Panel: Evolution of the velocities of both H$\alpha$ and H$\beta$. Both velocities are found by taking the Half-Width at Half Maximum HWHM of the spectral feature. The gray shaded region indicates the period of gamma-ray emission (Ackermann et al., 2014). This increase in velocity—coincident with the gamma-ray emission—is interpreted as being a signature of the shock interaction.

the velocity increase was in V339 Del, however, as Skopal et al. (2014) give only measured velocities for the absorption components. Further, it is also unknown if the increase in H$\alpha$ line widths persisted once V339 Del became gamma-ray quiet or if the wings shrank back, as seen in V1324 Sco. Further analysis is required for the early time spectra of V339 Del to properly compare its velocity increase to V1324 Sco.

There are three potential explanations for the observed increase in the Balmer line radial velocity.

• An increase in the ejecta speed. This is what is usually thought to be the case in novae when an increase in Doppler velocity is observed (Kovetz, 1998; Schwarz et al., 2001). The best argument against this interpretation is that—along with the increase in velocity—we also see a change in the structure of the spectral profile. Specifically, we see a double horned profile that is characteristic of bipolar ejected material (see Figure 4.1, between days 31 to 45).

• A recombination wave passing through the outer envelope of the ejecta. This type of model has been proposed to explain flattening of the optical light curves observed in SNe-II P and Luminous Red Novae, wherein expansion cools the ejecta to the point where hydrogen recombines (see Section 4.1.3 for further

details). The now neutral hydrogen can no longer radiate via free-free emission. This process is referred to as a recombination wave, and it would have a significant effect on the structure of the emission lines (see, e.g., Shore et al. 2011). We cannot rule out the possibility that a recombination wave is causing the changes in the Balmer emission lines. However, it is unclear if this would necessarily increase the line velocity or just change the shape of the line profile.

• A different, faster, ejecta component—*behind* the previously observed H$\alpha$ emitting region—slams into the previously observed slower region of material, becoming visible. We find this to be the most likely explanation, as it can explain both the increase in velocity and change in shape of the spectral feature.

It should be noted that this derivation of the velocity is an oversimplification. It is well known that there are multiple velocity components in novae spectra that need to be disentangled (see, e.g., Gill & O'Brien 1999). However, it does serve to put at least some kind of bound on the velocities.

### 4.2.2 Early Time Radio Emission

The initial radio bump—seen in Figure 2.8 starting on day +25 and going until day $\sim$ 106—is a strong indicator of a shock. The bump was too early to be the thermal emission normally seen in novae. To illustrate the non-thermal nature of the initial radio bump, we can use the brightness temperature, which is the temperature necessary for the observed flux to be purely thermal (assuming some distance and velocity). The equation for brightness temperature is given by

$$T_b(\nu, t) = \frac{S_\nu(t) c^2 D^2}{2\pi k_b \nu^2 (v_{\rm ej} t)^2}, \tag{4.1}$$

where $S_\nu$ is the observed flux, $D$ is the distance, $t$ is the time, and $v_{\rm ej}$ is a fiducial ejecta velocity. We use the brightness temperature as a measure of the deviation from what we would expect from a thermally emitting gas at $10^4$ K. Figure 4.2 shows the maximum brightness temperature as a function of time (using the distance lower limit of 6.5 kpc from Finzell et al. 2015 and a velocity of 1,000 km s$^{-1}$). Note that two observation epochs (days 80 and 92) were removed due to the lack of low-frequency observations, which usually set the maximum brightness temperature.

This type of initial radio bump has been seen in several other nova, including QU Vul (Taylor et al., 1987, 1988), V1723 Aql (Weston et al., 2016a), and V5589 Sgr (Weston et al., 2016b) and we are beginning to develop theories to explain such behavior. In Taylor et al. (1987), Metzger et al. (2014), and Weston et al. (2016a) it is postulated that the initial radio bumps could be thermal free-free or synchrotron emission—although Weston et al. (2016a) come down strongly in favor of the non-thermal model.

To get such high thermal emission at early times, both Taylor et al. (1987) and Metzger et al. (2014)

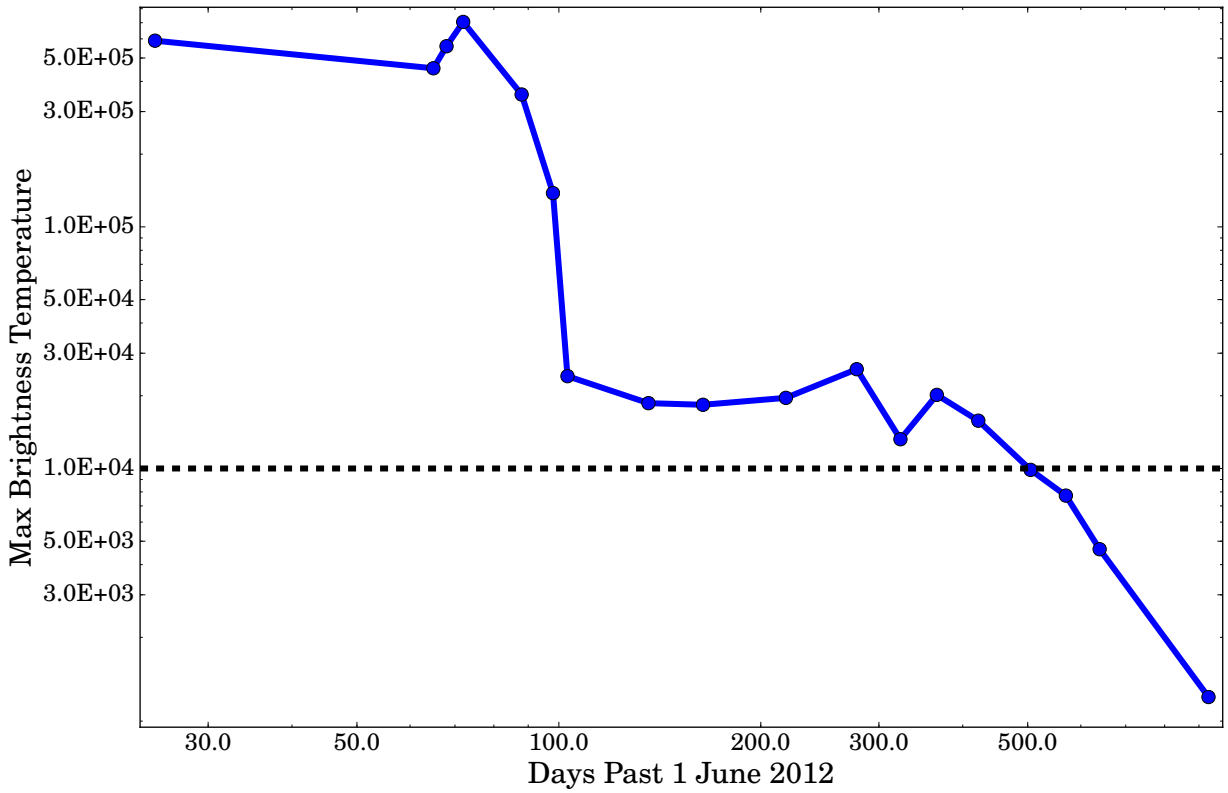


Figure 4.2 The early time radio bump (day 30 to 50) has maximum brightness temperatures far exceeding that of the canonical $10^4$ K thermally emitting ejecta—which can be seen as the dashed black line. The first radio observation, on day +25, occurred while the source was still gamma-ray bright. Note that the observation epochs taken on days 88 and 92 were omitted due to a lack of low-frequency observations.

invoke a strong shock as a means for generating hot, free-free emitting gas. Such high temperature gas would also produce significant X-ray emission, which was not observed in V1324 Sco. This can be explained if there is a high column density of material adjacent to the X-ray emitting region (see Section 2.3).

On the other hand, Taylor et al. (1987) and Vlasov et al. (2016) acknowledge that the emission could be coming from synchrotron emission. In the case of QU Vul, Taylor et al. (1987) invoke the Razin-Tsytovich effect to explain the high spectral-index ($\alpha = 2.42 \pm 0.04$) during the initial radio bump. Vlasov et al. (2016) find that you can also achieve a spectral index $> 2.0$ if the expanding ejecta are not isothermal, but have some temperature structure. There is no such evidence of the ejecta in V1324 Sco being non-isothermal, as the spectral index remains at or below 2 throughout the entire initial radio bump.

Vlasov et al. (2016) found that, for low-velocity shocks ($v_{sh} < 1000$ km s$^{-1}$), line emission dominates the cooling and is very efficient, driving the gas temperature to $T \sim 10^4$ K. This makes it very difficult to achieve the $\sim 10^6$ K gas necessary for the initial radio emission to be explained by thermal emission. The radio data favor a shock velocity $\leq 1,000$ km s$^{-1}$, as we show in Section 3.4. This means that the shock is

likely very radiatively efficient, making the thermal emission model for the early radio bump less likely than the non-thermal emission model.

### 4.2.3 Physical Parameters of the Shocking Media

In order to determine what could cause the extreme gamma-ray luminosity, we first determine—in an analytical fashion—the physical quantities that affect the gamma-ray luminosity. We present here a very simplified model of the ejecta that can explain the gamma-ray emission. We can imagine the ejecta as being composed of two parts: a slow initial component and a fast secondary component. When these two components meet, there will be both a forward and reverse shock, and it is these shocks that will power the gamma-ray emission. We further assume that these shocks are radiative, so we expect there to be a layer of cold material between the forward and reverse shocks. Most of this analysis is based on the models of Metzger et al. (2014) and Vlasov et al. (2016).

We assume that the slow component has the"pulse" density profile given in Metzger et al. (2014), which is defined to be

$$n_{\rm s}(r) = \left(\frac{\dot{M}_{\rm s}}{4\pi f_\Omega v_{\rm s} r^2 \mu m_p}\right) \exp\left[-\frac{r}{R_{\rm s}}\right], \tag{4.2}$$

where $\dot{M}_{\rm s}$ is the slow component mass loss rate, $\mu$ is the mean molecular weight, $f_\Omega$ is the solid angle fraction that is subtended by the slow component, $v_{\rm s}$ is the velocity of the slow component, and $R_{\rm s}$ is the radius of the slow component ($R_{\rm s} = v_{\rm s} t_{\rm s}$, where $t_{\rm s}$ is the time since the slow component was ejected).

Likewise, the fast component has a density profile given by

$$n_{\rm f}(r) \approx \frac{\dot{M}_{\rm f}}{4\pi v_{\rm f} r^2 \mu m_p}, \tag{4.3}$$

where $\dot{M}_{\rm f}$ is the fast component mass loss rate, $v_{\rm f}$ is the velocity of the fast component.

Assuming that the shocks are radiative, there will be a cold layer of material between the forward and reverse shocks (note that this is also the region where dust will eventually form Derdzinski et al. 2016). We will denote the mass of this shell as $M_{\rm shell}$, which grows in time as

$$\frac{dM_{\rm shell}}{dt} = \dot{M}_{\rm f}\left(\frac{v_{\rm f} - v_{\rm shell}}{v_{\rm f}}\right) + f_\Omega^{-1}\dot{M}_{\rm s}\frac{(v_{\rm shell} - v_s)}{v_s}, \tag{4.4}$$

while the momentum grows as

$$\frac{d}{dt}\left(M_{\rm shell} v_{\rm shell}\right) = \dot{M}_{\rm f}(v_{\rm f} - v_{\rm shell}) + f_\Omega^{-1}\dot{M}_{\rm s}(v_{\rm shell} - v_{\rm s}). \tag{4.5}$$

A steady state solution (i.e. $dv_{\rm shell}/dt = 0$) will be reached quickly, wherein the cool shell reaches a final "terminal" velocity. To make this problem more tractable, we assume that $\frac{v_{\rm s}}{v_{\rm f}} \ll 1$ and $\frac{f_\Omega \dot{M}_{\rm f}}{\dot{M}_{\rm s}} \lesssim 1$. In this limit we find that

$$\frac{v_{\rm shell}}{v_{\rm s}} \approx \left( \frac{\dot{M}_{\rm f} v_{\rm f} f_\Omega}{M_{\rm s} v_{\rm s}} \right)^{1/2}. \tag{4.6}$$

The power dissipated by the shocks is determined by the number of thermal particles swept up by the shock, which can be expressed as

$$\dot{E}_r = \frac{9}{32} f_\Omega \frac{\dot{M}_{\rm f}}{v_{\rm f}} (v_{\rm f} - v_{\rm shell})^3 \tag{4.7}$$

$$\dot{E}_f = \frac{9}{32} \frac{\dot{M}_{\rm s}}{v_{\rm s}} (v_{\rm shell} - v_{\rm s})^3. \tag{4.8}$$

Since usually $v_{\rm shell} \ll v_{\rm f}$, the shock power will be dominated by the reverse shock,

$$L_\gamma \propto \dot{E}_r \approx \frac{9}{32} f_\Omega \dot{M}_{\rm f} v_{\rm f}^2. \tag{4.9}$$

To determine the amount of time that the gamma-ray emission will persist—hereafter referred to as $t_\gamma$—we need to find the amount of time it will take for the shock to cross the initial slow component, i.e. $R_{\rm shell} \approx R_{\rm s} = v_{\rm s} t_{\rm s}$. Rewriting this using our expression for the shock velocity, we find

$$t_\gamma = \frac{R_{\rm s}}{v_{\rm shell}} = t_{\rm s} \left( \frac{\dot{M}_{\rm s} v_{\rm s}}{\dot{M}_f f_\Omega v_{\rm f}} \right)^{1/2}. \tag{4.10}$$

In the case where $\dot{M}_{\rm f} v_{\rm f} \gg \dot{M}_{\rm s} v_{\rm s}$ (where $t_{\rm s}$ is the amount of time since the slow initial component was ejected). In such a situation $t_\gamma$ can be simplified to

$$t_\gamma \approx \left( \frac{\dot{M}_{\rm s} v_{\rm s}}{f_\Omega \dot{M}_{\rm f} v_{\rm f}} \right)^{1/2} t_{\rm s} \propto \left( \frac{\dot{M}_{\rm s} v_{\rm s} v_{\rm f}}{L_\gamma} \right)^{1/2} t_{\rm s}. \tag{4.11}$$

We can see that increasing either $\dot{M}_{\rm f}$ or $v_{\rm f}$ will increase $L_\gamma$ while decreasing $t_\gamma$. This inverse relationship between the gamma-ray luminosity and the duration of the gamma-ray emission has been observed by Cheung et al. (2016).

We posit that it is the fast secondary component that is key in determining the total gamma-ray luminosity, and it is this component that made V1324 Sco the most gamma-ray luminous nova detected to date. It is unclear whether it is the fast component's velocity, mass, or a combination of the two that sets V1324 Sco apart from the other gamma-ray detected novae. This theory can be tested by comparing both

the velocity evolution of the ejecta (similar to the analysis of Section 4.2.1) and ejecta mass (similar to the analysis of Section 3.4) for multiple gamma-ray detected novae.

# 5 Conclusions

## 5.1 V1324 Sco Wrap Up

We have collected a large, multi-wavelength dataset for the most gamma-ray luminous nova observed to date, V1324 Sco. Using this dataset we have been able to tightly constrain the physical features of this nova, allowing us to use it as a prototype for comparison to other gamma-ray detected novae. Specifically, we derived the following:

- Using interstellar absorption lines—Na D, K, and Diffuse Interstellar Bands—we derived a reddening value of $E(B-V) = 1.16 \pm 0.12$.
- By comparing this reddening value to the three-dimensional reddening maps of Schultheis et al. (2014), we found a lower-limit on the distance of $\geq 6.5$ kpc.
- Using the orbital period and constraints on the absolute $K$-band magnitude, we found that the progenitor system most likely has a main-sequence companion.
- By fitting the second bump of the radio light curve—and utilizing the previously derived filling factor—we derived an ejecta mass of $2.0 \pm 0.4 \times 10^{-5}$ $M_{\odot}$, an ejecta velocity of $1150 \pm 40$ km s$^{-1}$, and an ejecta energy of $2.6 \pm 0.6 \times 10^{44}$ ergs.
- Comparing these derived values—along with qualitative features from the optical—we showed that V1324 Sco is, for all intents and purposes, a "normal" nova.

## 5.2 Shocks in Novae

Being the most gamma-ray luminous nova observed to date, the work done on V1324 Sco can be viewed as laying the ground work for all future on gamma-ray novae, having one of the most complete datasets of any nova. The most substantiative breakthrough came from the work of Metzger et al. (2015), where it was shown that the emission at optical maximum was powered by shocks, rather than the diffusion of energy from the hot white dwarf, as the canonical model of novae posits. This was shown by comparing the particle acceleration efficiency necessary to explain the gamma-ray production with the total amount of optical emission. Through detailed calculations of the shock interaction, it was shown that we would expect the gamma-ray producing shock to also produce $> 10\%$ of the total optical emission in V1324 Sco.

The first opportunity to put this theory to the test came in 2016 November, when ASSASN-16ma—another gamma-ray nova that bore striking similarities to V1324 Sco—was detected. With its early detection, ASSASN-16ma was benefited by a dedicated *Fermi* observational campaign, allowing for gamma-ray observations with a much higher signal-to-noise ratio. This allowed for a much more sensitive gamma-ray light curve than for V1324 Sco—which was only observed during *Fermi's* regularly scheduled all sky monitoring—and we were able to resolve changes in flux on a day-to-day basis.

Li (2017) found that changes in the gamma-ray and optical emission from ASSASN-16ma tracked one another, indicating that both types of emission had the same underlying source—shocks. This discovery is the first confirmation of the model first proposed in Metzger et al. (2015) to explain the optical emission in V1324 Sco.

## 5.3 Future Work on Classical Novae

Future work depends crucially on obtaining data for both gamma-ray detected and non-gamma-ray detected novae, with the aim of finding one or more variables that are present in the former and absent from the latter. This will require a more homogeneous and complete sampling of classical novae and publishing both gamma-ray detections *and* limits on non-detections. A more systematic approach to finding nova is already underway, in the form of the All-Sky Automated Survey for Supernovae (ASAS-SN), which is now patrolling the skies for classical novae (as well as supernovae). This will be complimented in the future by the Large Synoptic Survey Telescope (LSST), which has a snapshot saturation limit that is of the same order as the snapshot limiting magnitude of ASAS-SN. This will allow us to detect classical novae across $\sim 10$ orders of magnitude, with a nearly weekly cadence. We are hopeful that these surveys, along with greater involvement from amateurs and further work on the gamma-ray data will allow us to complete the work on gamma-ray novae started here.

APPENDICES

# Appendix A Model of Radio Emission from Different Density Environments

In this section we go through the derivation of a model for free-free emission coming from one or more shells with an $n \propto r^{-\alpha}$ density profile. We first define and justify the underlying physical assumptions of the model in Section A.1.1; we then define our coordinate system (both in terms of physical distance and a unitless variable that simplifies the problem) in Section A.1.2 and Section A.1.3, respectively; in Section A.1.4 we use this coordinate system to find an expression for the density, and in Section A.1.5 we define an expression for the free-free radio emission; finally, in Section A.1.6, we bring all of these expressions together to derive a time-dependent expression for the flux density. All of this work is done assuming that there is a single density profile for the shell of material.

We also include a example plots in Section A.2 that show how the different variables in our final expression qualitatively affect the evolution of the radio light curve. We also have Section A.3, which explicitly derives the mathematical formulation of the filling factor. In Appendix B, we show how to measure this filling factor using optical spectroscopy.

## A.1 Derivation

### A.1.1 Assumptions

We use a *steady flow model*, which assumes that the velocity of the system has a time-independent structure (Truelove & McKee, 1999). This model implicitly conserves both momentum and energy, assumes that any external pressure (e.g. from sweeping up material) is negligible, and that energy loss from radiation is also negligible.

We will use the same model as Wright & Barlow (1975), Seaquist & Palimaka (1977), and Hjellming et al. (1979); that is, an expanding, isothermal, spherical shell of gas. At radio frequencies, such a shell will be dominated by free-free emission, with the total amount of observed emission being a direct function of the density of the emitting material.

The models presented in the works of Wright & Barlow (1975), Seaquist & Palimaka (1977), and Hjellming et al. (1979) make the same assumptions about the conserved quantities stated above. Hjellming et al. (1979) provides justification for these assumptions, stating that, while it is clear that these assumptions aren't

physically accurate, the models that they generate fit the data well.

We will first define the coordinate system in terms of physical distance; after the system has been adequately setup we will transform to a unitless coordinate system that utilizes the time-independent nature of the velocity structure to simplify the problem greatly.

### A.1.2 Coordinate System

We use a cylindrical coordinate system similar to the one used by Hjellming et al. (1979); the vertical coordinate is given by $a$ and the horizontal coordinate is given by $s$ (see Figure A.1). We choose a cylindrical coordinate system both for historical reasons (it is used in Wright & Barlow (1975) and Hjellming et al. (1979)) and because it allows us define the direction to the observer, while still (partially) using the benefits afforded by the radial symmetry of the problem.

Given our assumption of a homologous flow, the variable of importance is the radial distance. To retrieve this variable, we decompose the horizontal coordinate $s$ (see Figure A.1 for further details), giving

$$\begin{aligned} l &= \left(r^2 - a^2\right)^{1/2} \\ \rightarrow r &= (s^2 + a^2)^{1/2} \end{aligned} \tag{A.1}$$

### A.1.3 Transformation to Unitless Velocity Coordinates

We transform the coordinate system by using the standard definition of a homologous flow,

$$r = vt. \tag{A.2}$$

this allows us to rewrite our values of $r$ to be in terms of velocity.

We take this one step further by introducing the maximum ejecta velocity, $v_{max}$; we use this quantity by enforcing the time-independent nature of the velocity structure. We define the transformed value

$$\tilde{r} = \left(\frac{vt}{v_{max}t}\right) \tag{A.3}$$

Bringing it all together, we see that

$$\begin{aligned} \frac{r}{v_{max}t} &= \tilde{r} \\ \rightarrow r &= \tilde{r}v_{max}t \\ dr &= d\tilde{r}v_{max}t \end{aligned} \tag{A.4}$$

These are the values we will use in all further derivations.

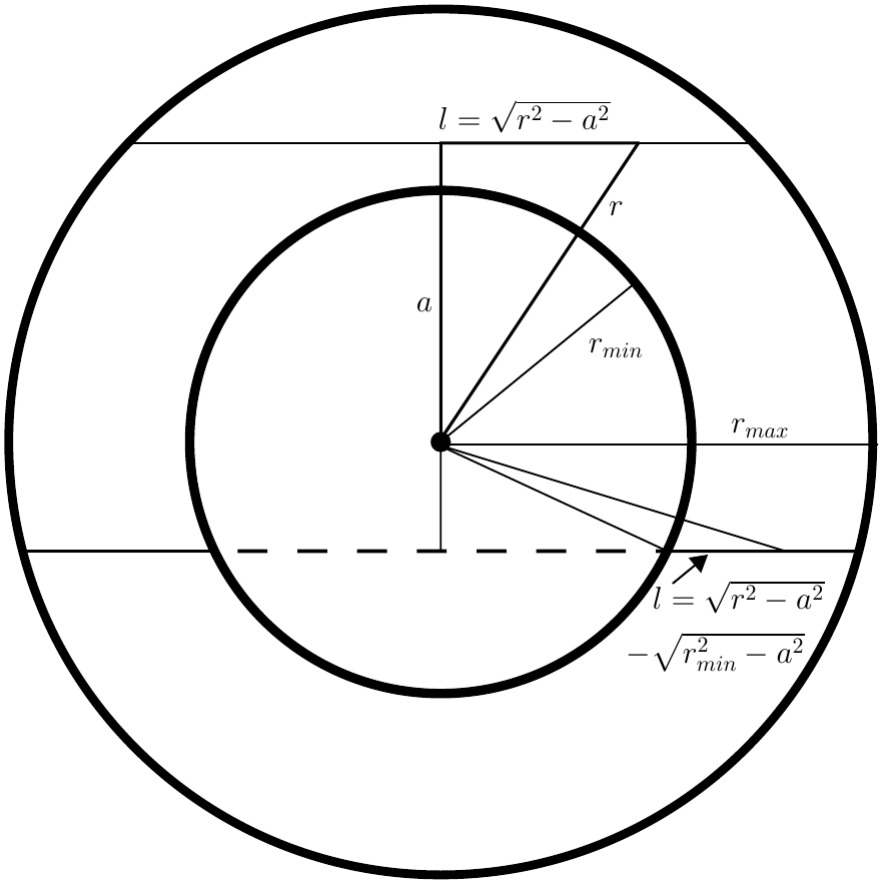


Figure A.1 This is the physical setup we're using for our system. By construction, the ejecta is taken to be a spherical shell with inner radius $r_{min}$ and outer radius $r_{max}$. For the purposes of our analysis (i.e. for the requisite integrals), we will use a cylindrical coordinate system, with height and radius lengths given by the variables $a$ and $s$, respectively.

### A.1.4 Defining Density

The quantities that we are interested in deriving—e.g. $S_\nu$—depend on the density of the ejecta. Therefore, we explicitly write out functions describing the time-evolution of density. We assume that the ejecta density is represented by a spherically symmetric power-law, similar to the models of Seaquist & Palimaka (1977); Hjellming et al. (1979). We define the particle number density as

$$n(r) = \frac{n_0}{r^\alpha}, \tag{A.5}$$

where $n_0$ is some constant that ensures that total particle number stays constant as a function of time. We rewrite this expression in terms of the unitless coordinate system defined in Section A.1.3

$$n(\tilde{r}) = n_0 \tilde{r}^{-\alpha} (v_{max} t)^{-\alpha} \tag{A.6}$$

To fix the constant of integration we enforce the conservation of particle number, which takes the form of

$$\begin{aligned} n &= n_0 r^{-\alpha} \\ \rightarrow \int n dV &= n_0 \int r^{-\alpha} dV \\ \rightarrow n_{tot} &= 4\pi n_0 \int r^{2-\alpha} dr \\ &= \frac{4\pi n_0}{(3-\alpha)} \, r^{3-\alpha} \Big|_{r_{min}}^{r_{max}} . \end{aligned} \tag{A.7}$$

We divide through by $(v_{max}t)^{3-\alpha}$ to transform to the unitless coordinate system, which gives the following

$$\begin{aligned} n_{tot} &= \frac{4\pi n_0}{(3-\alpha)} (v_{max} t)^{3-\alpha} \left(1 - \tilde{r}_{min}^{3-\alpha}\right) \\ \rightarrow n_0 &= \frac{n_{tot}(3-\alpha)}{4\pi (v_{max} t)^{3-\alpha} \left(1 - \tilde{r}_{min}^{3-\alpha}\right)} . \end{aligned} \tag{A.8}$$

We further simplify this by utilizing the fact that $n_{tot}\bar{\mu} = M_{ej}$. Making this substitution, we get

$$n_0 = \frac{M_{ej}(3-\alpha)}{4\pi \bar{\mu} (v_{max} t)^{3-\alpha} \left(1 - \tilde{r}_{min}^{3-\alpha}\right)} . \tag{A.9}$$

This leads to the following final expression for density

$$n(\tilde{r}) = \frac{M_{ej}(3-\alpha)\tilde{r}^{-\alpha}}{4\pi \bar{\mu} (v_{max} t)^{3} \left(1 - \tilde{r}_{min}^{3-\alpha}\right)} , \tag{A.10}$$

where we dropped the $\alpha$ in the exponent of $(v_{max}t)$ by converting $r^{-\alpha}$ to $\tilde{r}^{-\alpha}$.

### A.1.5 Expression for Observed Flux

Our assumption of LTE allows us to write out the following relatively simple expression for the flux density

$$S_\nu = 2\pi B_\nu (1/D)^2 \int a(1 - \exp^{-\tau(a)}) da, \tag{A.11}$$

where $\nu$ is the observed frequency, $B_\nu$ is the Planck function, $D$ is the distance, and $\tau$ is the optical depth (which we will define in the next Section).

We substitute $\tilde{a} = a/(v_{max}t)$ to convert to the unitless coordinate system, which gives

$$S_\nu = 2\pi B_\nu (1/D)^2 (v_{max}t)^2 \int \tilde{a}(1 - \exp^{-\tau(\tilde{a})}) d\tilde{a} \tag{A.12}$$

We further collapse this expression by setting the variables in front of the integral–excluding $t$—equal to a new constant,

$$\Psi = \frac{2\pi B_\nu v_{max}^2}{D^2}. \tag{A.13}$$

Note that $\Psi$ has units of flux (erg s$^{-1}$ cm$^{-2}$ Hz$^{-1}$) divided by time squared (s$^{-2}$), assuming that all inputed values are given in CGS.

This allows us to write Equation A.12 as

$$S_\nu = \Psi\ t^2 \int \tilde{a}(1 - \exp^{-\tau(\tilde{a})}) d\tilde{a} \tag{A.14}$$

#### A.1.5.1 Defining $\tau$

For free-free emission, the optical depth is given by the expression:

$$\tau(a) = \int \alpha(n, \nu, T) ds, \tag{A.15}$$

$$= \int n^2(a) \chi(\nu, T) ds. \tag{A.16}$$

$\chi(\nu)$ is an equation for the opacity of free-free emission, given by (Allen, 1973)

$$\chi(\nu, T) = 3.7 \times 10^8 \mathrm{cm}^5 \left[ T^{-1/2} Z \nu^{-3} \left( 1 - e^{-\frac{h\nu}{kT}} \right) \right]_{\mathrm{CGS}} g_{ff}, \tag{A.17}$$

where $g_{ff}$ is the Gaunt factor, a value of order unity that captures quantum mechanic corrections. Since we are only concerned with the radio regime, we can approximate the Gaunt factor as (Bekefi, 1967)

$$g_{ff}(\nu, T) = \frac{\sqrt{3}}{\pi} \left[ 17.7 + \ln \left( \frac{T^{3/2}}{\nu} \right) \right]. \tag{A.18}$$

Being in the radio wavelength regime also allows us to simplify Equation A.17 by taking the limit as $n\nu \ll kT$, which gives

$$\chi(\nu, T) \approx 0.018 \mathrm{cm}^5 \left[ T^{-3/2} \nu^{-2} \right]_{\mathrm{CGS}} g_{ff}, \tag{A.19}$$

note that we also took $Z = 1$.

### A.1.6 Bringing Density and Flux Together

We substitute the expression for the density (Equation A.10) into A.15 to get

$$\tau(\tilde{a}) = \left[\frac{M_{ej}(3-\alpha)}{4\pi\bar{\mu}(v_{max}t)^3\left(1-\tilde{r}_{min}^{3-\alpha}\right)}\right]^2 (v_{max}t)\chi(\nu,T)\int \tilde{r}^{-2\alpha}d\tilde{s}. \tag{A.20}$$

We picked up another value of $(v_{max}t)$ by converting the differential $ds$ to $d\tilde{s}$. Note that the quantity in front of the integral is independent of the value of $a$. Therefore, we collect all of the constant terms and recast them as a new quantity,

$$\Xi = 0.018 \text{ sec}^5\text{Hz}^2 \left[T_e^{-3/2} v_{max}^{-5}\left(\frac{M_{\rm ej}Z}{\bar{\mu}}\right)^2\right]_{\rm cgs} g_{ff}. \tag{A.21}$$

Substituting $\Xi$ into our equation—as well as substituting Equation A.1—we write $\tau$ as

$$\tau(\tilde{a}) = \Xi\ \nu^{-2}t^{-5}\left[\frac{(3-\alpha)}{\left(1-\tilde{r}_{min}^{3-\alpha}\right)}\right]^2 \int \frac{d\tilde{s}}{(\tilde{a}^2+\tilde{s}^2)^\alpha} \tag{A.22}$$

With this in hand, we must now define the different regions of integration.

#### A.1.6.1 Regions of Integration

Looking at Figure A.1, we can see that there are two regions of integration: $\tilde{a} < \tilde{r}_{min}$ (Region 1), and $\tilde{r}_{min} < \tilde{a} < 1$ (Region 2). The lower bound for Region 1 is $\sqrt{\tilde{r}_{min}^2 - \tilde{a}^2}$, and the lower bound for Region 2 is 0. Using this, we define the following functions

$$\tau_1(\tilde{a}) = \Xi\ \nu^{-2}t^{-5}\left[\frac{(3-\alpha)}{\left(1-\tilde{r}_{min}^{3-\alpha}\right)}\right]^2 \int_{\sqrt{\tilde{r}_{min}^2-\tilde{a}^2}}^{\sqrt{1-\tilde{a}^2}} \frac{d\tilde{s}}{(\tilde{a}^2+\tilde{s}^2)^\alpha} \tag{A.23}$$

$$\tau_2(\tilde{a}) = \Xi\ \nu^{-2}t^{-5}\left[\frac{(3-\alpha)}{\left(1-\tilde{r}_{min}^{3-\alpha}\right)}\right]^2 \int_{0}^{\sqrt{1-\tilde{a}^2}} \frac{d\tilde{s}}{(\tilde{a}^2+\tilde{s}^2)^\alpha}. \tag{A.24}$$

#### A.1.6.2 Final Expression for $S_\nu$

To write our final expression for $S_\nu$ we need to take Equation A.14 and break up the integral into the two different regions defined in the previous section. Doing this, we obtain the following:

$$S_\nu = \Psi\ t^2\left[\int_0^{\tilde{r}_{min}} \tilde{a}(1-\exp^{-\tau_1(\tilde{a})})d\tilde{a}\ + \int_{\tilde{r}_{min}}^1 \tilde{a}(1-\exp^{-\tau_2(\tilde{a})})d\tilde{a}\right]. \tag{A.25}$$

This expression for the free-free emission only has four free variables. Just by inspection, we can determine that the variable $\Psi$ sets the scale for the total amount of flux–i.e. larger $\Psi \rightarrow$ larger $S_\nu$–while the variable $\Xi$ determines how long it will take for the light-curve to turnover–i.e. larger $\Xi \rightarrow$ later turnover. However, it is not immediately clear how $\tilde{r}_{min}$and the power-law index will affect the light-curve evolution.

## A.2 Example Plots

We can gain insight into what effect $\tilde{r}_{min}$and the density power-law index play in shaping the evolution of the radio light curve by testing values and plotting the results. These can be seen in Figures A.2 and A.3, which shows the 4.5 GHz flux as a function of time for a fiducial ejecta model ($v_{max} = 3,000$ km s$^{-1}$, $M_{ej} = 5.0 \times 10^{-5} M_\odot$, $D = 4.5$ kpc). Along with the flux, we also plotted, with the reciprocal Y axis, the best fit spectral index, so that we can monitor its evolution as a function of time.

The primary feature is a limb-darkening effect, wherein the outer parts of the envelope become optically thin sooner than the inner parts. This effect lowers the spectral index–as it is a superposition of the optically thin and optically thick regions–and the total flux is still increasing, albeit more slowly than it was previously. This limb darkening effect occurs for small values of $\tilde{r}_{min}$, as well as large values for the density power-law index.

Coupled to this, we also see that, as the density power-law index increases, so too does the spectral index during the transition phase between optically thin and optically thick. This result was first derived by Wright & Barlow (1975) in their exposition on the radio emission from stellar mass-loss.

## A.3 Filling Factor

The standard model for treating clumping comes from e.g. Abbott et al. (1981), where clumping is treated by assuming that the gas has two components: high-density regions, with $n = n_H$, and low-density regions, with $n = n_L$. We assume that some fraction $f$ of the gas is in the clumps, and that the remainder of the gas (i.e. $1 - f$) is in the low-density region. Further, the ratio of the two densities is given by $x$—that is, $n_L/n_H = x < 1$. We still say that the *total* density is given by $n_{tot} = n_0 r^{-\alpha}$. This allows us to write out the following

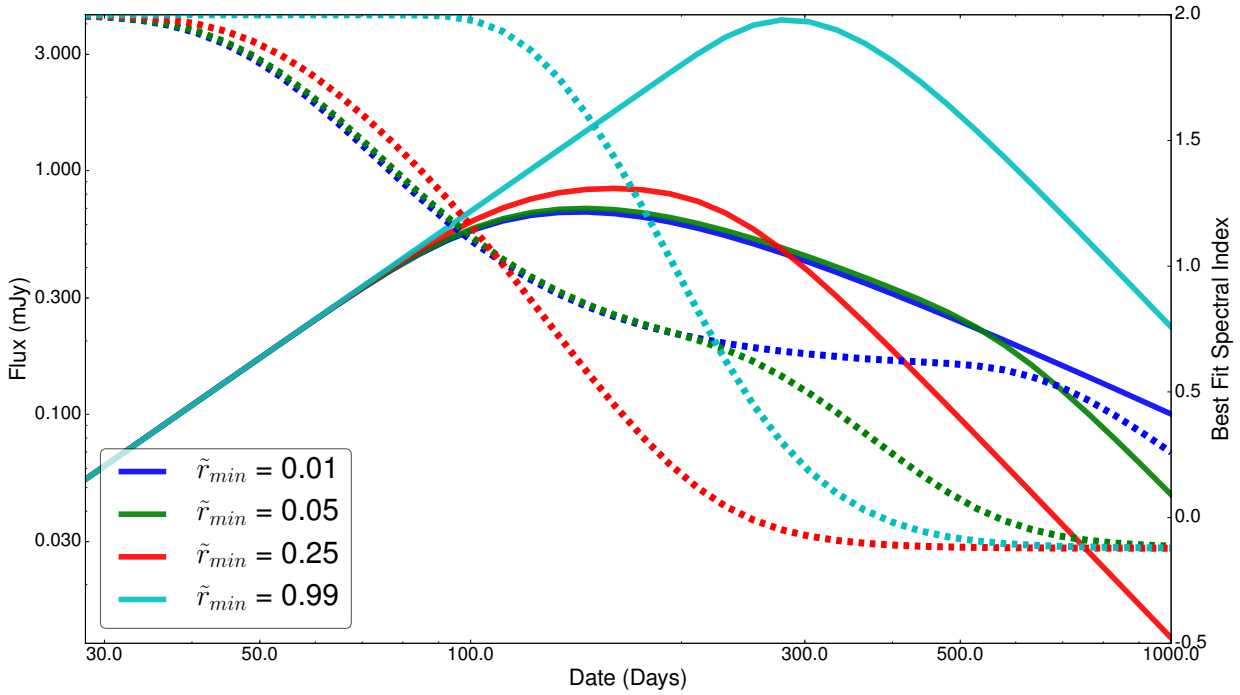


Figure A.2 Plot demonstrating the effect of varying $\tilde{r}_{min}$. The solid lines correspond to the Y axis on the left, and give the 4.5 GHz flux, while the dashed lines correspond to the Y axis on the right and give the best fit spectral index. For smaller values of $\tilde{r}_{min}$ we see effects of limb darkening, where the outer portion of the envelope has become optically thin, while the inner regions remain optically thick. The observed spectral index is a combination of the optically thin and thick regions. We also see that $\tilde{r}_{min}$ determines when the spectrum turns over, with smaller values of $\tilde{r}_{min}$ turning over later.

$$\begin{aligned} n_{tot} &= \frac{n_0}{r^\alpha} \\ &= f n_H + (1-f) n_L \\ &= n_H (f - (1-f)x) \end{aligned} \tag{A.26}$$

Since $n_{tot}$ is still equal to its previous expression, we find that the $n_0$ is also equal to its previous expression (that is, Equation A.9). Plugging this into Equation A.26, we find

$$n_H = \frac{M_{ej}(3-\alpha)\tilde{r}^{-\alpha}}{4\pi\bar{\mu}(\tilde{r})(v_{max}t)^3\left(1-\tilde{r}_{min}^{3-\alpha}\right)\left(f-(1-f)x\right)}, \tag{A.27}$$

Along with rewriting our expression for density, we also need to rewrite the expression for optical depth.

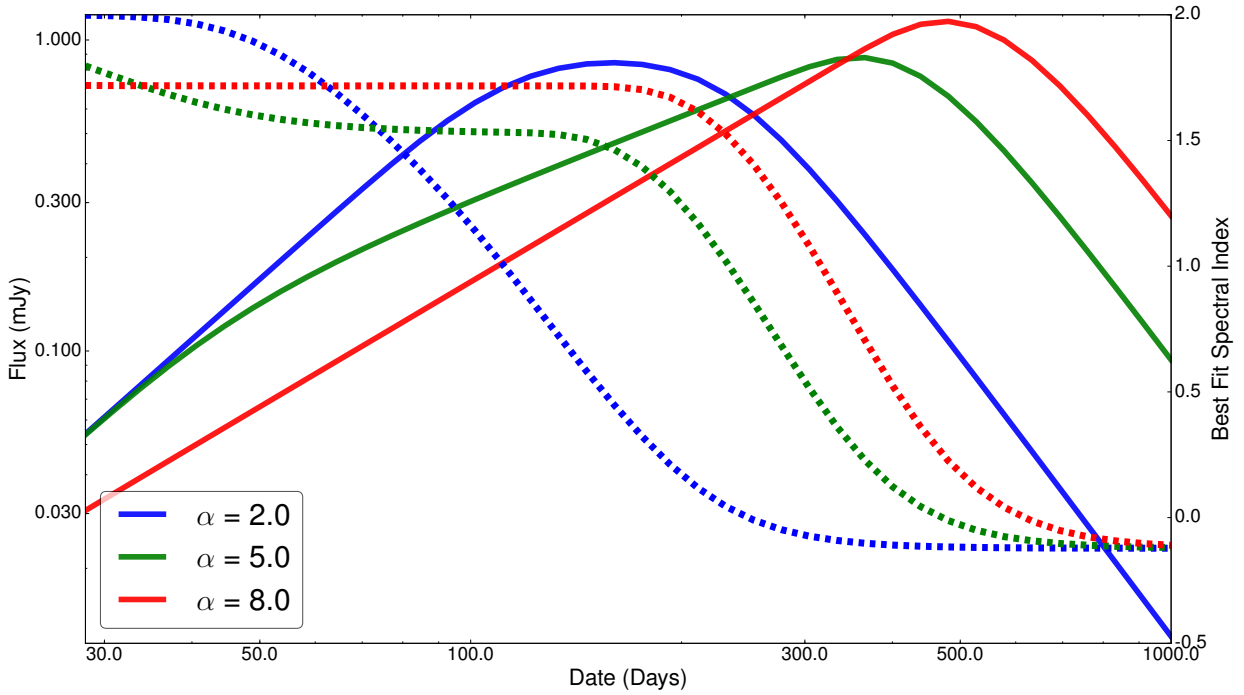


Figure A.3 Sister plot to Figure A.2, this shows the effect of varying the power-law index for the density profile ($\alpha$). A steeper power-law index has an effect similar to a smaller $\tilde{r}_{min}$, in that it turns over at a later time and the spectral index drops below 2.0 earlier. But, unlike a smaller $\tilde{r}_{min}$, a larger power-law index peaks at a larger flux, and also has a larger spectral index in the period between the optically thick and thin phases.

Specifically, this becomes

$$\tau(\tilde{a}) = (v_{max}t)\int (f n_H^2(\tilde{a}) + (1-f)n_L^2(\tilde{a}))\chi(\nu,T)d\tilde{s} \quad (A.28)$$

$$= \chi(\nu,T)(v_{max}t)\int n_H^2(\tilde{a})(f+(1-f)x^2)d\tilde{s} \quad (A.29)$$

Substituting in our new expression for $n_H$, we find

$$\tau(\tilde{a}) = \left[\frac{M_{ej}(3-\alpha)}{4\pi\bar{\mu}(f-(1-f)x)(v_{max}t)^3\left(1-\tilde{r}_{min}^{3-\alpha}\right)}\right]^2 (v_{max}t)\chi(\nu,T)\int \tilde{r}^{-2\alpha}(f+(1-f)x^2)d\tilde{s} \quad (A.30)$$

$$= \Xi t^{-5}\nu^{-2}\left[\frac{(3-\alpha)}{\left(1-\tilde{r}_{min}^{3-\alpha}\right)}\right]^2\left(\frac{f+(1-f)x^2}{(f-(1-f)x)^2}\right)\int \tilde{r}^{-2\alpha}d\tilde{s} \quad (A.31)$$

$$= \Xi t^{-5}\nu^{-2}\left[\frac{(3-\alpha)}{\left(1-\tilde{r}_{min}^{3-\alpha}\right)}\right]^2 \mathscr{F}\int \tilde{r}^{-2\alpha}d\tilde{s} \quad (A.32)$$

This is the same expression we saw without the filling factor, but with the inclusion of a new correction

factor $\mathscr{F}$, which is defined as

$$\mathscr{F} = \left( \frac{f + (1-f)x^2}{(f-(1-f)x)^2} \right) \tag{A.33}$$

This expression is simplified by using the assumptions of Osterbrock (1989), which is to say that *all* of the gas is in clumps and the regions surrounding the clumps are empty. Mathematically, this means that $n_H >> n_L$, so $x \approx 0$. The term $\mathscr{F}$ then simplifies to

$$\mathscr{F} \approx \left( \frac{f}{(f)^2} \right) = f^{-1} \tag{A.34}$$

# Appendix B Deriving the Filling Factor

In this Section we derive a means of determining the filling factor, a correction term for the inhomogeneities (clumpiness) of the ejecta. The following derivation of the filling factor is laid out according the following plan: first we find an analytic expression, in terms of measurables, for the filling factor; then, we detail how we measured the variables, the uncertainty for the variables, and how we incorporated the uncertainty into our final calculation. The method we use is similar to the one used in Ederoclite et al. (2006).

## B.1 Derivation

From Berkhuijsen (1998), the filling factor is given by equation 1a,

$$f_V = \frac{\langle n_e^2 \rangle}{n_e^2}, \tag{B.1}$$

where $\langle n_e^2 \rangle$ is the average of the density squared. This can be rewritten using equation 4 of the same paper,

$$\langle n_e^2 \rangle = \frac{EM}{L}, \tag{B.2}$$

where $EM$ is the emission measure and $L$ is the characteristic length of the emitting material. For our purposes we will assume spherical symmetry of the ejecta and say that the characteristic length is $2v_{max}t$.

We can determine the emission measure from equation 3-36 in Spitzer (1978),

$$\int I_\nu d\nu = h\nu\alpha_{mn} \left(\frac{n_p}{n_e}\right) \times 2.46 \times 10^{17} EM. \tag{B.3}$$

This expression can also be represented as

$$\int I_\nu d\nu = \frac{\int F_\nu d\nu}{\Omega} \approx \frac{F_\nu \Delta\nu}{\Omega} = \frac{F_\lambda \Delta\lambda}{\Omega}, \tag{B.4}$$

where $\Omega$ is the solid angle of the source, which we approximate as $(A/D)^2 = \pi(r/D)^2$. $r$ is the ejecta radius, which is just $v_{max}t$, and $D$ is the distance to the source.

This leads us to the following expression for $EM$

$$EM = \frac{F_\lambda \Delta\lambda}{h\nu_{H\beta}\alpha_{42}(2.46\times10^{17})\Omega} \text{ pc cm}^{-7} \tag{B.5}$$

$$= \frac{F_\lambda \Delta\lambda \pi D^2}{h\nu_{H\beta}\alpha_{42}(2.46\times10^{17})(v_{max}t)^2} \text{ pc cm}^{-7}. \tag{B.6}$$

Using this expression for $EM$, we can rewrite equation B.2 as

$$\langle n_e^2 \rangle = \frac{F_\lambda \Delta\lambda \pi D^2}{2h\nu_{H\beta}\alpha_{42}(2.46\times10^{17})(v_{max}t)^3} \text{ pc cm}^{-7}. \tag{B.7}$$

This expression is in terms of pc cm$^{-7}$, so we must convert it to cm$^{-6}$. To do this, we multiply by $\left(\frac{3.086\times10^{18}\text{ cm}}{1\text{ pc}}\right)$, which gives

$$\langle n_e^2 \rangle = \frac{4\pi^2 F_\lambda \Delta\lambda D^2}{2h\nu_{H\beta}\alpha_{42}(v_{max}t)^3} \text{ cm}^{-6}. \tag{B.8}$$

Finally, we can determine the density by using spectroscopic line ratios. We will use the [O III] line ratio to determine density by using equation 5.4 in Osterbrock (1989)

$$R_{[OIII]} = \frac{j_{\lambda4959} + j_{\lambda5007}}{j_{\lambda4363}} = \frac{7.90\exp(3.29\times10^4/T_e)}{1+4.5\times10^{-4}n_e/T_e^{1/2}}, \tag{B.9}$$

where all quantities are in CGS. This leads to our expression for $n_e$

$$n_e = \frac{T_e^{1/2}}{4.5\times10^{-4}}\left(\frac{7.90\exp(3.29\times10^4/T_e)}{R_{[OIII]}} - 1\right) \text{ cm}^{-3}. \tag{B.10}$$

Squaring the above expression and combining it with equations B.1 and B.8, we can now write out our expression for the filling factor.

$$f_V = \left(\frac{2\pi^2 F_\lambda \Delta\lambda D^2}{h\nu_{H\beta}\alpha_{42}(v_{max}t)^3}\right) \times \left[\frac{T_e^{1/2}}{4.5\times10^{-4}}\left(\frac{7.90\exp(3.29\times10^4/T_e)}{R_{[OIII]}} - 1\right)\right]^{-2}. \tag{B.11}$$

## B.2 Measured Values and Uncertainty

The unknown values that we need to solve equation B.11 are electron temperature ($T_e$), distance ($D$), ejecta velocity ($v_{max}$), the oxygen line ratio ($R_{[OIII]}$), and the H$_\beta$ flux ($F_\lambda\Delta\lambda$). We use the LBT spectrum taken on day +353, as it is taken well into the nebular phase and has better spectral response calibration than the SOAR spectrum. Note that the MODS1 instrument was not designed to be a spectrophotometer, and the seeing was twice the width of the slit, so that $\sim 50\%$ of the flux fell outside of the slit. This issue is negated

for line ratios (discussed below), but it does affect absolute line fluxes. Therefore, we will use a fiducial value of 10% for the uncertainty of the line ratios—to account for general calibration uncertainties—and 50% uncertainty for the absolute line fluxes.

With this value for the uncertainty, we use the IRAF tool *splot* to measure an $H_\beta$ flux—corrected for the throughput issue mentioned above—of $8.38 \pm 4.19 \times 10^{-15}$ ergs cm$^{-2}$ s$^{-1}$. The line ratio $R_{[OIII]}$ is determined by $j_{\lambda 4959}$, $j_{\lambda 5007}$, and $j_{\lambda 4363}$. We find for these quantities

- $j_{\lambda 4959} = 66.2 \pm 6.6 \times 10^{-15}$ ergs cm$^{-2}$ s$^{-1}$;
- $j_{\lambda 5007} = 218.0 \pm 21.8 \times 10^{-15}$ ergs cm$^{-2}$ s$^{-1}$;
- $j_{\lambda 4363} = 4.8 \pm 0.5 \times 10^{-15}$ ergs cm$^{-2}$ s$^{-1}$.

As these lines are meant to be a measure of the flux emitted from the source—not the flux measured—we need to make further corrections for interstellar reddening. From Finzell et al. (2015) we know that the reddening is $E(B-V) = 1.16 \pm 0.12$ for V1324 Sco. We use the wavelength specific reddening extinction law of Cardelli et al. (1989) (equations 1 and 3), with an $R_V = 3.1$, to determine the level of extinction. Doing this, we find reddening corrected fluxes of:

- $j_{\lambda 4959} = 30.5 \pm 12.4 \times 10^{-13}$ ergs cm$^{-2}$ s$^{-1}$;
- $j_{\lambda 5007} = 95.9 \pm 38.2 \times 10^{-13}$ ergs cm$^{-2}$ s$^{-1}$;
- $j_{\lambda 4363} = 4.5 \pm 2.2 \times 10^{-13}$ ergs cm$^{-2}$ s$^{-1}$,

and the reddening corrected H$\beta$ line flux is $4.35 \pm 2.84 \times 10^{-13}$ ergs cm$^{-2}$ s$^{-1}$. Note that the uncertainty on the flux values has increased due to the inclusion of the reddening uncertainty. Using these reddening corrected flux values, we find an $R_{[OIII]}$ value of $29.3 \pm 4.4$.

For two of the remaining unknown values—$T_e$ and $D$—we use the same values as section 3.4 ($T_e = 10^4$ K, $D = 6.5$ kpc). The remaining value, $v_{max}$, is derived using the best fit values to the radio data.

## B.3 Final Value

To determine the final value for $f_v$ we generate distributions of the input variables and plug them into B.11, which gives us a distribution of values for $f_v$. The final value that we quote for $f_v$ is the average of this distribution, and the uncertainty in $f_v$ is the standard deviation of $f_v$.

We can utilize our distribution of velocities derived in section 3.4 to help alleviate some of the uncertainty associated with our measured quantities. From this, and using our canonical nova temperature of $10^4$ K and

distance of 6.5 kpc, we get a filling factor of

$$f_V = 5.2 \pm 2.2 \times 10^{-2} \ . \tag{B.12}$$

The uncertainty is dominated by both the reddening value uncertainty and the fiducial flux calibration uncertainty.

# BIBLIOGRAPHY

# BIBLIOGRAPHY


Abbott, D. C., Bieging, J. H., & Churchwell, E. 1981, ApJ, 250, 645

Abdo, A. A., Ackermann, M., Ajello, M., et al. 2010, Science, 329, 817

Ackermann, M., Ajello, M., Albert, A., et al. 2014, Science, 345, 554

Allen, C. W. 1973, Astrophysical quantities (Springer)

Bath, G. T. 1978, MNRAS, 182, 35

Bath, G. T., & Shaviv, G. 1976, MNRAS, 175, 305

Bekefi, G. 1967, ZAp, 67, 315

Berkhuijsen, E. M. 1998, in Lecture Notes in Physics, Berlin Springer Verlag, Vol. 506, IAU Colloq. 166: The Local Bubble and Beyond, ed. D. Breitschwerdt, M. J. Freyberg, & J. Truemper, 301–304

Bernstein, R., Shectman, S. A., Gunnels, S. M., Mochnacki, S., & Athey, A. E. 2003, in Proc. SPIE, Vol. 4841, Instrument Design and Performance for Optical/Infrared Ground-based Telescopes, ed. M. Iye & A. F. M. Moorwood, 1694–1704

Bhatia, A. K., & Kastner, S. O. 1995, ApJS, 96, 325

Blandford, R. D., & Ostriker, J. P. 1978, ApJ, 221, L29

Blumenthal, G. R., & Gould, R. J. 1970, Reviews of Modern Physics, 42, 237

Bode, M. F., & Evans, A. 2008, Classical Novae (Cambridge University Press)

Bode, M. F., & Kahn, F. D. 1985, MNRAS, 217, 205

Bode, M. F., O'Brien, T. J., Osborne, J. P., et al. 2006, ApJ, 652, 629

Bond, I. A., Abe, F., Dodd, R. J., et al. 2001, MNRAS, 327, 868

Cardelli, J. A., Clayton, G. C., & Mathis, J. S. 1989, ApJ, 345, 245

Cheung, C. C., Donato, D., Wallace, E., et al. 2010, The Astronomer's Telegram, 2487

Cheung, C. C., Glanzman, T., & Hill, A. B. 2012a, The Astronomer's Telegram, 4284

Cheung, C. C., Hays, E., Venters, T., Donato, D., & Corbet, R. H. D. 2012b, The Astronomer's Telegram, 4224

Cheung, C. C., Jean, P., & Shore, S. N. 2015, The Astronomer's Telegram, 7315

Cheung, C. C., Jean, P., Shore, S. N., et al. 2016, ApJ, 826, 142

Chevalier, R. A. 1982, ApJ, 259, 302

—. 1998, ApJ, 499, 810

Chomiuk, L., Krauss, M. I., Rupen, M. P., et al. 2012, ApJ, 761, 173

Chomiuk, L., Linford, J. D., Yang, J., et al. 2014, Nature, 514, 339

Covey, K. R., Ivezić, Ž., Schlegel, D., et al. 2007, AJ, 134, 2398

Cunningham, T., Wolf, W. M., & Bildsten, L. 2015, ApJ, 803, 76

Darnley, M. J., Ribeiro, V. A. R. M., Bode, M. F., Hounsell, R. A., & Williams, R. P. 2012, ApJ, 746, 61

Dekker, H., D'Odorico, S., Kaufer, A., Delabre, B., & Kotzlowski, H. 2000, in Proc. SPIE, Vol. 4008, Optical and IR Telescope Instrumentation and Detectors, ed. M. Iye & A. F. Moorwood, 534–545

Derdzinski, A. M., Metzger, B. D., & Lazzati, D. 2016, ArXiv e-prints, arXiv:1610.02401

Drake, J. J., Delgado, L., Laming, J. M., et al. 2016, ApJ, 825, 95

Drury, L. O., Aharonian, F. A., & Voelk, H. J. 1994, A&A, 287, 959

Duerbeck, H. W. 2008, CAMBRIDGE ASTROPHYSICS SERIES, 43, 1

Ederoclite, A., Mason, E., Della Valle, M., et al. 2006, A&A, 459, 875

Ferland, G. J., Korista, K. T., Verner, D. A., et al. 1998, PASP, 110, 761

Finzell, T., Chomiuk, L., Munari, U., & Walter, F. M. 2015, ApJ, 809, 160

Finzell, T., Chomiuk, L., Metzger, B. D., et al. 2017, ArXiv e-prints, arXiv:1701.03094

Friedman, S. D., York, D. G., McCall, B. J., et al. 2011, ApJ, 727, 33

Gallagher, J. S. 1977, AJ, 82, 209

Gallagher, J. S., & Starrfield, S. 1978, ARA&A, 16, 171

Gallagher, III, J. S., & Code, A. D. 1974, ApJ, 189, 303

Gehrz, R. D. 1988, ARA&A, 26, 377

Gehrz, R. D., Grasdalen, G. L., Hackwell, J. A., & Ney, E. P. 1980, ApJ, 237, 855

Gehrz, R. D., Jones, T. J., Woodward, C. E., et al. 1992, ApJ, 400, 671

Gill, C. D., & O'Brien, T. J. 1998, MNRAS, 300, 221

—. 1999, MNRAS, 307, 677

Güver, T., & Özel, F. 2009, MNRAS, 400, 2050

Hays, E., Cheung, T., & Ciprini, S. 2013, The Astronomer's Telegram, 5302

Hillman, Y., Prialnik, D., Kovetz, A., Shara, M. M., & Neill, J. D. 2014, MNRAS, 437, 1962

Hjellming, R. M., van Gorkom, J. H., Taylor, A. R., et al. 1986, ApJ, 305, L71

Hjellming, R. M., & Wade, C. M. 1970, ApJ, 162, L1

Hjellming, R. M., Wade, C. M., Vandenberg, N. R., & Newell, R. T. 1979, AJ, 84, 1619

Hornoch, K. 2013, The Astronomer's Telegram, 5621

Hounsell, R., Bode, M. F., Hick, P. P., et al. 2010, ApJ, 724, 480

Hutchings, J. B. 1972, MNRAS, 158, 177

Irwin, M. J., Lewis, J., Hodgkin, S., et al. 2004, in SPIE Astronomical Telescopes+ Instrumentation, International Society for Optics and Photonics, 411–422

Ivanova, N., Justham, S., Avendano Nandez, J. L., & Lombardi, J. C. 2013, Science, 339, 433

José, J., & Hernanz, M. 1998, ApJ, 494, 680

Kantharia, N. G., Dutta, P., Roy, N., et al. 2016, MNRAS, 456, L49

Kastner, S. O., & Bhatia, A. K. 1995, ApJ, 439, 346

Knigge, C. 2011, in Astronomical Society of the Pacific Conference Series, Vol. 447, Evolution of Compact Binaries, ed. L. Schmidtobreick, M. R. Schreiber, & C. Tappert, 3

Kovetz, A. 1998, ApJ, 495, 401

Kovetz, A., & Prialnik, D. 1985, ApJ, 291, 812

Kraft, R. P. 1964, ApJ, 139, 457

Kraft, R. P., Burrows, D. N., & Nousek, J. A. 1991, ApJ, 374, 344

Li, K.-L. 2017, Nature, Submitted, 1

Linford, J. D., Chomiuk, L., Nelson, T., et al. 2017, ArXiv e-prints, arXiv:1703.03333

Livio, M., Shankar, A., Burkert, A., & Truran, J. W. 1990, ApJ, 356, 250

Lloyd, H. M., O'Brien, T. J., & Bode, M. F. 1997, MNRAS, 284, 137

LSST Science Collaboration, Abell, P. A., Allison, J., et al. 2009, ArXiv e-prints, arXiv:0912.0201

McLaughlin, D. B. 1936, in Publications of the American Astronomical Society, Vol. 8, Publications of the American Astronomical Society, 145

McLaughlin, D. B. 1956, Vistas in astronomy, 2, 1477

Metzger, B. D., Caprioli, D., Vurm, I., et al. 2016, MNRAS, 457, 1786

Metzger, B. D., Finzell, T., Vurm, I., et al. 2015, MNRAS, 450, 2739

Metzger, B. D., Hascoët, R., Vurm, I., et al. 2014, MNRAS, 442, 713

Minniti, D., Lucas, P. W., Emerson, J. P., et al. 2010, New A, 15, 433

Mukai, K., & Ishida, M. 2001, ApJ, 551, 1024

Munari, U., Dallaporta, S., Castellani, F., et al. 2013, MNRAS, 435, 771

Munari, U., Dallaporta, S., & Valisa, P. 2012, The Astronomer's Telegram, 4320

Munari, U., & Henden, A. 2013, Information Bulletin on Variable Stars, 6087, arXiv:1312.5890

Munari, U., & Zwitter, T. 1997, A&A, 318, 269

Nelson, T., Donato, D., Mukai, K., Sokoloski, J., & Chomiuk, L. 2012, ApJ, 748, 43

Nelson, T., Chomiuk, L., Roy, N., et al. 2014, ApJ, 785, 78

O'Brien, T. J., Lloyd, H. M., & Bode, M. F. 1994, MNRAS, 271, 155

Osterbrock, D. E. 1989, Astrophysics of gaseous nebulae and active galactic nuclei (University science books)

Paczyński, B. 1965, Acta Astron., 15, 197

Page, K. L., Osborne, J. P., Wagner, R. M., et al. 2013, ApJ, 768, L26

Pagnotta, A., & Schaefer, B. E. 2014, ApJ, 788, 164

Patil, A., Huard, D., & Fonnesbeck, C. J. 2010, Journal of statistical software, 35, 1

Patterson, J. 1984, ApJS, 54, 443

Payne-Gaposchkin, C. 1964, The galactic novae (New York: Dover Publication, 1964)

Pejcha, O., Antognini, J. M., Shappee, B. J., & Thompson, T. A. 2013, MNRAS, 435, 943

Pejcha, O., Metzger, B. D., & Tomida, K. 2016, MNRAS, 461, 2527

Poole, T. S., Breeveld, A. A., Page, M. J., et al. 2008, MNRAS, 383, 627

Prialnik, D. 1986, ApJ, 310, 222

Prialnik, D., & Kovetz, A. 1995, ApJ, 445, 789

Rappaport, S., Verbunt, F., & Joss, P. C. 1983, ApJ, 275, 713

Ribeiro, V. A. R. M., Darnley, M. J., Bode, M. F., et al. 2011, MNRAS, 412, 1701

Ribeiro, V. A. R. M., Munari, U., & Valisa, P. 2013, ApJ, 768, 49

Ribeiro, V. A. R. M., Bode, M. F., Darnley, M. J., et al. 2009, ApJ, 703, 1955

Robinson, E. L. 1975, AJ, 80, 515

Roming, P. W. A., Kennedy, T. E., Mason, K. O., et al. 2005, Space Sci. Rev., 120, 95

Sacco, G. G., Morbidelli, L., Franciosini, E., et al. 2014, A&A, 565, A113

Saito, R. K., Hempel, M., Minniti, D., et al. 2012, A&A, 537, A107

Sakon, I., Sako, S., Onaka, T., et al. 2016, ApJ, 817, 145

Schaefer, B. E. 2010, ApJS, 187, 275

Schultheis, M., Chen, B. Q., Jiang, B. W., et al. 2014, A&A, 566, A120

Schwarz, G. J., Hauschildt, P. H., Starrfield, S., et al. 1997, MNRAS, 284, 669

Schwarz, G. J., Shore, S. N., Starrfield, S., et al. 2001, MNRAS, 320, 103

Schwarz, G. J., Shore, S. N., Starrfield, S., & Vanlandingham, K. M. 2007, ApJ, 657, 453

Schwarz, G. J., Ness, J.-U., Osborne, J. P., et al. 2011, ApJS, 197, 31

Seaquist, E. 1989, in Classical Novae, Vol. 1, 143–161

Seaquist, E. R., & Palimaka, J. 1977, ApJ, 217, 781

Shen, K. J., & Bildsten, L. 2007, ApJ, 660, 1444

Shore, S. N. 2008, CAMBRIDGE ASTROPHYSICS SERIES, 43, 194

Shore, S. N. 2012, Bulletin of the Astronomical Society of India, 40, 185

Shore, S. N., Augusteijn, T., Ederoclite, A., & Uthas, H. 2011, A&A, 533, L8

Skopal, A., Drechsel, H., Tarasova, T., et al. 2014, A&A, 569, A112

Slavin, A. J., O'Brien, T. J., & Dunlop, J. S. 1995, MNRAS, 276, 353

Sokoloski, J. L., Luna, G. J. M., Mukai, K., & Kenyon, S. J. 2006, Nature, 442, 276

Solf, J. 1983, ApJ, 273, 647

Spitzer, L. 1978, Physical processes in the interstellar medium (John Wiley & Sons), doi:10.1002/9783527617722

Starrfield, S., Iliadis, C., & Hix, W. R. 2016, PASP, 128, 051001

Starrfield, S., Sparks, W. M., & Truran, J. W. 1974, ApJS, 28, 247

Starrfield, S., Truran, J. W., Sparks, W. M., & Kutter, G. S. 1972, ApJ, 176, 169

Strope, R. J., Schaefer, B. E., & Henden, A. A. 2010, AJ, 140, 34

Sumi, T., Udalski, A., Bennett, D. P., et al. 2016, ApJ, 825, 112

Surina, F., Hounsell, R. A., Bode, M. F., et al. 2014, AJ, 147, 107

Taylor, A. R., Hjellming, R. M., Seaquist, E. R., & Gehrz, R. D. 1988, Nature, 335, 235

Taylor, A. R., Pottasch, S. R., Seaquist, E. R., & Hollis, J. M. 1987, A&A, 183, 38

Townsley, D. M., & Bildsten, L. 2004, ApJ, 600, 390

Truelove, J. K., & McKee, C. F. 1999, ApJS, 120, 299

Tylenda, R., Hajduk, M., Kamiński, T., et al. 2011, A&A, 528, A114

Udalski, A. 2003, Acta Astron., 53, 291

Uthas, H., Knigge, C., & Steeghs, D. 2010, MNRAS, 409, 237

Vlasov, A., Vurm, I., & Metzger, B. D. 2016, MNRAS, 463, 394

Vurm, I., & Metzger, B. D. 2016, ArXiv e-prints, arXiv:1611.04532

Wagner, R. M., Dong, S., Bensby, T., et al. 2012, The Astronomer's Telegram, 4157

Walter, F. M., Battisti, A., Towers, S. E., Bond, H. E., & Stringfellow, G. S. 2012, PASP, 124, 1057

Warner, B. 1989, in Classical Novae, ed. M. F. Bode & A. Evans, 1–16

Weston, J. H. S., Sokoloski, J. L., Metzger, B. D., et al. 2016a, MNRAS, 457, 887

Weston, J. H. S., Sokoloski, J. L., Chomiuk, L., et al. 2016b, MNRAS, 460, 2687

Wiescher, M., Görres, J., Uberseder, E., Imbriani, G., & Pignatari, M. 2010, Annual Review of Nuclear and Particle Science, 60, 381

Williams, R. 2012, AJ, 144, 98

Williams, R. E. 1992, AJ, 104, 725

Williams, R. E., Hamuy, M., Phillips, M. M., et al. 1991, ApJ, 376, 721

Williams, R. E., Phillips, M. M., & Hamuy, M. 1994, ApJS, 90, 297

Wright, A. E., & Barlow, M. J. 1975, MNRAS, 170, 41

Yaron, O., Prialnik, D., Shara, M. M., & Kovetz, A. 2005, ApJ, 623, 398